TESE DE DOUTORAMENTO

Novos sistemas electrónicos de comparación de frecuencias mediante interferómetro Michelson para a estabilización de díodos láser

Javier Diz Bugarín

2022

Universidade Vigo

EIDO
Escola Internacional
de Doutoramento

Universidade Vigo
Escola Internacional de Doutoramento

TESE DE DOUTORAMENTO

Novos sistemas electrónicos de comparación de frecuencias mediante interferómetro Michelson para a estabilización de díodos láser

Autor:
Javier Diz Bugarín

Director/Titor:
Prof. Dr. José Benito Vázquez Dorrío

Director:
Prof. Dr. Jesús Blanco García

2022

Universidade Vigo

Escola Internacional de Doutoramento

José Benito Vázquez Dorrío e Jesús Blanco García

FAN CONSTAR que o presente traballo, titulado "Novos sistemas electrónicos de comparación de frecuencias mediante interferómetro Michelson para a estabilización de díodos láser", que presenta Javier Diz Bugarín para a obtención do título de Doutor, foi elaborado baixo a súa dirección no programa de doutoramento "Láser, Fotónica e Visión" interuniversitario das Universidades de A Coruña, Santiago de Compostela e Vigo, e autorizan a súa presentación e defensa pola modalidade de compendio de artigos de investigación.

Vigo, 24 de outubro de 2022.

Os directores da tese de doutoramento

Dr. José Benito Vázquez Dorrío Dr. Jesús Blanco García

AGRADECIMIENTOS

La historia de esta tesis viene ya del pasado siglo, con otro título y otros protagonistas. Luego llegó una pausa que pudo ser definitiva.

Mucho tiempo después Benito y Suso, directores de esta tesis y amigos, se empeñaron en recuperarme para la investigación, contra el viento y marea de la crisis económica que se llevó por delante proyectos e ilusiones. Pero aquí seguimos, y esta tesis es la mejor prueba de ello. Gracias en primer lugar a ellos por ofrecerme esta oportunidad y por estar ahí todos estos años.

A Ismael Outumuro y José Luís Valencia del LOMG, sin cuya colaboración (y de todo el Laboratorio) esta tesis no habría sido posible. Espero que de todo este trabajo salga alguna más y que vengan nuevos proyectos.

A los compañeros de la Universidad y el Departamento de Física, tanto los que están como los que ya no, de todos estos años desde que empezamos a conocernos allá por 1986. En especial a Marta Miranda y Fernando Ribas, coautores de trabajos incluidos en esta tesis.

A mi familia, especialmente a Montse, Natalia y Lorena (por orden decreciente de edad, para que nadie se enfade) que igual se encuentran un interferómetro en la cocina que se ponen a buscar una rana en Salamanca en medio de un congreso. Como ya suponéis ésto no se acaba aquí.

Y por último y para no dejar a nadie atrás, gracias a todos los que de un modo u otro se han cruzado en el camino y a los que se han atrevido a abrir estas páginas. La fortuna favorece a los audaces!

ÍNDICE

RESUMEN

Esta Tesis Doctoral forma parte de una línea de investigación del Departamento de Física Aplicada de la Universidad de Vigo en colaboración con el Laboratorio Oficial de Metrología de Galicia (LOMG) cuyo objetivo último es la estabilización electrónica de diodos láser para aplicaciones interferométricas, entre las que se puede citar el desarrollo de un sistema de calibración de Bloques Patrón Longitudinales (BPL).

La calibración de BPLs se realiza típicamente aplicando el método de excedentes fraccionarios a una serie de patrones de franjas proporcionados por un sistema interferométrico en el que se emplean por lo menos dos fuentes láser de gas tipo He-Ne ultraestabilizadas en longitud de onda. El proceso precisa de un módulo interferométrico encapsulado con control ambiental fino, un sistema electrónico de control para el posicionado de los BPLs y la modulación de fase óptica, un sistema de adquisición y procesamiento de imagen encargado de obtener la fase óptica mediante la combinación apropiada de uno o más patrones de franjas. El proceso de decodificación que proporciona la fase óptica emplea habitualmente Algoritmos de Desplazamiento de Fase (ADFs) combinados con un proceso adicional de reconstrucción de fase ("unwrapping") que proporcione la fase real teniendo en cuenta el orden de las franjas del patrón interferométrico a partir de los valores principales de fase. Durante el proceso, la temperatura, la presión atmosférica y la humedad relativa deben estar monitorizadas para obtener la variación del índice de refracción del aire.

Los equipos comerciales existentes son sistemas cerrados de precio muy elevado y normalmente se sitúan en los laboratorios nacionales de referencia. Uno de los elementos que más los encarece son las fuentes láser ultraestabilizadas de He-Ne, con un ancho de banda inferior a 1 MHz que permite calibrar BPL menores de 100 mm con incertidumbres menores de 50 nm. El uso de de diodos láser ultraestabilizados permite reducir el coste de forma notable con una estabilidad en longitud de onda similar. La estabilización en la longitud de onda de los diodos se consigue actuando sobre la corriente de alimentación y la temperatura, y la ultraestabilización mediante técnicas de anclaje en frecuencia con una celda de gas y un actuador piezoeléctrico. Con este procedimiento, el ancho de banda de los diodos láser se puede reducir a menos de 1 MHz (igual que con los láseres de gas) utilizando la electrónica de control necesaria y con precios mucho más económicos. Una vez conseguida la estabilización de los diodos láser es importante conocer con exactitud la longitud de onda resultante, para lo que se necesita un láser de referencia calibrado y un sistema electrónico de comparación de ambos láseres.

Esta Tesis Doctoral se centra fundamentalmente en los elementos electrónicos necesarios para la medida de la longitud de onda de diodos láser mediante un sistema con interferómetro Michelson de brazo móvil. Se ha desarrollado un nuevo prototipo basado en el método Vernier, mejorando y actualizando desarrollos anteriores. También se ha desarrollado una nueva técnica de medida que hemos denominado "cuenta de multicoeficientes con restos fraccionarios" ("*multicoefficient fractional counting*") que combina y mejora métodos anteriores utilizando marcas de tiempo, multicoincidencias y promediado de múltiples medidas, junto con el uso de restos fraccionarios de las franjas de interferencia para mejorar la precisión.

También se ha contemplado la función final del sistema, abordando tareas relacionadas con el sistema electrónico de control de generación y adquisición de patrones de franjas y su posterior procesado mediante algoritmos diferenciales de desplazamiento de fase ADDFs, así como el proceso de reconstrucción de fase o unwrapping.

CAPÍTULO 1. INTRODUCCIÓN

1.1. CONTEXTO

El conjunto de trabajos de investigación que han dado lugar a esta tesis doctoral están orientados al desarrollo de las herramientas ópticas, electrónicas e informáticas necesarias para la calibración interferométrica de Bloques Patrón Longitudinales (BPL). Estos elementos [1,2], también denominados patrones de cantos o calas, son paralelepípedos de acero, cerámica o tungsteno que se suministran normalmente en conjuntos con un rango de longitudes estándar y son imprescindibles en numerosas aplicaciones industriales ya que proporcionan una referencia de la unidad de longitud o sus submúltiplos, a partir de la longitud de onda del patrón primario o de otras fuentes luminosas secundarias. Los BPL pueden emplearse, según sus cualidades, para la calibración de instrumentos de metrología, la medición de piezas por comparación o la fabricación de piezas en talleres mecánicos. Una importante característica de estos elementos es que pueden apilarse para generar múltiplos de su longitud básica, mediante un procedimiento especial de deslizamiento (*wringing*). La fabricación de los BPL requiere elevada precisión e incertidumbres mínimas, ya que sus caras deben ser perfectamente planas y paralelas, lo que supone un reto continuo para la Metrología Dimensional [3], por ejemplo para BPL cortos (<100 mm) la norma UNE-EN ISO 3650:2000 [4] requiere medidas de tolerancias de 50 nm, lo que implica incertidumbres menores de 20 nm.

El procedimiento de calibración de BPL requiere un entorno controlado en temperatura, ya que los valores estándar se refieren a una temperatura de 20ºC de acuerdo con la norma. La calibración interferométrica es el método más utilizado para la certificación de la longitud nominal del BPL, siendo necesario el empleo de varias fuentes de luz láser ultraestabilizadas combinadas con el método de los excedentes fraccionarios [5,6]. La configuración interferométrica tradicional emplea dos o más fuentes láser de gas estabilizadas en longitud de onda de 10^{-8} nm [7-10] y requiere del encapsulado del módulo interferométrico con, por lo menos, control de temperatura, humedad relativa y presión atmosférica (valores típicos de incertidumbres son 0.01 ºC en temperatura, 1% en humedad relativa y 0.1 mbar en presión). Este control permite calcular el índice de refracción del medio empleando la ecuación de Edlén [11,12] o Ciddor [13] para corregir las longitudes de onda en el proceso de medida.

Las conocidas ventajas de los Algoritmos de Desplazamiento de Fase (ADF) [14,15] para la decodificación de los patrones interferenciales los hacen candidatos idóneos para facilitar una mejora significativa de las prestaciones del proceso junto con una mayor automatización del mismo, lo que redunda en una mejora de la repetibilidad y reproducibilidad del protocolo metrológico. Sin embargo la selección del ADF puede cambiar la incertidumbre expandida de la medida a un valor que depende de la longitud nominal del BPL (por ejemplo con diferencias de un 2.4% para un BPL de 100 mm o de un 15.5% para un BPL de 1 mm dependiendo del ADF utilizado [16]) y es por ello que el diseño y elección del ADF a utilizar es un factor importante a tener en cuenta si se pretende minimizar este parámetro estadístico en este tipo de aplicación.

Así mismo los modernos sistemas de evaluación de la fase óptica interferométrica hacen uso de sistemas de adquisición de imagen y modulación piezoeléctrica que convierten la medida longitudinal de BPL en un proceso semiautomático, controlado por computador, más exacto, menos intrusivo, más rápido y más fácil de usar. Para ambas estrategias existe en la literatura información periódicamente actualizada sobre el diseño eficiente de nuevos algoritmos y sus sensibilidades a las posibles fuentes de error relacionadas con su utilización [17-22]. En la medida de BPLs se hace necesario un proceso adicional de reconstrucción de fase con posibles problemas de frontera que

proporcione la fase real teniendo en cuenta el orden de las franjas del patrón interferométrico a partir de los valores principales de fase [23], un proceso de optimización discreta muy delicado que no ha sido completamente resuelto para todas las posibles situaciones que se pueden presentar [24-26].

Los sistemas comerciales que emplean láseres He-Ne ultraestabilizados son muy costosos y no permiten la introducción de modificaciones o nuevos sistemas de procesado por parte del usuario final. Muchos centros nacionales de referencia como el Centro Español de Metrología (CEM) poseen alguno de estos sistemas comerciales mientras que otros han desarrollado sus propios sistemas interferométricos homologados.

Actualmente es posible utilizar diodos láser ultraestabilizados como alternativa a los láseres de gas He-Ne. Los diodos se montan en configuración de cavidad externa o ECDL. La estabilización se consigue mediante el ajuste preciso de la corriente de alimentación y la temperatura, ésta última mediante una celda Peltier con control PID [27-31]. La ultraestabilización se consigue mediante técnicas de anclaje en frecuencia utilizando una celda de gas de Yodo o Rubidio como referencia dependiendo de la longitud de onda del diodo. La salida del láser se divide en un haz de trabajo y otro de control, circulando éste último a través de la celda de gas. Un fotodetector recoge las variaciones de amplitud del haz de control, que dependen de la diferencia entre la frecuencia de absorción y la del láser. Esta señal de error controla un actuador piezoeléctrico que modifica el ángulo de una red de difracción (*grating*) situada en la cavidad externa (configuración Littrow), lo que permite anclar la frecuencia de trabajo. Este procedimiento de ultraestabilización permite reducir el ancho de banda de los diodos a menos de 1MHz [32].

Así pues, un sistema completo de calibración de BPL con diodo láser estaría formado por tres módulos (Fig. 1): a) un sistema de estabilización del diodo láser, b) sistema interferométrico de medida de la longitud de onda resultante, y c) sistema de medida de longitud con posicionador piezoeléctrico, cámara para la captación de imágenes de fase y un programa de procesamiento de imágenes que implementa los algoritmos de cálculo para la obtención de la magnitud de interés. En esta tesis se realiza la descripción detallada de un sistema de este tipo, abordada en un capítulo posterior. Este tipo de sistema se ha planteado en el marco de proyectos de investigación realizados en colaboración entre el Departamento de Física Aplicada de la Universidade de Vigo y el Laboratorio Oficial de Metroloxía de Galicia (LOMG). En estos proyectos se ha construido un prototipo de interferómetro Twyman-Green vertical encapsulado en un recinto termostático con dos longitudes de onda no estabilizadas. Se han desarrollado y caracterizado diversos tipos de algoritmos de desplazamiento de fase, tema que se aborda en apartados posteriores de esta tesis. También se ha realizado la estabilización de diodos láser rojos mediante la técnica de anclaje en frecuencia con celda de yodo y absorción saturada para evitar el efecto Doppler. Esta tarea estaría incluida en el plan de investigación de otro doctorando del equipo investigador por lo que no forma parte de esta tesis.

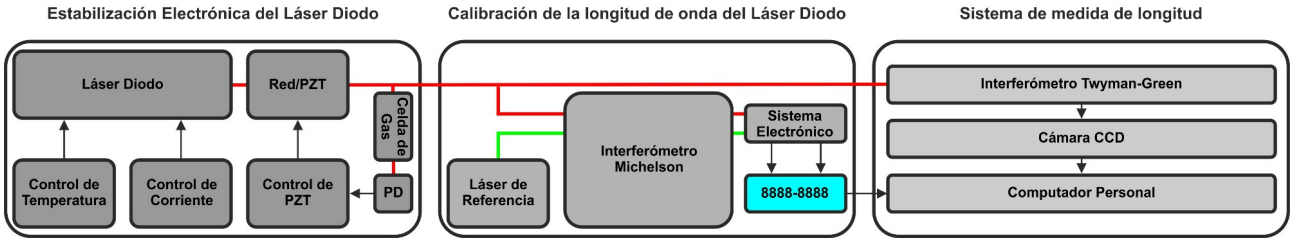

Fig. 1. Elementos del sistema de medida de Bloques Patrón

Una vez conseguida la estabilización de los diodos láser es preciso determinar la longitud de onda resultante con un margen de error reducido (inferior a 10^{-8} en el caso de la calibración de BPL). Los equipos comerciales en algunos casos no alcanzan la resolución requerida [33] o resultan demasiado costosos. Una solución es comparar el diodo láser con otro de referencia mediante un interferómetro tipo Michelson con un brazo móvil cuyo desplazamiento está controlado electrónicamente [34,35]. Ambos láseres producen simultáneamente franjas de interferencia que pueden ser captadas mediante fotodetectores, amplificadas y contadas durante un período de tiempo suficiente para que la relación numérica entre ambas proporcione la resolución requerida.

Uno de los objetivos de esta tesis es el desarrollo de prototipos y técnicas para automatizar la tarea de medición de longitud de onda, como se verá en apartados posteriores. Se ha desarrollado un nuevo prototipo basado en el método Vernier [36-38], mejorando y actualizando desarrollos anteriores.

También se ha desarrollado una nueva técnica de medida que hemos denominado "cuenta de multicoeficientes con restos fraccionarios" ("*multicoefficient fractional counting*") que combina y mejora métodos anteriores utilizando marcas de tiempo [39], multicoincidencias y multicoeficientes [40] y cálculo de restos fraccionarios de franjas de interferencia para mejorar la precisión [41].

Esta tesis doctoral se presenta en la modalidad de compendio de artículos y está formada por los trabajos que se indican a continuación, cuyos indicadores de calidad se detallan en apartados posteriores:

i. Javier Diz-Bugarin, Benito V. Dorrio, Jesus Blanco, Marta Miranda, Ismael Outumuro, Jose Luis Valencia, "Design of an interferometric system for gauge block calibration", Optical Engineering 52(4), 045601 (3 April 2013). https://doi.org/10.1117/1.OE.52.4.045601

ii. M. Miranda, B.V. Dorrio, J. Blanco, J. Diz-Bugarin, "Linear error analysis of differential phase shifting algorithms", Optik - International Journal for Light and Electron Optics, Vol. 124, Issue 8, 2013, pp. 710-717, ISSN 0030-4026. https://doi.org/10.1016/j.ijleo.2012.02.006

iii. M. Miranda, B.V. Dorrio, J. Blanco, J. Diz-Bugarin, F. Ribas, "Characteristic polynomial theory of two-stage phase shifting algorithms", Optics and Lasers in Engineering, Vol. 50, Issue 4, April 2012, Pages 522-528, ISSN 0143-8166. https://doi.org/10.1016/j.optlaseng.2011.09.002

iv. J. Diz-Bugarín, I. Outumuro-González, J. B. Vázquez-Dorrío, J. L. Valencia-Álvarez, J. Blanco-García, "Design of a New Microcontroller-Based Vernier Fringe Counter for Interferometric Measurement of Laser Wavelength", IEEE Transactions on Instrumentation and Measurement, Vol. 65, No. 2, pp. 407-412, Feb. 2016. https://doi.org/10.1109/TIM.2015.2482258

Además de las anteriores publicaciones se ha enviado otro artículo a la revista *Review of Scientific Instruments* que en el momento de depósito de esta tesis todavía no tiene aceptación definitiva para publicación. Este trabajo desarrolla la nueva técnica de medida de longitud de onda "cuenta de multicoeficientes con restos fraccionarios" (*multicoefficient fractional counting*).

1.2. REVISIÓN DE TÉCNICAS DE MEDIDA DE LONGITUD DE ONDA

Desde el punto de vista interferométrico, la longitud de onda de un láser desconocido se puede obtener por comparación con la longitud de onda de un láser de referencia en un interferómetro Michelson con brazo móvil, en donde los láseres son colineales y viajan caminos ópticos coincidentes. Un desplazamiento controlado de uno de sus espejos produce patrones de interferencia diferentes para cada láser. Las variaciones de amplitud correspondientes a las franjas interferenciales, una vez adquiridas por un sistema electrónico y convertidas de una señal analógica a pulsos digitales, pueden ser contadas por hardware o software. En ese caso, la razón entre las longitudes de onda del láser desconocido y el láser de referencia coincide con la razón entre el número de franjas producidas por la longitud de onda de referencia y desconocida [34-35]. Si no se asume el mismo índice de refracción para ambas longitudes de onda, se puede aplicar un factor de corrección para mejorar la precisión del cálculo de la longitud de onda. Esta precisión en la medida de la longitud de onda desconocida depende así de la relación entre el número de franjas de interferencia medidas que debe ser calculada con suficiente velocidad y resolución.

Existen diferentes técnicas que se emplean para la determinación de longitudes de onda desconocidas por comparación con longitudes de onda de referencia. Estas son:

Contador de franjas enteras

El tipo de medidor más simple es el propuesto por Fox et al. [36], diseñado para contar simultáneamente un número entero de franjas de ambos láseres. El sistema electrónico estaba hecho mediante contadores binarios y otros circuitos digitales básicos. En este caso, el error puede llegar a ser de un periodo completo, lo que se puede solucionar aumentando el número de franjas mediante un mayor desplazamiento del brazo móvil del interferómetro, lo cuál puede traer otro tipo de problemas como desalineamientos. Los autores han obtenido una precisión relativa de $3{,}8\text{x}10^{-6}$ para un número total de franjas de 650.000. Este sistema ha sido mejorado por Ugray et al. [42], utilizando un microcontrolador PIC18F1320 a 40 MHz.

Multiplicador de franjas con PLL

Una forma de aumentar el número de franjas y la resolución [34,43] es multiplicando la frecuencia de la señal de la franja mediante un lazo de fase o PLL. Este método requiere un control preciso del desplazamiento del brazo móvil del interferómetro para lograr una gran estabilidad de frecuencia de la señal de franjas. Usando un factor de multiplicación de 128, se han obtenido resoluciones en el rango de $8\text{x}10^{-9}$ con desplazamientos del interferómetro de 165 mm [43].

Método Vernier o de coincidencia de fase

El método Vernier [37] cuenta las franjas entre dos coincidencias de fase de las señales, reduciendo el error debido al truncamiento de N_R y N_U a números enteros. En este caso, la precisión depende de los circuitos electrónicos empleados para detectar la coincidencia de fase entre las señales. Este método tiene la desventaja de que la longitud de la medida queda limitada a puntos donde hay coincidencia de fase y si no se pueden detectar las coincidencias con exactitud la medida resulta imposible. Los autores han obtenido una precisión en el rango de $1\text{x}10^{-8}$, siendo la principal fuente de error el ruido de amplitud en los puntos de cruce por cero de las señales digitales.

Método de multicoincidencia

En Ishikawa [40] se describe una mejora del método Vernier que consiste en contar conjuntos de coincidencias de fase sucesivas. El sistema está compuesto por contadores y registros digitales que almacenan el número de franjas de cada entrada. Cada vez que hay una coincidencia, los valores de ambos contadores se envían a un ordenador. Al final del proceso, el ordenador ha almacenado un número total de *2N* coincidencias y calcula los coeficientes N_R/N_U para pares de valores separados por *N/2* coincidencias, promediando finalmente todos los coeficientes. Este método reduce el error en un factor $N^{1/2}$ y la incertidumbre en 1/500 de franja, obteniendo una resolución mejor que $1x10^{-9}$.

La principal desventaja de este sistema es la baja resolución de la lógica de detección (en torno a 300 ns) y el elevado tiempo de transmisión (15 ms), que limita el número de coincidencias que se pueden capturar y puede provocar pérdidas de datos.

Contador de franjas con restos fraccionarios

Bennet y Gill [41] han descrito una mejora del sistema que tiene en cuenta la parte fraccionaria de las franjas al principio y al final del desplazamiento. Para ello utilizaron contadores digitales de tres y siete dígitos, biestables y un oscilador de 5 MHz. El método consistía en contar el número entero de franjas con los contadores digitales de siete dígitos y medir los intervalos de tiempo entre los cruces por cero de ambas señales con los contadores de 3 dígitos. El circuito también medía el período inicial y final de las señales. Para una frecuencia de franjas máxima de 50 kHz y 1.000.000 de franjas, se puede lograr una resolución de 10^{-8}. Este método tenía las desventajas de su baja flexibilidad, baja resolución de franjas y que los circuitos lógicos sólo podían almacenar un máximo de 6 parámetros correspondientes al número total de franjas y partes fraccionarias al inicio y al final de la cuenta. Cualquier mejora de estas limitaciones implicaba un rediseño completo del sistema de medición.

Monchalin et al. [44] mejoraron este método usando un ordenador PDP12 y un reloj de cristal para calcular las diferencias de fase. Este método obtenía medidas locales en diferentes momentos durante el desplazamiento del interferómetro para comprobar la incertidumbre del proceso. Como desventaja se puede comentar que el hardware empleado es muy antiguo. La frecuencia de reloj era de unos pocos cientos de kHz, mejor que el reloj de 50 kHz utilizado por Bennet y Gill. Con estas mejoras lograron una resolución de $2x10^{-9}$.

Método de las marcas de tiempo

Pedregosa et al. [39] propusieron un nuevo método para la medición de fase utilizando sistemas comerciales de adquisición de datos que permiten el almacenamiento de marcas de tiempo para cada pulso de las franjas de entrada. Utilizaron un interferómetro con un desplazamiento de 40 cm y una placa de adquisición PCIe-6363 combinada con un contador digital HM-8122 como adaptador para convertir los pulsos analógicos en una señal digital. La placa de adquisición tenía una frecuencia de reloj interno de 100 MHz que permite una resolución de tiempo de 10 ns. La memoria interna de la tarjeta almacenaba las marcas de tiempo de ambos pulsos de señal, lo que proporciona información sobre el número total de franjas, así como las diferencias de tiempo al principio y al final de la adquisición. Los autores obtuvieron una precisión de 10^{-8} (modo de alta velocidad) y 10^{-10} (modo de baja velocidad). La principal ventaja de este método es que proporciona una gran cantidad de información que puede utilizarse para verificar la fiabilidad de las medidas. Su desventaja es el alto precio de los equipos (tarjeta de adquisición y contador digital) que podrían ser

reemplazados por circuitos electrónicos más económicos.

1.3. MÚLTIPLES MEDICIONES CONSECUTIVAS PARA REDUCIR LA INCERTIDUMBRE

Partiendo del prototipo Vernier desarrollado como parte de esta tesis es posible reducir la incertidumbre utilizando múltiples mediciones consecutivas. Este sistema y el prototipo asociado se basa en los métodos de marcas de tiempo [39] y multicoincidencia [40], con un hardware compuesto por una placa de control con microcontrolador y un módulo contador de alta velocidad. El módulo de contador de alta velocidad utiliza registros y contadores para adquirir las marcas de tiempo con la resolución de tiempo requerida y transferir datos al microcontrolador. Este enfoque permite el uso de microcontroladores con una amplia gama de velocidades de procesamiento, elimina los requisitos de tiempo real y simplifica el desarrollo de software. Este módulo alcanza resoluciones de 10 ns para un oscilador de 100 MHz y podría mejorarse mediante el uso de familias lógicas más rápidas y frecuencias de reloj más altas.

El método de medida se ha denominado "cuenta de multicoeficientes con restos fraccionarios" ("*multicoefficient fractional counting*"), mejora la resolución y elimina algunas de las desventajas de los métodos tradicionales antes mencionados, con menor costo y mayor flexibilidad. El método cuenta las partes fraccionarias de las franjas como en Bennet y Gill [41] y también usa marcas de tiempo como Pedregosa et al. [39] en un proceso de medición similar al método de multicoincidencia de Ishikawa [40] pero sin necesidad de esperar coincidencias de fase, lo que permite iniciar y finalizar el proceso de captura en cualquier punto del desplazamiento del interferómetro. Esto maximiza la longitud de medición del interferómetro y reduce la complejidad del hardware porque no hay necesidad de detectar las coincidencias de fase con alta precisión.

La Fig. 2 representa la posición de las marcas de tiempo empleadas, siendo λ_U y λ_R las longitudes de onda desconocida y de referencia, t_U y t_R los conjuntos de marcas de tiempo desconocidas y de referencia, y N y M los números enteros de franjas de las señales desconocida y de referencia.

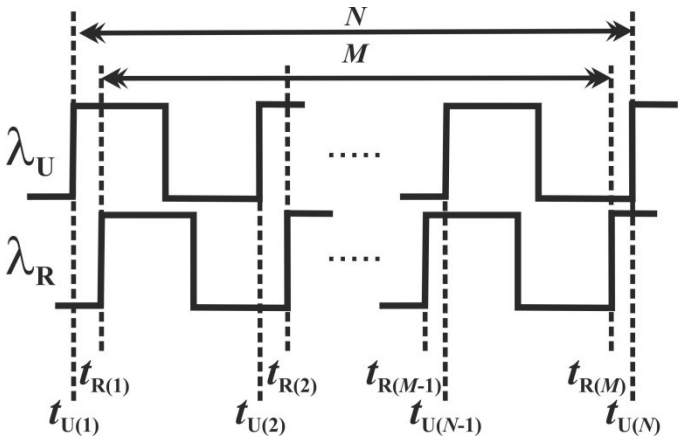

Fig. 2. Detalle de las marcas de tiempo empleadas en el cálculo

El cálculo de λ_U o λ_R se efectúa mediante las ecuaciones (1) o (2). La diferencia entre ambas ecuaciones puede emplearse como una medida de incertidumbre del proceso. Esto es una mejora respecto de los sistemas de Bennet-Gill y Pedregosa, que siempre usan una de las señales como referencia y calculan la parte fraccionaria de la otra.

$$\lambda_U N = \lambda_R \left(M + \frac{t_{R(1)} - t_{U(1)}}{t_{R(2)} - t_{R(1)}} + \frac{t_{U(N)} - t_{R(M)}}{t_{R(M)} - t_{R(M-1)}} \right) \quad (1)$$

$$\lambda_R M = \lambda_U \left(N + \frac{t_{R(1)} - t_{U(1)}}{t_{U(2)} - t_{U(1)}} + \frac{t_{U(N)} - t_{R(M)}}{t_{U(N)} - t_{U(N-1)}} \right) \quad (2)$$

El sistema también puede adquirir marcas de tiempo en cualquier momento durante la medida, lo que permite verificar la frecuencia local de las franjas, controlar la velocidad de desplazamiento y verificar el ruido y la calidad de las franjas. Las marcas de tiempo también se pueden utilizar para detectar coincidencias de fase (como en el método Vernier), con la ventaja de que el sistema puede calcular la fase instantánea e incluso predecir las coincidencias futuras. Si se almacenan muchas marcas de tiempo durante el proceso de lectura, la información proporcionada se puede usar para calcular una gran cantidad de coeficientes en lugar de un solo valor con los datos inicial y final.

Este método ha sido utilizado por Ishikawa [40], pero solo entre puntos de coincidencia en las señales. En este caso los cálculos se realizan con un número elevado de conjuntos de marcas de tiempo con una separación superior a 10^6 franjas para tener una buena resolución en el cálculo, teniendo en cuenta además los restos fraccionarios inicial y final. Finalmente se obtiene el valor medio de todos los coeficientes calculados para reducir el error como en el método de Ishikawa.

Este diseño implementa el método de marcas de tiempo con un módulo electrónico compuesto por un microcontrolador de propósito general y un circuito electrónico de interfaz compuesto por un conjunto doble de contadores y registros, que almacenan las marcas de tiempo de cada pulso de entrada de ambas señales. Estos valores son leídos por el microcontrolador que crea un registro para cada marca de tiempo que incluye el tiempo de adquisición y el número de franja. Este método combina la alta velocidad de los contadores hardware y la flexibilidad del microcontrolador con buen rendimiento y a un coste reducido. En las Fig. 3 y 4 se representa el diagrama de bloques del sistema y el módulo de interfaz, y en la Fig. 5 el esquema electrónico detallado de este módulo.

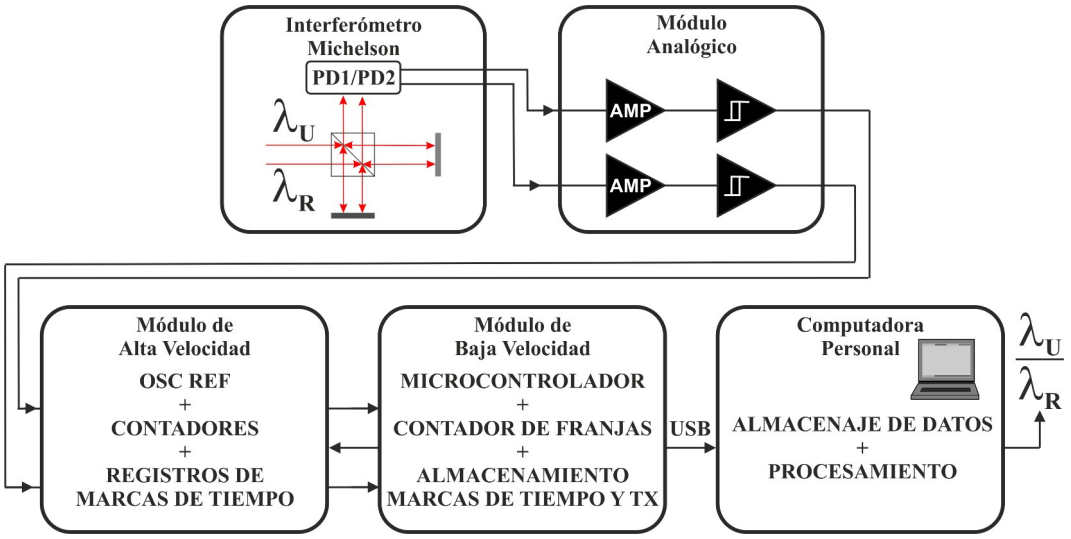

Fig 3. Diagrama de bloques del sistema de medida

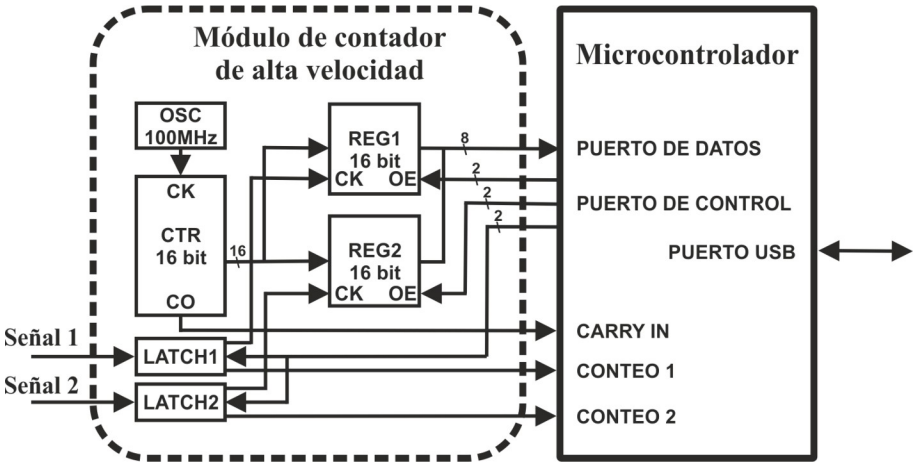

Fig 4. Elementos del módulo de interfaz

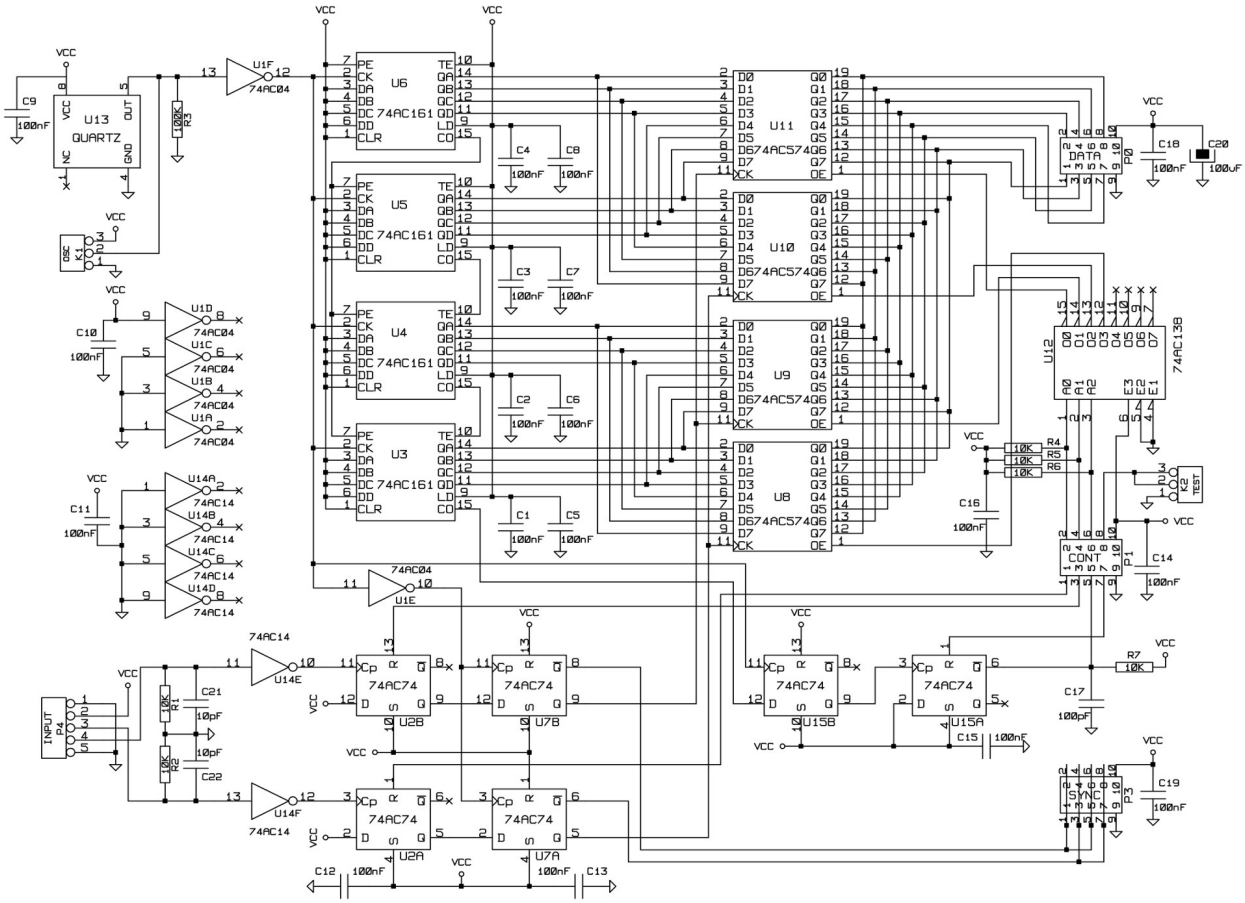

Fig. 5. Esquema electrónico del módulo de interfaz.

La resolución del sistema depende del período del oscilador principal (10 ns para un cristal de 100 MHz). Este valor podría incrementarse en futuras versiones del hardware para mejorar la resolución del sistema o reducir el tiempo de adquisición. El proceso de adquisición almacena un grupo de 16 marcas de tiempo consecutivas para cada canal, que se envían al ordenador para su

almacenamiento. Este método de medición requiere un pequeño espacio de memoria en el microcontrolador, mientras que el ordenador recibe y procesa una gran cantidad de datos que nos permiten realizar cálculos precisos de longitud de onda. El primer y último conjunto de marcas de tiempo tienen la información requerida para calcular las partes fraccionarias de las franjas como en el método Bennet-Gill [41]. De esta forma la resolución no está limitada por el número de dígitos de los contadores, de hecho, podría ser tan grande como se desee reduciendo la frecuencia de la franja. Este método no requiere una velocidad constante del interferómetro o una frecuencia constante en las señales de entrada porque cada conjunto de marcas de tiempo proporciona información sobre la frecuencia local en cualquier momento durante la adquisición. Esta información se puede utilizar como medida de calidad de las señales de entrada o para controlar la velocidad del brazo móvil del interferómetro.

El proceso de prueba electrónica del módulo de alta velocidad se ha diseñado cuidadosamente en varios pasos: una verificación inicial del hardware para asegurarse de que todos los circuitos funcionan correctamente y envían datos al microcontrolador, un programa de autodiagnóstico en el que el microcontrolador genera pulsos de señal para el módulo de alta velocidad y lee los datos, y finalmente pruebas con osciladores externos simples y dobles. Los resultados han servido para detectar algunos problemas en el diseño y se ha realizado una nueva versión de la placa para corregirlos. En estas pruebas se han aplicado una o dos señales digitales externas a las entradas para calcular su relación de frecuencia. Para estas pruebas hemos utilizado el módulo auxiliar descrito en el apartado dedicado al prototipo Vernier y generadores digitales de señales comerciales. En cada medida se han almacenado un mínimo de 1000 conjuntos de marcas, calculado los coeficientes de frecuencia correspondientes y promediado todos ellos para reducir la variabilidad, resultando márgenes de error en el entorno 10^{-13}, lo que demuestra el correcto funcionamiento de este nuevo método. En la Fig. 6 se representa el resultado de una de las medidas realizadas con dos frecuencias diferentes y en la Fig. 7 la distribución estadística de la relación de coeficientes.

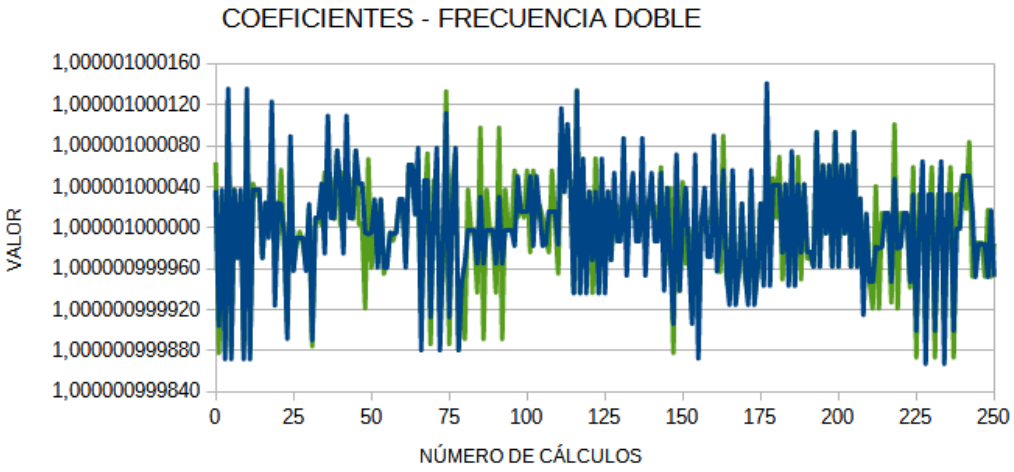

Fig. 6. Medidas con dos frecuencias diferentes

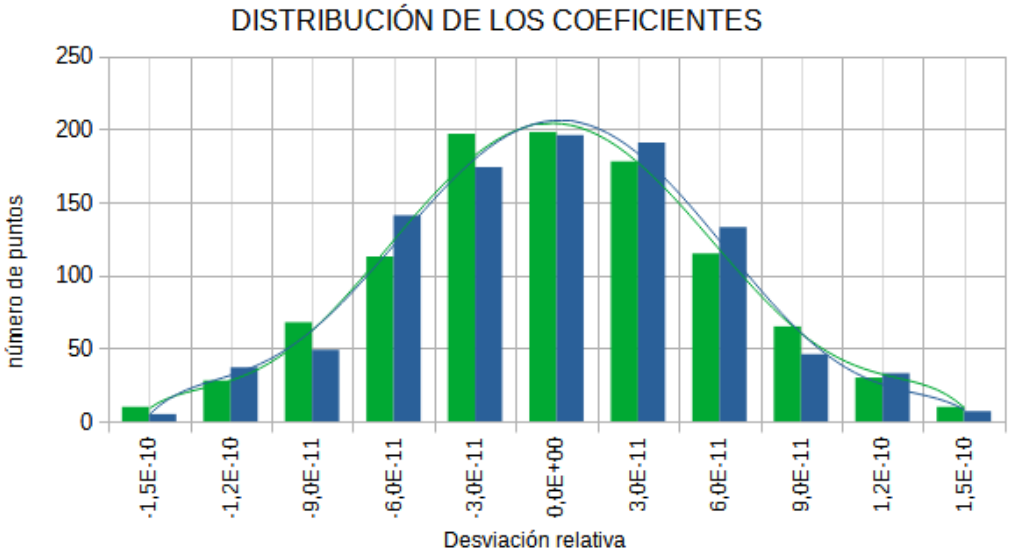

Fig. 7. Distribución estadística de los coeficientes

1.4. MOTIVACIÓN Y OBJETIVOS

MOTIVACIÓN

Un proceso de calibración fiable, rápido y económico de Bloques Patrón Longitudinales es un elemento fundamental para el aseguramiento de la calidad de los procesos en la industria mecánica moderna. Su medida precisa requiere un control fino de las magnitudes de influencia que juegan un papel en el proceso metrológico. En el ámbito de la interferometría buena parte de la tecnología de adquisición y evaluación de la fase óptica se ha universalizado convirtiéndose en un estándar en el ámbito industrial. Lo mismo ocurre en el contexto del control termodinámico de recintos, en donde la tecnología actual de sensores permite un control en tiempo cuasi real del medio con altísima precisión. Muchas de estas herramientas pueden ser ahora implementadas de forma directa en los procesos de calibración y trazabilidad de los centros de referencia metrológicos. Sin embargo uno de los principales inconvenientes para poder llevar a cabo este salto desde los centros de investigación es el muchas veces prohibitivo uso de los necesarios láseres gaseosos estabilizados. Una solución sería emplear como fuentes de iluminación láseres de diodo estabilizados (robustos y de bajo coste) como los que se emplean en las trampas magnetoópticas para el enfriamiento de átomos en los Laboratorios de Física Fundamental.

Así pues un sistema completo de calibración de BPL mediante interferometría requiere una capacidad investigadora, temporal y de personal muy elevada por lo que la parte principal de esta tesis se centra en el desarrollo del sistema electrónico de medición de longitud de onda de los diodos láser estabilizados que se pretenden utilizar como referencia, pieza fundamental para conocer en cual de las líneas de absorción de la celda de gas se ha anclado el diodo láser y para dar trazabilidad a su longitud de onda. Además de lo anterior en esta tesis se han abordado otras partes del sistema completo, como la integración y automatización de elementos del interferómetro de

medida por desplazamiento de fase, la lectura del conjunto de sensores que garantizan la estabilización de los parámetros ambientales para el control del índice de refracción que permite el cálculo preciso de la longitud de onda, los procesos de adquisición y tratamiento de imágenes de fase y el estudio de los algoritmos empleados.

OBJETIVOS

Los objetivos concretos de la presente tesis son:

O1. Diseño general de un sistema de medida interferométrico para Bloques Patrón Longitudinales.

O2. Programación de un entorno de control que integra todos los elementos: parámetros ambientales del recinto estabilizado (temperatura, humedad, presión), control de desplazamiento del actuador piezoeléctrico para adquisición de imágenes de fase, lectura de cámara, adquisición y almacenamiento de imágenes, módulo de combinación de conjuntos de imágenes según diferentes algoritmos de fase y presentación de resultados.

O3. Estudio y caracterización de diversos tipos de algoritmos de evaluación de fase y de diferencia de fase. Obtención de mapas de fase reconstruídos y análisis de posibles fuentes de error en los algoritmos.

O4. Diseño, realización y verificación de prototipo de medidor de longitud de onda basado en el método Vernier.

O5. Diseño, realización y verificación de nuevas técnicas de medida de longitud de onda con características mejoradas.

1.5. ESTRUCTURA

Esta tesis doctoral se presenta por compendio de artículos, siendo cuatro los publicados a la fecha, que se completan con una veintena de presentaciones en congresos nacionales e internacionales, algunos de los cuales son referencia en el ámbito con actas indexadas en SCOPUS, JCR o SCR. Definidas en el capítulo 1 las complejidades del contexto de la medida interferométrica de longitudes de BPL, la revisión actualizada de las técnicas de medida de longitud de onda, la estrategia de reducción de incertidumbre en la medida utilizando múltiples mediciones consecutivas y la motivación y objetivos de la tesis doctoral, se presentan los correspondientes artículos agrupados temáticamente por capítulos como sigue:

Capítulo 2. Diseño del sistema interferométrico para la calibración de Bloques Patrón Longitudinales.

Este Capítulo 2 consta de un artículo de revista ("*Design of an interferometric system for gauge block calibration"*) y en él se aborda el diseño general de un sistema de medida de Bloques Patrón

Longitudinales (BPL) mediante interferometría. Se ha diseñado y construido un interferómetro de tipo Twyman-Green en configuración vertical con doble fuente láser (He-Ne de 632.8 nm y 543.2 nm). En uno de los brazos se sitúa una superficie óptica de referencia y en el otro el bloque patrón sobre una superficie de soporte de referencia, de forma que los frentes de onda provenientes de ambos brazos se superponen. Se utiliza el método de los excedentes fraccionarios para el cálculo de la longitud del bloque como un múltiplo de la semilongitud de onda del láser.

La adquisición de imágenes de fase se realiza mediante dos cámaras, una 2M-XLI (RGB) o una Thorlabs-DCC1545M (monocromática). La modulación optomecánica se lleva a cabo mediante un posicionador piezoeléctrico Physik Instrumente P-733.ZCL, que tiene un rango de desplazamiento de 100 μm y una resolución de 0,3 nm. El sistema de control y evaluación está compuesto por un ordenador con un programa propio escrito en C++, que controla los diferentes módulos de posicionamiento, adquisición, procesamiento y cálculo de la fase óptica en tiempo casi real utilizando Algoritmos de Desplazamiento de Fase, pudiendo escoger algoritmos convencionales o crear nuevos algoritmos experimentales. El sistema recibe información de los módulos de medida para realizar el cálculo del coeficiente de refracción del aire.

El interferómetro se ha encapsulado en una carcasa termostática formada por perfiles de aluminio que alojan un serpentín de cobre recubierto de aislante. Las paredes actúan como intercambiadores de calor entre el serpentín de cobre y el interior de la carcasa. Un circulador de agua Julabo F25MC con control PID mantiene la temperatura estable en el interior del recinto, y los sensores envían información al equipo de control a través de un un puente de termometría ASL 600 DC F600 y un medidor Vaisala PTU3030.

La estabilización del diodo láser se ha realizado en configuración de Littrow controlando el ángulo de una red de difracción, la ultraestabilización mediante una técnica de bloqueo de modo con una celda de gas de referencia. Se ha empleado un haz láser de saturación para saturar la celda y evitar el efecto láser Doppler. Las variaciones de frecuencia del láser se convierten en variaciones de amplitud en el fotodetector, debido a la absorción selectiva de la celda de gas. Esta señal electrónica se envía a un equipo de control Moglabs DLC-202, que varía el ángulo de la red mediante un actuador piezoeléctrico.

Para evitar vibraciones mecánicas y gradientes de temperatura y mantener la cavidad resonante del láser a una temperatura constante, se diseñó un sistema mecánico encapsulado y aislado con elementos de inercia que incorpora sensores NTC y celdas Peltier.

El sistema se ha verificado mediante medidas de larga duración, lo que ha demostrado su viabilidad para la estabilización de los diodos láser. El siguiente paso es la medida precisa de la longitud de onda resultante para que se pueda utilizar en el sistema de medida de BPL. Por último, se integrarán estos elementos en un sistema de medición dimensional de BPL automatizado que emplee diodos láser robustos y económicos como fuentes de luz.

Capítulo 3 Estudio de algoritmos diferenciales de desplazamiento de fase para medidas de BPL.

Este Capítulo 3 consta de dos artículos de revistas (Secciones 3.1, "*Characteristic polynomial theory of two-stage phase shifting algorithms*", y 3.2, "*Linear error analysis of differential phase shifting algorithms*") y se analizan los necesarios procesos de decodificación de los patrones de franjas proporcionados por el sistema interferométrico para la calibración de un BPL, un sistema de campo completo y doble haz que presenta la información del mensurando en la fase de una distribución de irradiancia bidimensional de perfil sinusoidal. El proceso decodificador supone en la

mayoría de los casos la combinación de al menos tres valores de irradiancia desplazados en fase en el argumento de una función trigonométrica inversa para recuperar la fase del patrón franjas con los conocidos Algoritmos de Desplazamiento de Fase (ADF). Este proceso presenta sensibilidades a diversas fuentes de error (modulador de fase, presencia de armónicos de orden superior, …) y requieren además, puesto que se recuperan los valores de fase óptica módulo 2π, de un proceso de reconstrucción para asignar el orden correcto de las franjas. Este último proceso se vuelve delicado y limitante cuando los valores de irradiancia presentan ruido, baja modulación, muy baja densidad de muestreo, pero sobre todo cuando muestran cambios abruptos de fase como ocurre en la medida de un BPL. No existe un algoritmo que resuelva todas las posibles problemáticas asociadas a un proceso interferométrico de medida particular siendo por ello necesario su análisis e implementación experimental para elegir aquel que minimice las posibles fuentes de error.

Por otra parte, la información del mensurando de interés puede estar asociada a la diferencia de fase óptica codificada entre el patrón de franjas original y otro patrón modificado siendo posible el cálculo de la diferencia de fase empleando dos ADFs para calcular explícitamente la fase de cada patrón y finalmente sustraerlas para recuperar su diferencia. De la misma forma que se recupera la diferencia de fase entre los dos patrones se puede requerir también de la fase suma de ambos, algo que puede entenderse en ciertos casos como un promediado de algoritmos que disminuye la influencia de los errores que pueden afectar al cálculo directo y que es también de interés para la medida de BPL en tanto en cuanto reduce el error asociado al empleo de los ADFs en el cálculo de incertidumbre final de la medida.

Sin embargo, se puede realizar un cálculo directo de la diferencia de fase, evitando incluso el delicado proceso de reconstrucción cuando esta no alcanza un periodo completo, si patrones de franjas desplazados originales y modificados se combinan directamente en un Algoritmo Diferencial de Desplazamiento de Fase (ADDF), que puede ser obtenido sistemáticamente mediante un ajuste de mínimos cuadrados. Este proceso diferencial resulta de utilidad en procesos de calibración y análisis de estabilidad, repetibilidad y reproducibilidad, como los necesarios en la medida de BPL, siendo necesario en cualquier caso para la evaluación experimental de la incertidumbre combinada de la medida de acuerdo con todos los factores que contribuyen durante el proceso de medida y la función modelo correspondiente.

Es necesario, pues utilizar algún mecanismo de diseño definido y un análisis de sensibilidades de los posibles algoritmos a emplear en nuestra particular aplicación de medida de BPL, para detectar las posibles fuentes de error en el cálculo y obtener luego la fase con el menor error posible. Este diseño previo y posterior caracterización cualitativa de los ADDF se realiza relacionando el cálculo con la obtención de la fase del número complejo asociado en función del Polinomio Característico del ADDF. En este caso la multiplicidad y localización de las raíces del Polinomio Característico indican la sensibilidad a las posibles fuentes de error así como sus capacidades compensatorias. Una vez seleccionados los algoritmos que mejor comportamiento de insensibilidad y compensación presentan para nuestra aplicación particular se obtiene un resultado cuantitativo del error asociado fácilmente comparable entre los diferentes algoritmos seleccionados utilizando un proceso de linealización, obteniendo expresiones analíticas del error que podrían ser empleadas en procesos posteriores de reducción y/o análisis del error.

Los resultados obtenidos, en lo que se refiere al control de modulación, sincronización de adquisición, tratamiento de imagen y procesamiento de algoritmos de desplazamiento de fase, tanto de desarrollo propio como publicados en la literatura, muestran protocolos validados para la elección adecuada del algoritmo a emplear en la evaluación de la fase para la calibración de Bloques Patrón Longitudinales.

Capítulo 4. Diseño de un medidor interferométrico de longitud de onda con microcontrolador mediante el método Vernier.

El Capítulo 4 consta de un artículo de revista ("*Design of a New Microcontroller-Based Vernier Fringe Counter for Interferometric Measurement of Laser Wavelength"*) y en él se describe un nuevo sistema electrónico de medida de longitud de onda mediante el método Vernier con interferómetro Michelson de brazo móvil para verificar la estabilización de diodos láser de cavidad extendida (ECDL). Este sistema utiliza un microcontrolador combinado con circuitos CMOS de alta velocidad para alcanzar la resolución temporal requerida en la detección de conincidiencias. El sistema desarrollado ha mejorado la resolución de otros sistemas anteriores.

Un láser He-He calibrado se utiliza como referencia y el láser ECDL como fuente desconocida. El desplazamiento del brazo móvil del interferómetro se consigue mediante una mesa de velocidad constante Thorlabs DDS220/M. Este equipo tiene un desplazamiento máximo de 220 mm, que resulta suficiente para la adquisición de alrededor de 1.400.000 franjas de interferencia para longitudes de onda de 633 nm en un único recorrido.

El sistema electrónico se divide en cuatro módulos: un módulo analógico, un módulo de interfaz digital que incorpora el detector de coincidencia, un módulo de control y un generador auxiliar.

El módulo analógico consta de dos secciones idénticas con un fotodiodo, amplificador de transimpedancia, un preamplificador de tensión con filtro, un amplificador de ganancia variable y un comparador. Se han realizado muchas pruebas para verificar su fiabilidad y bajo nivel de ruido. Este módulo va alojado en el interferómetro y va conectado por cable con el resto del sistema.

El segundo módulo del sistema electrónico es la interfaz digital y el detector de coincidencias. El módulo de interfaz digital proporciona la señal de entrada al microcontrolador y realiza la detección de coincidencia de franjas para iniciar y detener las mediciones de franjas según el método Vernier. Este circuito ha mejorado diseños anteriores que utilizaban contadores hardware, que se han sustituido por un microcontrolador. El detector de coincidencias se ha realizado mediante circuitos de alta velocidad y genera una señal de interrupción para los contadores software del microcontrolador.

El módulo de control se ha diseñado con un microcontrolador que implementa la interfaz de usuario, contador de franjas, detector Vernier y comunicaciones. Los microcontroladores utilizados pertenecen a la familia MCS-51 de Atmel (AT89S4051 o AT89S52). Estos microcontroladores tienen contadores hardware de 16 bits de alta velocidad, que se han ampliado a 32 bits por software usando interrupciones, por lo que el tiempo de adquisición puede extenderse hasta donde sea preciso para tener suficiente resolución de cuenta. El módulo tiene una conexión USB para ISP, control remoto y transferencia de datos a un ordenador externo. También se ha utilizado una placa de interfaz con pantalla LCD y un pequeño teclado para funcionamiento autónomo.

El módulo generador auxiliar se ha desarrollado para disponer de señales de prueba electrónicas y ópticas para verificar la precisión y fiabilidad de los contadores de franjas antes de integrarlos en el sistema real con interferómetro. Este módulo tiene dos osciladores de cristal de cuarzo con un componente ajustable que puede variar ligeramente la frecuencia y un contador binario para seleccionar el rango de salida. Cada oscilador se puede ajustar de forma independiente.

La resolución del medidor queda limitada por dos factores, el número de dígitos del visualizador y el número de bits del contador software. Con 10 dígitos y 32 bits la resolución puede alcanzar 0,00023 ppm, suficiente para las aplicaciones propuestas. Este diseño mejora la resolución de los

diseños anteriores que tenían sólo ocho dígitos o menos, pero aún así podría aumentarse mediante la reprogramación del sistema en caso necesario.

La principal fuente de error en la cuenta simultánea de franjas se debe al truncamiento de la parte fraccionaria de las franjas al inicio y al final del período de cuenta. Para lograr una resolución de 0,01 ppm, se debe adquirir un número mínimo de 10^8 franjas. Para una longitud de onda del láser de 633 nm, en el interferómetro empleado se requiere un recorrido del brazo móvil de 158 mm para obtener sólo 10^6 de franjas. El uso del método Vernier reduce el número de franjas necesarias para lograr la misma resolución. Con este método, el número de franjas en cada canal es siempre un valor entero, eliminando la mayor parte del error. La principal fuente de error en este caso se debe a la resolución temporal del circuito electrónico, y también está relacionada con la frecuencia de las franjas. En nuestro prototipo, la resolución temporal del detector de coincidencia electrónica es de 100 ns. Si la frecuencia de franja es inferior a 100 kHz, el intervalo entre franjas es superior a 10 μs y la resolución es mejor que 0,01 franjas. Si el número total de franjas es superior a 1.000.000, se puede lograr una resolución total de 0,01 ppm.

Tras la integración con el interferómetro realizamos dos tipos de medidas: en primer lugar el láser de referencia se dividió en dos haces y se aplicó en las dos entradas del interferómetro, dando el mismo número de franjas en ambos canales del contador. Esta primera medida sirvió como verificación del correcto funcionamiento del sistema hardware-software.

En la segunda medición, se utilizaron dos láseres diferentes, un láser de referencia (REO Modelo 32734, calibrado por el CEM-Madrid-España) y uno desconocido (HP 5519A). En este caso, la longitud de onda medida fue de 632,99141 nm con una incertidumbre de 0,00016 nm (0,26 ppm), lo que concuerda con los valores de 632,9913867 nm y 0,000013 nm obtenidos por el Laboratorio de Metrología de la ETSII de la Universidad Politécnica de Madrid.

Por último, se utilizó el ECDL como láser desconocido y el modelo REO 32734 como láser de referencia. Estos resultados de longitud de onda e incertidumbre fueron 632,9922 nm y 0,0013 nm (2,0 ppm), respectivamente, demostrando la utilidad del medidor en un caso real con diodo láser estabilizado.

CAPÍTULO 2. DISEÑO DEL SISTEMA INTERFEROMÉTRICO PARA LA CALIBRACIÓN DE BLOQUES PATRÓN LONGITUDINALES

RESUMEN

Hemos desarrollado un interferómetro para la calibración de bloques patrón basado en algoritmos de desplazamiento de fase. El proceso de medición puede proporcionar planitud, paralelismo y longitud. Los valores de longitud de onda deben ser corregidos de acuerdo con el índice de refracción del aire. Esta corrección se obtiene indirectamente usando la ecuación de Edlén. Un conjunto de sensores de alta resolución proporcionan medidas de temperatura, presión y humedad relativa. Para preservar la estabilidad, el interferómetro está encapsulado en una cámara con control de temperatura activo. Se analiza el diseño, principio de medida, calibración, estabilidad y reproductibilidad. Dado que uno de los objetivos es emplear láseres de diodo robustos y baratos como fuentes luminosas, se describe el sistema desarrollado para estabilizar un diodo láser rojo usando la técnica de bloqueo de modo con una celda de gas como referencia. El montaje evita el efecto Doppler en la celda de gas, que podría limitar la resolución de la longitud de onda. Se han realizado pruebas para reducir la influencia de los cambios ambientales, que afectan la frecuencia del diodo láser.

PALABRAS CLAVE

Phase shifting; gauge block; optical standards and testing; metrology; external cavity diode laser; iodine cell.

PUBLICACIÓN ORIGINAL

Javier Diz-Bugarin, Benito V. Dorrio, Jesus Blanco, Marta Miranda, Ismael Outumuro, Jose Luis Valencia, "*Design of an interferometric system for gauge block calibration*", Opt. Eng. 52 (4) 045601 (3 April 2013) https://doi.org/10.1117/1.OE.52.4.045601

Optical Engineering 52(4), 045601 (April 2013)

Design of an interferometric system for gauge block calibration

Javier Diz-Bugarín
Benito V. Dorrío
Jesús Blanco
Marta Miranda
University of Vigo
Applied Physics Department
Campus Universitario
36310 Vigo, Spain
E-mail: jbugarin@uvigo.es

Ismael Outumuro
José Luis Valencia
Laboratorio Oficial de Metroloxía de Galicia
R&D Department, Parque Tecnolóxico de Galicia
32901 Ourense, Spain

Abstract. We have developed an interferometer for gauge block calibration based on phase shifting algorithms. The measurement process can provide flatness, parallelism, and length. Wavelength values need to be corrected according to the refractive index of air. This correction is obtained indirectly using Edlén's equation. High-resolution sensors provide the temperature, pressure, and relative humidity readings. To preserve stability, the interferometer is encapsulated in a chamber with active temperature control. Its design, measurement principle, calibration, stability, and reproducibility are analyzed. Since one goal is to employ robust and cheap diode lasers as light sources, we describe the system developed to stabilize a red laser diode using a mode locking technique with a reference gas cell. The instruments and assembly are used to avoid the Doppler effect in the gas cell, which would limit wavelength resolution. Several experiments are carried out to restrict the influence of environmental changes, which affect laser diode frequency. [DOI: 10.1117/1.OE.52.4.045601]

Subject terms: phase shifting; gauge block; optical standards and testing; metrology; external cavity diode laser; iodine cell.

Paper 130130P received Jan. 24, 2013; revised manuscript received Mar. 6, 2013; accepted for publication Mar. 12, 2013; published online Apr. 3, 2013.

1 Introduction

Procedures for ensuring industrial quality require metrological calibration processes that guarantee the traceability of the reference magnitudes for the measurement instruments. In dimensional metrology, gauge blocks (GBs) materialize the unit length or its submultiples, where the length of the GB is considered to be the perpendicular distance between two gauging surfaces. The traditional interferometric configuration used for this purpose employs two or more gas laser sources that are frequency stabilized, and it needs a housing capsule for the interferometric module with control over temperature, relative humidity, and atmospheric pressure (typical uncertainties are below 0.1°C in temperature, 1% in relative humidity, and 0.1 mbar in pressure).[1] These values are used to monitor the temperature of the measured GBs (at the reference temperature of 20ºC, according to ISO 3650:1998) and to calculate the air refractive index using a modified version of Edlén's equation,[2–4] because the refractive index determination is a crucial part of the gauge block calibration procedure.[5] To preserve the stability conditions, the interferometer is encapsulated within an insulated chamber with an active temperature control. Therefore, it is necessary to develop an electronic control system which manages the position of the GBs, the optical phase modulation, the image processing system, and the CCD camera to obtain the optical phase by means of the appropriate combination of the interferograms modulated in phase. Because they affect the measurement of the length, problems associated with this interferometric process should be also considered, such as variations in contact layer thickness, phase shift corrections, environmental variations, and geometrical deviations.

This work reports on the advance of the design and construction of an interferometric device, its thermostatic housing, and its refractometric module, paying attention to the operation and stability of the most determinant variables. Calibration of the optomechanical modulator is done by using differential phase shifting algorithms[6–8] (DPSAs), while the experimental values of the refractive index of air are compared with those provided by the National Institute of Standards and Technology[9] (NIST).

The experimental setup is related to the red diode laser stabilization using a mode-locking frequency technique, which is also presented. Since the results show a suitable frequency stabilization of the diode laser, this stabilized red laser diode will be integrated later in the interferometric optical phase evaluation system.

2 Principle of Measurement

Figure 1 shows the interferometer configuration employed to determine the GB's length. As can be seen, the GB is placed on a reference support surface (RSS) in such a way that the wavefronts reflected from the GB and the reference optical surface (ROS) coming from the other interferometric arm are superimposed. With this arrangement, the longitudinal length of the GB can be estimated by fractional excess[10] as a multiple of the semiwavelengths contained in its length. That is,

$$L = \frac{\lambda_1}{2}(m_1 + F_1) = \cdots = \frac{\lambda_j}{2}(m_j + F_j), \tag{1}$$

where L is the length of the GB, λ_j represents the laser wavelength, m_j represents a whole number of fringes, and F_j is

0091-3286/2013/$25.00

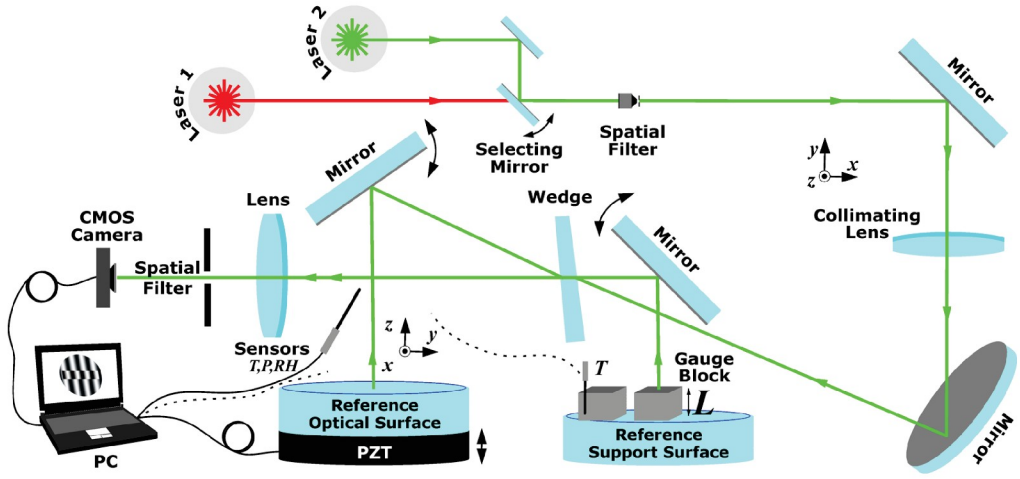

Fig. 1 This experimental setup uses the following principal elements: double He-Ne illumination (632.8 and 543.2 nm); Zerodur mirrors with a flatness of $\lambda/20$; 2M-XLI (CMOS-RGB) and Thorlabs-DCC1545M cameras; a PZT Physik Instrumente P-733.ZCL piezo nanopositioner; a Julabo F25MC circulator; an ASL 600 DC F600 thermometry bridge; and a Vaisala PTU 3030 barometer.

the fractional excess or the decimal part of these semiwavelengths. It is necessary to iterate the results obtained with several laser wavelengths, because a unique wavelength does not allow us to calculate the total number of semiwavelengths of the assessed GBs. This interferometric process requires the frequency stabilization of the laser to correct the theoretical wavelength of the source from vacuum to air values. Therefore, the refractive index [at temperatures near 20°C (68°F)] for each wavelength n_j of the interferometer is accurately controlled using Eldén's experimental equation[2–4] as

$$(n_j-1)\cdot 10^8 = \left(8342.54+\frac{2406147}{130-\lambda_j^{-2}}+\frac{15998}{38.9-\lambda_j^{-2}}\right)\cdot\left(\frac{P}{96095.43}\right)\left[\frac{1+10^{-8}(0.601-0.00972T)P}{1+0.0036610T}\right]-\mathrm{RH}(8.753+0.036588T^2)\times(0.037345-0.000401\lambda_j^{-2}), \quad (2)$$

once the temperature T, the atmospheric pressure P, and the relative humidity RH are known. The influence of the CO_2 composition is not considered. Ciddor's experimental equation[11] provides similar results at our working temperature, and it should give better results for the refractive index of air than Eq. (2) over a broader range of wavelengths and under severe environmental conditions of temperature, pressure, and humidity.[9]

What is more, the fractional excess is measured using the phase difference of the fringes formed on the GB with respect to those formed on the RSS[10] as

$$F_j = \frac{[\phi_{\mathrm{RSS}} - \phi_{\mathrm{GB}}]_j}{2\pi}. \quad (3)$$

This provides the interference fringe pattern that is shifted in phase by the modulation system, the computer-controlled PZT, obtaining a series of phase-shifted fringe patterns expressed as

$$s_m(\mathbf{r},\phi,\alpha_m) = a_0(\mathbf{r}) + a_1(\mathbf{r})\cos[\phi(\mathbf{r})+\alpha_m], \quad (4)$$

where $a_0(\mathbf{r})$ is the average local irradiance value, $a_1(\mathbf{r})$ is the modulation amplitude which is proportional to the visibility, and α_m is the additional introduced phase shift. This optical phase $\phi(\mathbf{r})$ is retrieved by using phase shift algorithms[12] (PSAs) as

$$\phi(\mathbf{r}) = \arctan\left[\sum_{m=1}^{M} n_m s_m(\mathbf{r},\phi,\alpha_m) \Big/ \sum_{m=1}^{M} d_m s_m(\mathbf{r},\phi,\alpha_m)\right], \quad (5)$$

where n_m and d_m are the coefficients of the corresponding PSA. The main error source during this process is given by the lack of repeatability of the piezoelectric system.

The measurement of a mechanical comparator is combined with the exact fractions calculation method to provide the final result, which is then completed with corrections such as heat dilatation, obliquity, or phase shift of different materials between the GB and the RSS. Uncertainty estimation associated with the determination of the GB's length indicate that thermal expansion due to the temperature gradient between the GB and its setting makes a contribution of more than 63% in the uncertainty evaluation.[13] It is therefore necessary to control the environmental parameters during the process of measurement. In this way, the GB's length is corrected from the measured temperature to the reference temperature of 20ºC, according to its coefficient of linear thermal expansion, and taking into account possible phase shifts and obliquity errors.[1]

3 Interferometric System

The design implemented in this work is essentially a Twyman-Green interferometer (Fig. 1) at present, with a double He-Ne laser light source (632.8 and 543.2 nm) where the GB is illuminated vertically, according to the standard, and is wrung to the RSS. This surface and the ROS on the other arm of the interferometer are selected with good flatness and low wavefront distortion (Zerodur mirrors with $\lambda/20$ of flatness). Since our system provides

the optical and not the mechanical length, an error related to the different characteristics of the surfaces must be corrected. If two wavelengths are used, the length of the GB must be previously measured better than 1 μm. The collimation of the original beam is obtained with an achromatic doublet with a focal length of 500 mm, for a 2 in. optic, and with expansion possibilities. The light reflected from the ROS interferes with the light reflected from the GB and the RSS where the GB is wrung. For image acquisition, there is a choice of cameras: a 2M-XLI (CMOS-RGB) or a Thorlabs-DCC1545M (monochrome CMOS). Optomechanical modulation is carried out by a Physik Instrumente P-733.ZCL piezo nanopositioner with a displacement range of 100 μm and a nominal resolution of 0.3 nm. To adjust the fringe pattern (period and orientation), a fine adjustment is available. The control and evaluation system is made up of a main program written in C ++, which controls the different modules for positioning, acquisition, processing, and calculation of the optical phase (absolute/differential) in quasi-real-time using both conventional and custom designed PSAs/differential PSAs. The system also communicates with the atmospheric measuring equipment in order to include its readings in the calculation process. In the future, the modular design of the aforementioned program will allow us to insert or change its different components effortlessly.

There are two good reasons to control the environmental parameters around the GB and the interferometer. The first reason is to limit the temperature gradients between the block and its setting; the second reason is to monitor the air temperature, pressure, and relative humidity levels used to calculate the air refractive index. This requirement led us to encapsulate the measurement system in a thermostatic housing. Its structure is made up of modular aluminum profiles. Each wall is heat stabilized and is composed of a copper coil covered with insulation foam and sitting between two aluminum plates. This system was installed in the roof of the housing and in the four side walls, one of which is removable to access the inside of the interferometer. The housing is made up of an aluminum structure suitable for coupling to the mechanical base of the interferometer, which makes the assembly stable and secure. The walls are attached to this tubular aluminum structure by a custom designed system, and they act as heat exchangers between the copper coil and the inside the housing. In addition, we have installed a Julabo F25MC circulator with the nominal specification for PID controller stability. The required environmental values are monitored in real-time by a LabView® control program through an ASL 600 DC F600 thermometry bridge (uncertainty is higher than 10 ppm) and a Vaisala PTU3030 (uncertainties are higher than 0.1ºC in temperature, 1% in relative humidity, and 15 Pa in pressure). Readings are used for the indirect calculation of the refractive index of a specific wavelength according to Eq. (2). Figure 2 shows the evolution of the refractive index calculated over a period of 24 h. The measurement process was carried out in an environmentally controlled room at Laboratorio Oficial de Metroloxía de Galicia (LOMG) once the optical module was sealed and the additional temperature stabilization was allowed. To validate the implementation of our own software design, the results were compared with the reference results published by the NIST.[9] This comparison indicates a RMS deviation of 2.3 e-10, which is less than the ninth decimal of the refractive index. These values are compatible, bearing in mind that the uncertainty of the air refractive index and the experimental results exceed the eighth digit.

The calibration procedure consists of an acquisition of $M+N$ shifted patterns with known phase increments. A nominal control shift δ is introduced between the first M patterns, Eq. (4), and the δ-shifted N patterns (Fig. 3), such that

$$s_{M+m}(\mathbf{r},\phi,\alpha_{M+m}) = a_0(\mathbf{r}) + a_1(\mathbf{r})\cos[\phi(\mathbf{r}) + \delta_{\mathrm{PZT}} + \alpha_{M+m}]. \tag{6}$$

This process is repeated for consecutive increments of δ_{PZT}, and the phase difference between both patterns is recalculated, δ_{DPSA}, in each case with a DPSA[6–8] so that

$$\tan[(\phi+\delta_{\mathrm{DPSA}})-\phi] = \tan[\delta_{\mathrm{DPSA}}] = \frac{\sum_{m=1}^{M} d_m s_m(\mathbf{r},\phi,\alpha_m)\sum_{m=1}^{N} n_m s_{M+m}(\mathbf{r},\phi+\delta_{\mathrm{PZT}},\alpha_{M+m}) - \sum_{m=1}^{M} n_m s_m(\mathbf{r},\phi,\alpha_m)\sum_{m=1}^{N} d_m s_{M+m}(\mathbf{r},\phi+\delta_{\mathrm{PZT}},\alpha_{M+m})}{\sum_{m=1}^{M} n_m s_m(\mathbf{r},\phi,\alpha_m)\sum_{m=1}^{M} d_m s_m(\mathbf{r},\phi,\alpha_m) + \sum_{m=1}^{N} n_m s_{M+m}(\mathbf{r},\phi+\delta_{\mathrm{PZT}},\alpha_m)\sum_{m=1}^{N} d_m s_{M+m}(\mathbf{r},\phi+\delta_{\mathrm{PZT}},\alpha_{M+m})}. \tag{7}$$

The shift δ_{DPSA} is affected by the various systematic and random errors of the DPSAs. A histogram of the whole field image is obtained for each value with its average value and its typical deviation. Thus, a calibration line can be constructed with the values of δ_{PZT} and δ_{DPSA}. For example, Fig. 3 shows the line calibration drawn making use of Schwider-Hariharan[14,15] DPSA. The well-known compensatory capacities of this algorithm justify the regression coefficient R, one with a nearly 99% significance level. A test statistic for the F-test on the regression model provides a value of 6,881.666. Therefore, a significant linear regression relationship between the variables is provided. Finally, the p-value for the F-statistic of the linear relationship is equal to zero.

4 External Cavity Diode Laser Stabilization Using a Laser Mode Locking Technique

External cavity diode lasers (ECDL) can be used as an alternative to He-Ne gas lasers in dimensional metrology. These lasers take advantage of efficient, low-cost diode lasers and use frequency selective feedback to achieve narrow line width and tunability. Typically, the feedback is obtained through a diffraction grating in the Littrow configuration, and the narrow line width is achieved by a mode-locking technique using a reference gas cell, such as what is currently

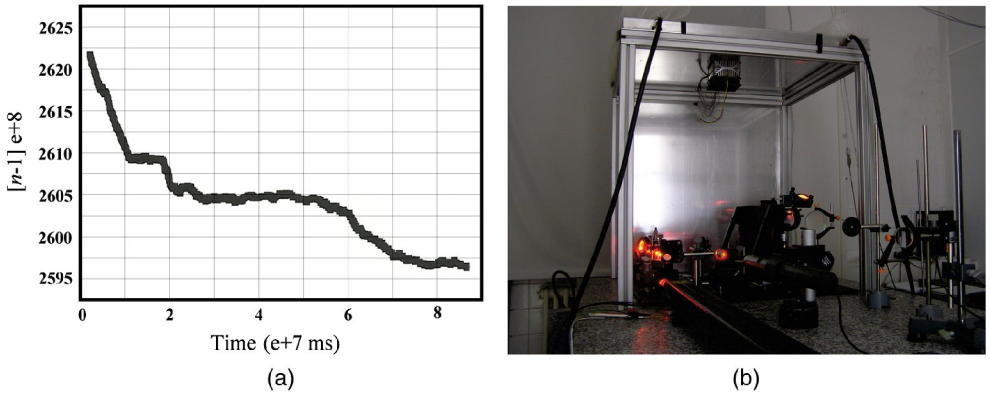

Fig. 2 Refractive index calculation stability (a) and real view of the experimental setup (b).

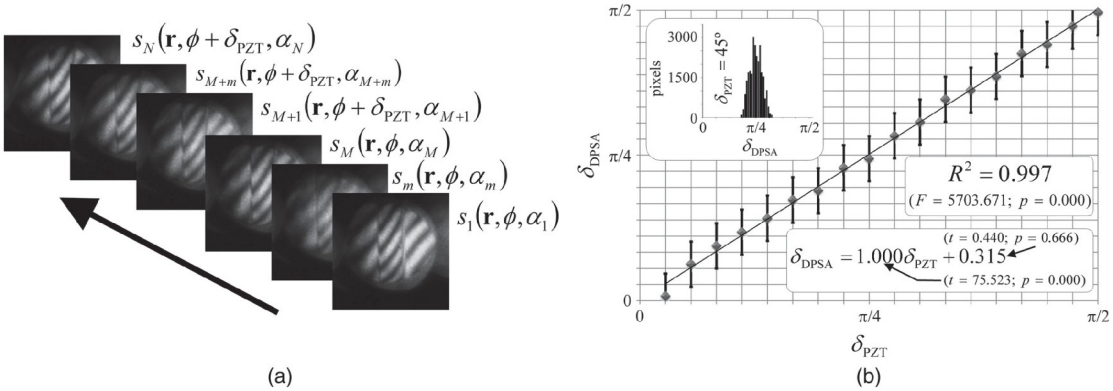

Fig. 3 $M+N$ phase-shifted patterns (a) and an example of the calibration line for δ values in the interval $[0,\pi/2]$ (b).

used in fundamental physics labs to cool atoms using magneto-optical traps.[16–18]

The experimental setup is shown in Fig. 4, and the laser beam is split in two probe beams and a saturating beam. The first two beams are shifted in the same direction and are received by the photodetectors, whereas the third one is shifted in the opposite direction to cross one of the others. This third beam, which is much more powerful than the others, is used to attain the saturation of the cell, avoiding the laser Doppler effect, which limits the line width to 1 ppm of the desired frequency. Frequency variations of the laser are turned into amplitude variations on the photodetector, due to the selective absorption of the gas cell. This electronic signal is controlled by the Moglabs DLC-202 electronics system, which drives a grating assembled on a piezoelectric actuator. Depending on the intensity differences detected by the photodetector, the controller can change the grating angle, which tunes the frequency of the probe beam. With this procedure, the bandwidth of the laser diodes can be reduced[19–21] to less than 1 MHz.

The line width is sensitive to the variations of the cavity length, laser diode temperature and current, feedback and gratting efficiency, and optical system alignment. Therefore, to avoid mechanical vibrations and temperature gradients and to keep the laser resonant cavity at a constant temperature, an encapsulated mechanical system was designed.

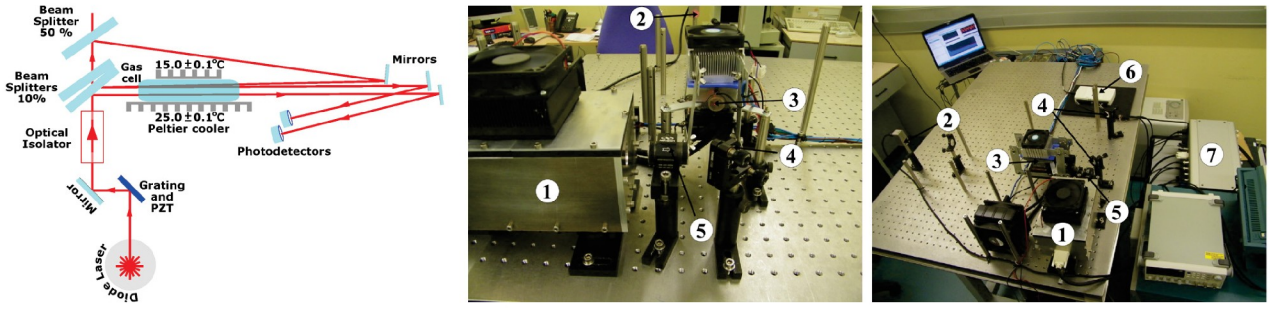

Fig. 4 Optical diagram and photography of the experimental setup: ECDL (1), photodetectors (2), iodine cell (3), beam splitters (4), optical isolator (5), DAQ (6), electronic controller (7).

This system was temperate and isolated, and it allowed the grating assembly, the mirror reflector, and the piezoelectric actuator to be integrated in the same module. This design reduces the mode spacing of the external cavity, while the cavity length can be tuned facing the laser mode hop.[22–24] The mechanical device depicted in Fig. 5 consists of a red laser diode at 635 nm (HL6344G) coupled to a collimator tube (Thorlabs LT230P-B), which incorporates a mounted aspheric lens (Thorlabs A230TM-A, $f = 4.51$ mm NA $=$ 0.54, 350 to 700 nm). These elements are mounted to a piece of aluminum connected to a Peltier cell (Global Componet Sourcing ET-131-10-13-S-RS, 36W 4A), and the temperature is measured by a temperature sensor (Texas Instruments AD592). In addition, there is a piece of stainless steel supporting the grating (Thorlabs GR25-1850, 18,00 l/mm), the mirror, and two piezoelectric actuators. This mirror is parallel to the diffraction grating and produces a fixed output beam regardless of the changes in the cavity length and grating angle.[19] The two different piezoelectric actuators, a stack (Noliac CMAP04) and a disc (Steminc SMD20T08F2500R), are responsible for changing the cavity length and seeking a better frequency response function in the control feedback. Moreover, three high-precision adjustment screws (Newport AJS100) are used to align the grating with the laser diode to achieve a fine alignment of the first diffraction order. Finally, the whole ECDL system is mounted to a thick invar 36 plate to provide inertial and thermal damping, and it is isolated from the environment through an aluminum box.

Furthermore, to assure good stability in the reference frequency given by the iodine cell, temperature stabilizing was performed on it. A thermal conditioning system was developed based on four Peltier cells (Melchor CP1.4-127-045-RTV), two SuperCool PR-59 controllers, and two fans (Coisar H80 and Fisher SK100-75-SA), as depicted in Fig. 6. To guarantee the accuracy of this thermal stabilization system, the NTC temperature sensors of the PID controllers (SuperCool PR-59) were calibrated by LOMG with deviations and uncertainties lower than 0.1°C. This system allows the cell to be stabilized with better parameters than the required specifications of 25.0 ± 5°C for the cell and 15.0 ± 0.2°C for the cold finger,[19,25] as shown in Fig. 7, over a period of 6 h.

This ECDL experimental setup was tested on the laser fluorescence phenomenon (as shown in Fig. 6), which is triggered by de-excitation of the iodine after having been excited by the laser at its absorption line. Figure 8 presents several absorption lines around 632.9 nm [R(127) 11-5 a16 transition],[19,25] detected by the photodetector when a triangular voltage sweep of the cavity was made by the stack piezoelectric. For this sweep, an interval between two peaks is shown in these figures to assess the quality of the system. Figure 8(b) shows the laser mode hops, which disguise the absorption lines, using the previous ECDL version without the mechanical system. However, Fig. 8(c) depicts the absorption lines achieved with the ECDL presented in this work. The downward dashed arrows mark two iodine transitions, labelled as a_n, because it was not possible to measure the absorption lines, since low-resolution equipment does not allow the spectral lines to be evaluated with the required precision. However, this equipment can measure the line width of the absorption lines, whereas the laser is stabilized. Also, Fig. 8(d) shows the error in the frequency measured during a mode-locking frequency technique using Fourier transform analysis. The diode frequency remained stable for a period of 5 h with a line width of 0.2 ppm. Therefore, this technique is suitable for adapting laser diodes as a reference frequency in metrological applications. The next step will enhance the stability of the ECDL, adjust the cavity parameters to avoid doing new alignments when a diode is changed, and measure the wavelength of the laser to know the accurate iodine transition fixed by the laser.

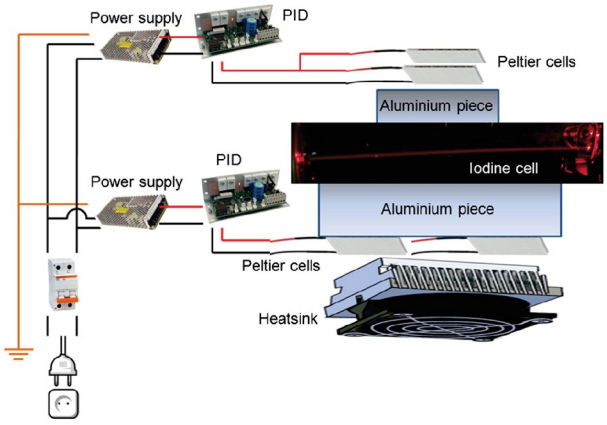

Fig. 6 Scheme of the temperature controller for the iodine cell.

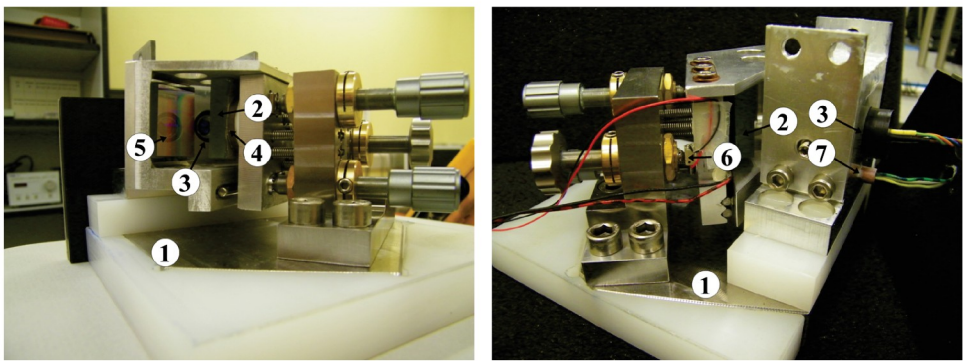

Fig. 5 Mechanical system of the external cavity diode laser (ECDL): Invar plate (1), grating (2), laser diode (3), PZT disc (4), mirror (5), PZT stack (6), temperature sensor (7).

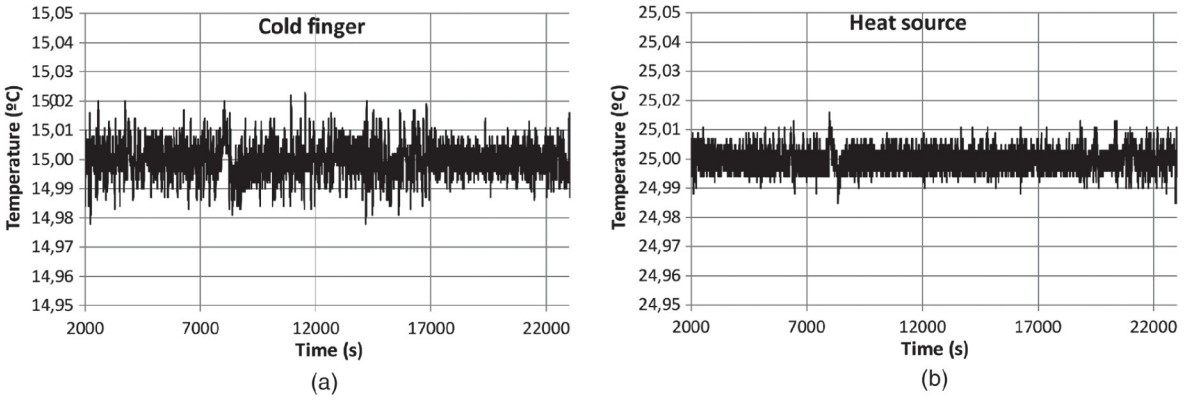

Fig. 7 Temperature stabilization of the iodine cell: (a) cold finger and (b) heat source.

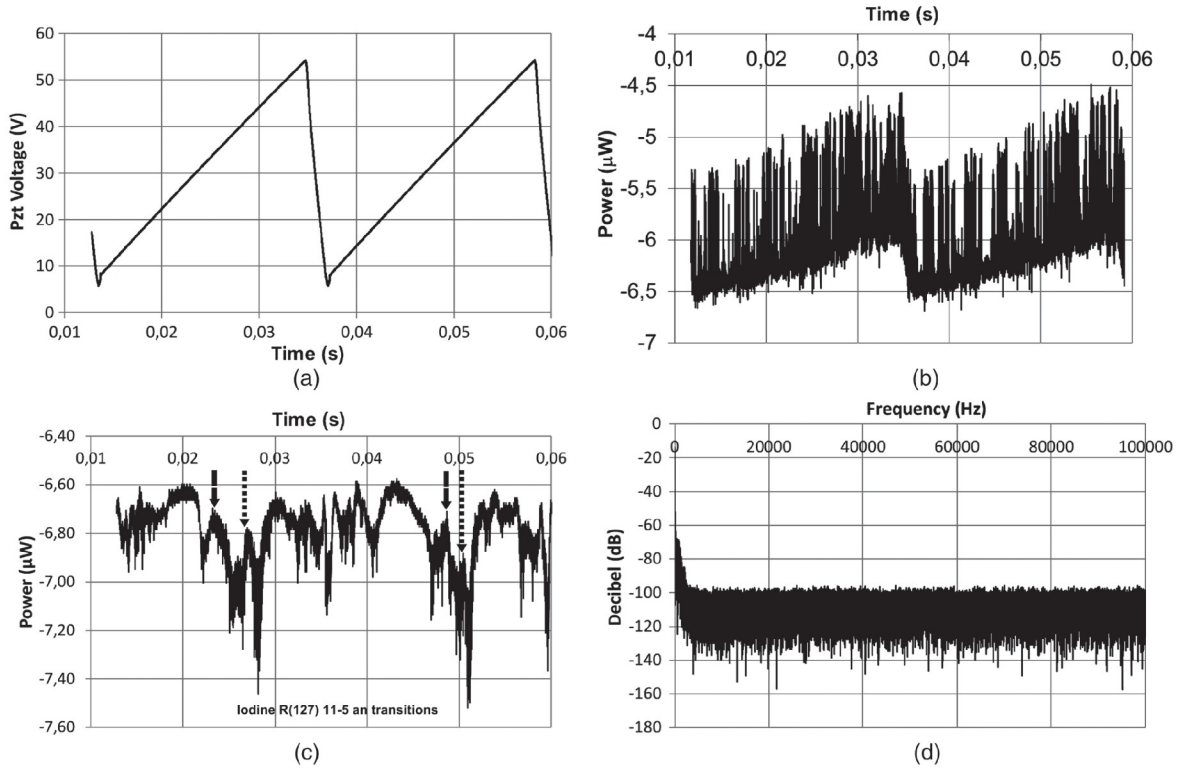

Fig. 8 (a) Triangular voltage sweep of the resonant cavity, (b) mode hops of the previous ECDL setup, (c) iodine absorption lines detected by the ECDL presented in this work and marked by the downward dashed arrows, and (d) frequency spectrum of the stabilized laser diode.

5 Summary and Conclusions

This work shows several aspects of the process of designing, constructing, and calibrating of a new multiple-wavelength Twyman-Green interferometer for the calibration of GBs. This interferometer has a custom developed automatic evaluation system based on optomechanical modulation, and the refractive index of the air was calculated using Edlén's equation to obtain the final length value. The main features of the interferometer are described, including the phase-shifting and image acquisition system. A procedure for the calibration is developed, and the experiments are carried out to stabilize a diode laser as a light source. We are planning to design a complete control loop that involves hardware and software developments to achieve the maximum performance of the stabilization process using low-cost components. The aim is to attain an automated GB dimensional measurement system employing robust and cheap laser diodes as light sources. The results obtained by calculating the refractive index of air and the optomechanical modulator show a high level of theoretical-experimental correlation.

Acknowledgments

The authors are grateful to the Spanish Ministry for Education and Science for funding the DPI2008-06818-C2-01 & 02/DPI Project.

References

1. J. E. Decker and J. R. Pekelsky, "Uncertainty evaluation for the measurement of gauge blocks by optical interferometry," *Metrologia* **34**(6), 479–493 (1997).
2. B. Edlén, "The refractive index of air," *Metrologia* **2**(2), 71–80 (1966).
3. K. P. Birch and M. J. Downs, "An updated Edlén equation for the refractive index of air," *Metrologia* **30**(3), 155–162 (1993).
4. K. P. Birch and M. J. Downs, "Correction to the updated Edlén equation for the refractive index of air," *Metrologia* **31**(4), 315–316 (1994).
5. J. E. Decker, R. Schödel, and G. Bönsch, "Considerations for the evaluation of measurement uncertainty in interferometric gauge block calibration applying methods of phase step interferometry," *Metrologia* **41**(3), L11–L17 (2004).
6. M. Miranda and B. V. Dorrío, "Fourier analysis of two-stage phase-shifting algorithms," *J. Opt. Soc. Am. A* **27**(2), 276–285 (2010).
7. M. Miranda and B. V. Dorrío, "Monte Carlo based techniques of two-stage phase shifting algorithms," *Opt. Lasers Eng.* **49**(3), 439–444 (2011).
8. M. Miranda et al., "Characteristic polynomial theory of two-stage phase shifting algorithms," *Opt. Lasers Eng.* **50**(4), 522–528 (2012).
9. J. A. Stone and J. H. Zimmerman, "Index of refraction of air," NIST 28, December 2011, http://emtoolbox.nist.gov/Wavelength/Edlen.asp (10 January 2013).
10. M. Born and E. Wolf, *Principles of Optics*, p. 291, Pergamon Press Ltd., Cambridge (1980).
11. P. E. Ciddor, "Refractive index of air: 3. The roles of CO_2, H_2O, and refractivity virials," *Appl. Opt.* **41**(12), 2292–2298 (2002).
12. B. V. Dorrío and J. L. Fernández, "Phase-evaluation methods in whole-field optical measurement techniques," *Meas. Sci. Tech.* **10**(3), 33–35 (1999).
13. V. Álvarez-Valado et al., "Testing phase-shifting algorithms for uncertainty evaluation in interferometric gauge block calibration," *Metrologia* **46**(6), 637–645 (2009).
14. J. Schwider et al., "Digital wave-front measuring interferometry: some systematic error sources," *Appl. Opt.* **22**(22), 3421–3432 (1983).
15. P. Hariharan, B. F. Oreb, and T. Eiju, "Digital phase-shifting interferometry: a simple error-compensating phase calculation algorithm," *Appl. Opt.* **26**(13), 2504–2506 (1987).
16. K. B. McAdam, A. Steibach, and C. Wieman, "A narrow-band tunable laser diode system with gratting feedback, and saturated absortion spectrometer for Cs and Rb," *Am. J. Phys.* **60**(12), 1098–1111 (1992).
17. M. C. Wieman and G. Flowers, "Inexpensive laser cooling and trapping experiment for undergraduate laboratories," *Am. J. Phys.* **63**(4), 317–330 (1995).
18. "Research groups working with atom traps," University of Innsbruck, 31, March 2007, http://www.uibk.ac.at/exphys/ultracold/atomtraps.html (10 January 2013).
19. H. Talvitie, M. Merimaa, and E. Ikonen, "Frequency stabilization of a diode laser to Doppler-free spectrum of molecular iodine at 633 nm," *Opt. Commun.* **152**(1–3), 182–188 (1998).
20. C. J. Hawthorn, K. P. Weber, and R. E. Scholten, "Littrow configuration tunable external cavity diode laser with fixed direction output beam," *Rev. Sci. Instrum.* **72**(12), 4477–4479 (2001).
21. R. W. P. Drever, "Laser phase and frequency stabilization using an optical resonator," *Appl. Phys. B: Lasers Opt.* **31**(2), 97–105 (1983).
22. C. Ye, *Tunable External Cavity Diode Lasers*, World Scientific, Texas A & M University (2004).
23. J. M. W. Kruger, "A novel technique for frequency stabilizing laser diodes," Postgraduate Diploma in Science, University of Otago (1998).
24. S. D. Saliba et al., "Mode stability of external cavity diode lasers," *Appl. Opt.* **48**(35), 6692–6700 (2009).
25. T. J. Quinn, "Practical realization of the definition of the metre, including recommended radiations of other optical frequency standards," *Metrologia* **40**(2), 103–133 (2003).

Javier Diz-Bugarín graduated as a telecommunications engineer from the University of Vigo, Spain, in 1994. He has worked as a fellow in the Applied Physics Department in several projects related to optical metrology, and he is currently working on a PhD in gauge block calibration. He also has experience in electronics R&D. He is also working as a teacher of electronics, and he has written several papers about electronics design and renewable energies.

Benito V. Dorrío received his BSc degree in physics in 1990 from the University of Santiago de Compostela, Spain, and his PhD in physics in 1996 from the University of Vigo, Spain. Since 1998, he has held a permanent research position as an assistant professor at the University of Vigo. He has coauthored more than 50 international scientific publications. His research interests include fringe analysis, interferometry, and phase evaluation methods.

Jesús Blanco-García received his doctoral degree in physics in 1992, with a thesis on holographic interferometry, from the University of Santiago de Compostela, Spain. He currently teaches physics at the University of Vigo, Spain. His main research subjects are holographic interferometry, moiré methods, ESPI, interferometer fringe analysis, and physics education.

Marta Miranda obtained her BSc in physics (optoelectronics) from the University of Santiago de Compostela, Spain, in 2003. Then she joined the Applied Physics Department at the University of Vigo, Spain, to work on the analysis of differential phase shifting algorithms to get her PhD in 2010. Nowadays, she is developing new tools to analyze the behavior of phase evaluation algorithms for optical metrology.

Ismael Outumuro graduated in 2006 with a degree in physics from the University of Vigo, Spain. Soon afterward, he joined the Metrology Laboratory of Galicia, Spain, where is currently working in dimensional metrology, in particular laser interferometry and coordinate measurement machines. He is enrolled in a PhD program in laser applications in metrology.

Jose Luis Valencia is a researcher at the Metrology Laboratory of Galicia, Spain. He earned his MSc in 2000 and his PhD in 2005 in physics from the University of Vigo, Spain. He has worked at the National Physical Laboratory, UK, as a guest researcher from 2008 to 2010 in the area of dimensional nanometrology. His current areas of interest are atomic force microscopy and laser interferometry.

CAPÍTULO 3. ESTUDIO DE ALGORITMOS DIFERENCIALES DE DESPLAZAMIENTO DE FASE PARA MEDIDAS DE BPL

3.1. CHARACTERISTIC POLYNOMIAL THEORY OF TWO-STAGE PHASE SHIFTING ALGORITHMS

RESUMEN

Los algoritmos de desplazamiento de fase de dos etapas permiten recuperar directamente la suma o la diferencia de la fase óptica de dos patrones de franjas diferentes. Estos algoritmos se pueden construir combinando algoritmos de desplazamiento de fase conocidos de forma no lineal. En este trabajo, asociamos un polinomio característico bidimensional a cada algoritmo de desplazamiento de fase de dos etapas. Esto nos permite comparar cualitativamente su comportamiento frente a las principales fuentes sistemáticas de error, mediante un protocolo de análisis como el que se utiliza para los algoritmos de desplazamiento de fase. Demostramos que esta herramienta permite comprender la propagación de las propiedades de los algoritmos de desplazamiento de fase precursores a los nuevos algoritmos de evaluación obtenidos a partir de ellos. Como aplicación experimental, se presenta una evaluación de distorsión de frente de onda en interferometría.

PALABRAS CLAVE

Phase retrieval, Phase shifting Interferometry, Wavefront distortion, Two-stage.

PUBLICACIÓN ORIGINAL

M. Miranda, B.V. Dorrio, J. Blanco, J. Diz-Bugarin, F. Ribas, "*Characteristic polynomial theory of two-stage phase shifting algorithms*", Optics and Lasers in Engineering, Vol. 50, Issue 4, April 2012, Pages 522-528, ISSN 0143-8166. https://doi.org/10.1016/j.optlaseng.2011.09.002

Optics and Lasers in Engineering 50 (2012) 522–528

Contents lists available at SciVerse ScienceDirect

Optics and Lasers in Engineering

journal homepage: www.elsevier.com/locate/optlaseng

Characteristic polynomial theory of two-stage phase shifting algorithms

M. Miranda *, B.V. Dorrío, J. Blanco, J. Diz-Bugarín, F. Ribas

Applied Physics Department, University of Vigo, Campus Universitario, 36310 Vigo, Spain

ARTICLE INFO

Available online 4 October 2011

Keywords:
Phase retrieval
Phase shifting
Interferometry
Wavefront distortion
Two-stage

ABSTRACT

Two-stage phase shifting algorithms make possible to directly recover the sum or the difference of the optical phase of two different fringe patterns. These algorithms can be built by combining the known phase shifting algorithms in a non-linear way. In this work, we associate a two-dimensional characteristic polynomial to each two-stage phase shifting algorithm. This enables us to qualitatively compare their behaviour against the main systematic error sources, by means of an analysis protocol like that used for phase shifting algorithms. We show that this tool allows to understand the propagation of properties from precursor phase shifting algorithms to new evaluation algorithms built from them. As an experimental application, a wavefront distortion evaluation in differential phase-shifting interferometry is presented.

1. Introduction

A great variety of metrological applications [1] require the use of phase shifting interferometry [2]. In it, M irradiance values equally shifted in phase [3], $\alpha_m=2\pi(m-1)/M$, and with k-harmonic components a_k

$$s_m(\mathbf{r},\phi,\alpha_m)=\sum_{k=0}^{\infty}a_k(\mathbf{r})\cos[k(\phi+\alpha_m)] \tag{1}$$

are linearly combined in the argument of an arctan function [4] to recover the phase of the pattern

$$\phi(\mathbf{r})=\arctan\frac{\sum_{m=1}^{M}n_m s_m(\mathbf{r},\phi,\alpha_m)}{\sum_{m=1}^{M}d_m s_m(\mathbf{r},\phi,\alpha_m)}=\arctan\frac{\sum_{m=1}^{M}h_N(u_{1m})s_m(\mathbf{r},\phi,\alpha_m)}{\sum_{m=1}^{M}h_D(u_{1m})s_m(\mathbf{r},\phi,\alpha_m)} \tag{2}$$

where (n_m,d_m) are the sampling amplitudes that define each phase shifting algorithm (PSA). This process can also be expressed as a discretization of the irradiance signal $s(\mathbf{r},\phi)$ with sampling functions $h_{N,D}(u_1)$ [5,6] – where u_1 is the spatial or temporal variable – at each sampling point $u_1=u_{1m}$, where $\alpha_m=2\pi f_s u_{1m}$ with f_s its reference frequency. The Fourier transform (FT) of these sampling functions are called characteristic spectra (CS), $H_{N,D}(f_1)=\mathrm{FT}[h_{N,D}(u_1)]$, and their amplitudes provide a qualitative vision of the main errors sources of the PSAs. But this frequency analysis, carried out independently with the two sampling functions, can lead to proportional spectral representations of each rotation of the same PSA with identical compensatory properties and with a difference, in general, connected to a constant phase term that is irrelevant in many situations. This non-evident similarity between shifted PSAs can be sidestepped [7–12] using a more complete analysis considering the combined CS of the PSA defined as

$$H=H_D(f_1)+jH_N(f_1) \tag{3}$$

An alternative, and equivalent, analysis of sensitivities is obtained relating the calculation of the optical phase of a PSA to an associated complex number $V(\phi)$. So Eq. (2) can be rewritten as

$$V(\phi)=\sum_{m=1}^{M}(d_m+jn_m)s_m(\mathbf{r},\phi,u_m)=\sum_{k=-\infty}^{\infty}\left[a_k e^{jk\phi}\sum_{m=1}^{M}(d_m+jn_m)e^{jk\alpha(m-1)}\right]=\sum_{k=-\infty}^{\infty}[a_k e^{jk\phi}P(e^{jk\alpha})] \tag{4}$$

with additional phase $\alpha=\alpha_{m+1}-\alpha_m=\alpha_m/(m-1)$ being $P[\exp(jk\alpha)]$ the characteristic polynomial (CP) of the PSA. The multiplicity and localisation of the roots of the CP inform about the main systematic error sources in PSAs, such as the presence of undesired harmonics in the recovered signal or phase shift errors. So, if we consider the k-coefficients a_k with $k>1$ non zero and the additional phase disturbed in the form

$${}^{E}\alpha_m=\alpha_m+E\alpha_m=\alpha_m+\sum_{q=1}^{\infty}\varepsilon_q\frac{\alpha_m^q}{q\pi^{q-1}} \tag{5}$$

with the error $E\alpha_m$ quantified by the q-th term ε_q, we can express the Eq. (1) affected by both errors:

$$s_m(\mathbf{r},\phi,{}^{E}\alpha_m)=\sum_{k=0}^{\infty}a_k(\mathbf{r})\cos[k(\phi+{}^{E}\alpha_m)]=\sum_{k=-\infty}^{\infty}\frac{a_k(\mathbf{r})}{2}e^{jk(\phi+{}^{E}\alpha_m)} \tag{6}$$

Thus [13–18], for instance, elimination of local average irradiance effects for the fringe pattern requires the cancelling of the CP at $k=0$, while the insensitivity to an undesired k-harmonic ($k>1$) demands that $P[\exp(jk\alpha)]$ was cancelled at this frequency, which, in

* Corresponding author.
E-mail address: marta_miranda@uvigo.es (M. Miranda).

0143-8166/$ - see front matter © 2011 Elsevier Ltd. All rights reserved.
doi:10.1016/j.optlaseng.2011.09.002

factorisation terms, means that $\exp(jk\alpha)$ and $\exp(-jk\alpha)$ must be roots of the CP. Regarding phase detuning errors (first order errors in the phase step), the double root of $\exp(-j\alpha)$ must appear, and not that for $\exp(j\alpha)$ since the fundamental harmonic must be detected.

$$[\phi(\mathbf{r})+\Delta\phi(\mathbf{r})]\pm\phi(\mathbf{r})=\arctan\frac{\sum_{m=1}^{M}d_m s_m(\mathbf{r},\phi,\alpha_m)\sum_{p=1}^{P}n_p t_p(\mathbf{r},\phi+\Delta\phi,\beta_p)\pm\sum_{m=1}^{M}n_m s_m(\mathbf{r},\phi,\alpha_m)\sum_{p=1}^{P}d_p t_p(\mathbf{r},\phi+\Delta\phi,\beta_p)}{\mp\sum_{m=1}^{M}n_m s_m(\mathbf{r},\phi,\alpha_m)\sum_{p=1}^{P}n_p t_p(\mathbf{r},\phi+\Delta\phi,\beta_p)+\sum_{m=1}^{M}d_m s_m(\mathbf{r},\phi,\alpha_m)\sum_{p=1}^{P}d_p t_p(\mathbf{r},\phi+\Delta\phi,\beta_p)} \tag{13}$$

In any case, the analysis with the combined CS and the CP are directly related [18] and both of them obtain coinciding results so

$$\begin{aligned}P(e^{jk\alpha})&=\sum_{m=1}^{M}(d_m+jn_m)e^{(m-1)jk\alpha}=\sum_{m=1}^{M}d_m e^{j\alpha_m\frac{f_1}{f_s}}+j\sum_{m=1}^{M}n_m e^{j\alpha_m\frac{f_1}{f_s}}\\&=H_D(-f_1)+jH_N(-f_1)\end{aligned} \tag{7}$$

But it can also be the case that the information of the measurand [19–27] was function of the sum or the difference of the optical phase between an original fringe pattern $s(\mathbf{r},\phi)$ and another modified one $t(\mathbf{r},\phi+\Delta\phi)$ with irradiance values weighted with g-coefficients b_g:

$$t_p(\mathbf{r},\phi+\Delta\phi,\beta_p)=\sum_{g=0}^{\infty}b_g(\mathbf{r})\cos[g(\phi+\Delta\phi+\beta_p)] \tag{8}$$

Likewise, the phase $\phi(\mathbf{r})+\Delta\phi(\mathbf{r})$ is also obtained by the linear combination of P irradiance values

$$\begin{aligned}\phi(\mathbf{r})+\Delta\phi(\mathbf{r})&=\arctan\frac{\sum_{p=1}^{P}n_p t_p(\mathbf{r},\phi+\Delta\phi,\beta_p)}{\sum_{p=1}^{P}d_p t_p(\mathbf{r},\phi+\Delta\phi,\beta_p)}\\&=\arctan\frac{\sum_{p=1}^{P}h_N(u_{2p})t_p(\mathbf{r},\phi+\Delta\phi,\beta_p)}{\sum_{p=1}^{P}h_D(u_{2p})t_p(\mathbf{r},\phi+\Delta\phi,\beta_p)}\end{aligned} \tag{9}$$

with (n_p,d_p) the sampling amplitudes at the point analysed $u_2=u_{2p}$ as $\beta_p=2\pi f_t u_{2p}$ where f_t is its reference frequency and the sampling functions are related with the CS of the modified pattern as $H_{N,D}(f_2)=\mathrm{FT}[h_{N,D}(u_2)]$. We can associate the phase of the pattern with the phase of the complex function $V(\phi+\Delta\phi)$. So, the sensitivity of the modified pattern can also be given by the behaviour of its CP $P[\exp(jg\beta)]$

$$\begin{aligned}\mathrm{V}(\phi+\Delta\phi)&=\sum_{p=1}^{P}(d_p+jn_p)t_p(\mathbf{r},\phi+\Delta\phi,u_p)\\&=\sum_{g=-\infty}^{\infty}\left[b_g e^{jg(\phi+\Delta\phi)}\sum_{p=1}^{P}(d_p+jn_p)e^{jg\beta(p-1)}\right]\\&=\sum_{g=-\infty}^{\infty}[b_g e^{jg(\phi+\Delta\phi)}P(e^{jg\beta})]\end{aligned} \tag{10}$$

where $\beta=\beta_{p+1}-\beta_p=\beta_p/(p-1)$. We can also assume the presence of g undesired harmonics b_g and errors in the phase shifter in the form

$${}^{E}\beta_p=\beta_p+E\beta_p=\beta_p+\sum_{r=1}^{\infty}\chi_r\frac{\beta_p^r}{r\pi^{r-1}} \tag{11}$$

quantifying X_r the magnitude of r-th order. So the modified pattern, Eq. (8), is disturbed in the form

$$\begin{aligned}t_p(\mathbf{r},\phi+\Delta\phi,{}^{E}\beta_p)&=\sum_{g=0}^{\infty}b_g(\mathbf{r})\cos[g(\phi+\Delta\phi+{}^{E}\beta_p)]\\&=\sum_{g=-\infty}^{\infty}\frac{b_g(\mathbf{r})}{2}e^{jg(\phi+\Delta\phi+{}^{E}\beta_p)}\end{aligned} \tag{12}$$

Thus, the last step to recover the additive phase or the difference phase between the original and the modified patterns would be to add or subtract, respectively, the unwrapped phases [28] obtained with Eqs. (2) and (9). If a characterisation procedure was required the calculation of the combined CS and/or the CP of each pattern would also be necessary. All this laborious process can be simplified if two-stage phase shifting algorithms (TSPSAs) [29–36] are employed:

This two-dimensional analysis combine the numerator and the denominator of the precursor PSAs, Eqs. (2) and (9), to recover the phase sum $2\phi(\mathbf{r})+\Delta\phi(\mathbf{r})$ (upper sign) or the phase difference $\Delta\phi(\mathbf{r})$ (lower sign) in a unique calculation. Moreover, they can provide directly continuous values of the phase difference $\Delta\phi(\mathbf{r})$ when a period is not completed in the whole pattern area and thus avoid the unwrapping process. The advantages of the use of TSPSAs depend on the particular application. For example, in phase-shifted ESPI measurements [21] the subtraction in the fringe pattern domain, before the arctangent is applied, has the noticeable advantage of facilitating the application of smoothing routines to improve the contrast of the correlation fringes; or in multi-wavelength interferometry, the fringe pattern domain calculation reduces the sensitivity to random irradiance fluctuations and facilities its ability to measure diffuse, as well as reflective, surfaces [20]. In previous works [32–36], we have shown the good behaviour of TSPSAs by means of quantitative and qualitative analysis of their main associated errors. All these techniques supply the same information with the obvious difference between a quantitative and a qualitative research. Thus, the Taylor development [32] or the Monte Carlo method [33,36] obtain a curve of the error whereas the Fourier analysis [34] can only inform about the presence or absence of the error. The procedures are independent, the choice of either one depends on the capabilities of the researcher. Here, we aim to complete the qualitative characterisation of these algorithms using as a tool a two-dimensional characteristic polynomial (TDCP) that provides information about the main sensitivities of the TSPSAs and relates them with the sensitivities of their precursor PSAs.

2. Two-dimensional characteristic polynomial

The generic equation of a TSPSA, Eq. (13), can also be expressed as a quantification process [34]

$$\begin{aligned}&[\phi(\mathbf{r})+\Delta\phi(\mathbf{r})]\pm\phi(\mathbf{r})\\&=\arctan\frac{\sum_{m=1}^{M}\sum_{p=1}^{P}n_{m,p}s_m(\mathbf{r},\phi,\alpha_m)t_p(\mathbf{r},\phi+\Delta\phi,\beta_p)}{\sum_{m=1}^{M}\sum_{p=1}^{P}d_{m,p}s_m(\mathbf{r},\phi,\alpha_m)t_p(\mathbf{r},\phi+\Delta\phi,\beta_p)}\\&=\arctan\frac{\sum_{m=1}^{M}\sum_{p=1}^{P}h_N(u_{1m},u_{2p})s_m(\mathbf{r},\phi,\alpha_m)t_p(\mathbf{r},\phi+\Delta\phi,\beta_p)}{\sum_{m=1}^{M}\sum_{p=1}^{P}h_D(u_{1m},u_{2p})s_m(\mathbf{r},\phi,\alpha_m)t_p(\mathbf{r},\phi+\Delta\phi,\beta_p)}\end{aligned} \tag{14}$$

where $(n_{m,p},d_{m,p})$ are the sampling amplitudes of the auxiliary mathematical function $s(\mathbf{r},\phi)t(\mathbf{r},\phi+\Delta\phi)$, which are precisely the values that make good recovery of either the phase sum, when $n_{m,p}=\sin(\alpha_m+\beta_p)$ and $d_{m,p}=\cos(\alpha_m+\beta_p)$, or the phase difference, $n_{m,p}=\sin(\alpha_m-\beta_p)$ and $d_{m,p}=\cos(\alpha_m-\beta_p)$. Thus, the goodness of a TSPSA is also determined by its sensitivities to the main error sources that are given in the reciprocal space by their two-dimensional CS (TDCS) $H_{N,D}(f_1,f_2)=\mathrm{FT}[h_{N,D}(u_1,u_2)]$. A similar qualitative characterisation can be carried out by associating a complex number $V[(\phi+\Delta\phi)\pm\phi]$ to the calculation of the phase,

using Eq. (14)

$$V[(\phi+\Delta\phi)\pm\phi]=\sum_{m=1}^{M}\sum_{p=1}^{P}(d_{m,p}+jn_{m,p})s_m(\mathbf{r},\phi,\alpha_m)t_p(\mathbf{r},\phi+\Delta\phi,\beta_p)$$
$$=\sum_{k=-\infty}^{\infty}\sum_{g=-\infty}^{\infty}a_kb_ge^{j[g\Delta\phi+(g\pm k)\phi]}\sum_{m=1}^{M}\sum_{p=1}^{P}(d_{m,p}+jn_{m,p})e^{jk2\pi f_s u_m}e^{jg2\pi f_t u_p}$$
$$=\sum_{k=-\infty}^{\infty}\sum_{g=-\infty}^{\infty}a_kb_ge^{j[g\Delta\phi+(g\pm k)\phi]}\sum_{m=1}^{M}\sum_{p=1}^{P}(d_{m,p}+jn_{m,p})e^{jk\alpha(m-1)}e^{jg\beta(p-1)}$$
$$=\sum_{k=-\infty}^{\infty}\sum_{g=-\infty}^{\infty}a_kb_ge^{j[g\Delta\phi+(g\pm k)\phi]}P(e^{jk\alpha},e^{jg\beta}) \quad (15)$$

So, the analysis of the TDCP $P[\exp(jk\alpha),\exp(jg\beta)]$ provides information about the sensitivity of the TSPSA. So, if we consider the k-coefficients a_k of the original pattern and the g-coefficients b_g of the modified one, with $k,g>1$, non zero and the additional phases of the patterns disturbed in the form of Eqs. (5) and (11), the complex representation of the TDCP, Eq. (15), is altered as follows:

$$V\left[(\phi+\Delta\phi)\pm\phi\right]=\sum_{k=-\infty}^{\infty}\sum_{g=-\infty}^{\infty}\frac{a_kb_g}{4}e^{j[g\Delta\phi+(g+k)\phi]}P(e^{jk^E\alpha},e^{jg^E\beta})$$
$$=\sum_{k=-\infty}^{\infty}\sum_{g=-\infty}^{\infty}\frac{a_kb_g}{4}e^{j[g\Delta\phi+(g+k)\phi]}\left[P(e^{jk\alpha},e^{jg\beta})+\sum_{q=1}^{\infty}(jk\alpha e^{jk\alpha})^q\right.$$
$$\times\frac{\varepsilon_q\alpha^q}{q\pi^{q-1}}\frac{\partial^qP(e^{jk\alpha},e^{jg\beta})}{\partial(e^{jk\alpha})^q}+\sum_{r=1}^{\infty}(jg\beta e^{jg\beta})^r\frac{\chi_r\beta^r}{r\pi^{r-1}}\frac{\partial^rP(e^{jk\alpha},e^{jg\beta})}{\partial(e^{jg\beta})^r}$$
$$\left.+\sum_{q=1}^{\infty}\sum_{r=1}^{\infty}(jk\alpha e^{jk\alpha})^q(jg\beta e^{jg\beta})^r\frac{\varepsilon_q\alpha^q}{q\pi^{q-1}}\frac{\chi_r\beta^r}{r\pi^{r-1}}\frac{\partial^r}{\partial}\left(\frac{\partial^qP(e^{jk\alpha},e^{jg\beta})}{\partial(e^{jk\alpha})^q}\right)\right] \quad (16)$$

The localisation and multiplicity of the roots of the TDCP indicate the sensitivities of the TSPSA.

The non-sinusoidal function $s(\mathbf{r},\phi)t(\mathbf{r},\phi+\Delta\phi)$ should only detect the reference frequency, $(k,g)=(1,1)$ for the phase sum and $(k,g)=(-1,1)$ for the phase difference. An harmonic component a_kb_g does not interfere if the TDCP is null at (k,g) and at its conjugate $(-k,-g)$. If a harmonic with $k=0$ or $g=0$ is detected, the TSPSA is sensitive to local average irradiance. The last three summands in Eq. (16) must be null in order to avoid calibration errors. Thus, the lack of detuning errors ($q=1$ and $r=1$) demands that the harmonic (k,g) and its conjugate $(-k,-g)$ were double roots to cancel the first and also the second derivative of the summands. Obviously, in the case of the reference frequency only $\exp(-j\alpha)$ and $\exp(-j\beta)$ for the sum and $\exp(j\alpha)$ and $\exp(-j\beta)$ for the difference have to be double roots.

The calculation of the zeros of a TDCP can be considerably simplified by relating the two-dimensional sampling amplitudes $(n_{m,p},d_{m,p})$ with those for their PSA precursors, (n_m,d_m) and (n_p,d_p), according to Eqs. (4) and (10). Thus the additive TDCP can be expressed as the direct multiplication of the CP of the PSA precursors

$$P(e^{jk\alpha},e^{jg\beta})=\sum_{m=1}^{M}\sum_{p=1}^{P}(d_m+jn_m)(d_p+jn_p)e^{jk(m-1)\alpha}e^{jg(p-1)\beta}=P(e^{jk\alpha})P(e^{jg\beta}) \quad (17)$$

and the same for the differential TDCP but recovering $-\phi$ in the original pattern

$$P(e^{jk\alpha},e^{jg\beta})=\sum_{m=1}^{M}\sum_{p=1}^{P}(d_m-jn_m)(d_p+jn_p)e^{jk(m-1)\alpha}e^{jg(p-1)\beta}$$
$$=P^*(e^{-jk\alpha})P(e^{jg\beta}) \quad (18)$$

where * indicates complex conjugate. Thus, the propagation of the PSA precursor sensitivities to the TSPSAs is obtained in an obvious way according to Eqs. (17) and (18). The error associated to the additive/differential TSPSA coincides with the sum/difference of the error linked of its precursor PSAs. Moreover, this factorisation can be used as a design tool of PSAs, if $\Delta\phi(\mathbf{r})$ is null in the modified pattern, with probable improved properties with regards to their PSA precursors. So, the current state of knowledge of the sensitivities of a large number of PSAs is a valuable help to design both PSA and TSPSAs.

Finally, it is also possible to directly relate the TDCP with a combined TDCS that shows mathematically that the two are equivalent qualitative analysis

$$P(e^{jk\alpha},e^{jg\beta})=\sum_{m=1}^{M}(d_m\mp jn_m)e^{jk(m-1)\alpha}\sum_{p=1}^{P}(d_p+jn_p)e^{jg(p-1)\beta}$$
$$=\left(\sum_{m=1}^{M}d_me^{j\alpha_m\frac{f_1}{f_s}}\mp j\sum_{m=1}^{M}n_me^{j\alpha_m\frac{f_1}{f_s}}\right)$$
$$\times\left(\sum_{p=1}^{P}d_pe^{j\beta_p\frac{f_2}{f_t}}+j\sum_{p=1}^{P}n_pe^{j\beta_p\frac{f_2}{f_t}}\right)$$
$$=\left[H_D(-f_1)\mp jH_N(-f_1)\right]\left[H_D(-f_2)+jH_N(-f_2)\right]$$
$$=H(-f_1,-f_2) \quad (19)$$

3. Example of two-dimensional characteristic polynomial

To appreciate the importance of a good choice of the precursors PSAs we combine two of them with different sensitivities: the symmetrical 3+1 PSA for the original pattern and the symmetrical 4+1 PSA for the modified pattern [37] in order to study inherited behaviours. Figs. 1 and 2 show the module and polar diagram of the CP of each of them [6,13–18]. Both representations are equivalent: the module represents the magnitude of the coefficient a_k or b_g at each k-harmonic or g-harmonic and the polar diagram represents its value at each α_m or β_p angle. The latter shows in a more evident from the periodicity of the harmonic amplitudes, thus the symmetrical 3+1 PSA repeats its behaviour every three harmonics and the symmetrical 4+1 PSA every four harmonics. We can note that symmetrical 3+1 PSA is sensitive to small detuning error ($P[\exp(jk\alpha)]$ does not have a double root at $k=-1/\alpha_{-1}=4\pi/3$) and the second harmonic is the first detected (it is not null at $k=-2/\alpha_{-2}=2\pi/3$) while the symmetrical 4+1 PSA is insensitive to small detuning error ($P[\exp(jg\beta)]$ and its derivative function are null at $g=-1/\beta_{-1}=3\pi/2$) and the first detected harmonic is the third (at $g=-3/\beta_{-3}=\pi/2$ is not null). We build the additive (upper sign) and differential (lower sign) symmetrical 3+1–symmetrical 4+1

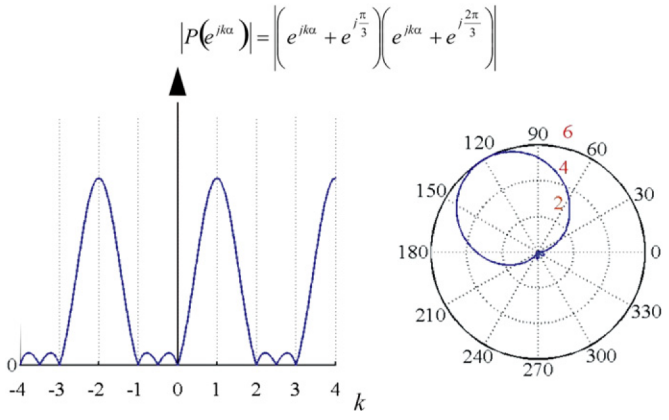

Fig. 1. Module (left) and diagram polar (right) of the CP for the symmetrical 3+1 PSA.

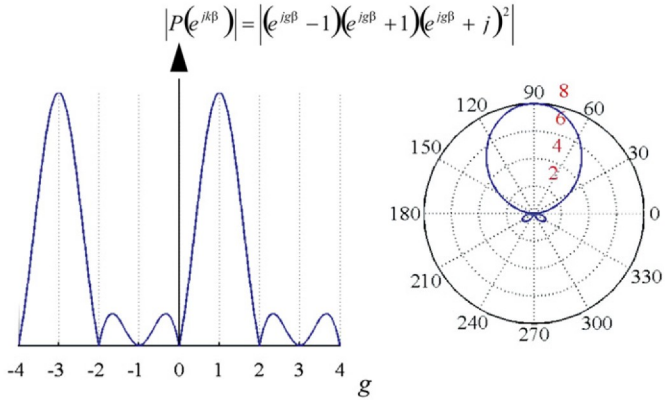

Fig. 2. Module (left) and diagram polar (right) of the CP for the symmetrical 4+1 PSA.

TSPSA with Eq. (13)

$$\text{Sim3+1–Sim4+1}[(\phi+\Delta\phi)\pm\phi] = \arctan\frac{2(s_1-s_2-s_3+s_4)(t_4-t_2)\pm\sqrt{3}(s_3-s_2)(t_1-2t_3+t_5)}{\mp 2\sqrt{3}(s_3-s_2)(t_4-t_2)+(s_1-s_2-s_3+s_4)(t_1-2t_3+t_5)} \quad (20)$$

Fig. 3 shows the additive TDCP, calculated according to Eq. (17), and Fig. 4 shows the differential TDCP, obtained according to Eq. (18), making use of their moduli and polar diagrams. The additive TDCP (Fig. 3) shows that the reference frequency $2\phi+\Delta\phi$ is effectively recovered as $(k,g)=(1,1)/(\alpha_1,\beta_1)=(2\pi/3,\pi/2)$ is not a root. The harmonics $(-2,1)$, $(-2,-3)$, $(1,-3)$, $(4,-3)$ and $(4,1)$ neither are null so the harmonics components with coefficients a_2b_1, a_2b_3, a_1b_3, a_4b_3 and a_4b_1 interfere with the signal. At $(k,g)=(-1,-1)$ $/(\alpha_{-1},\beta_{-1})=(4\pi/3,3\pi/2)$ the additive TDCP has not a double root so it is sensitive to detuning.

The differential TDCP (Fig. 4) has a similar representation to the additive TDCP except that it is $4\pi/3$ displaced in the direction of the original pattern. It detects the signal at $(k,g)=(-1,1)$ and unfortunately also at $(-4,-3)$, $(-4,1)$, $(-1,-3)$, $(-1,1)$, $(2,-3)$ and $(2,1)$. At $(k,g)=(1,-1)$ does not have a double root, which means it is also sensitive to detuning.

The additive symmetrical 3+1–symmetrical 4+1 TSPSA does not detect the second harmonic, $4\phi+2\Delta\phi$, and the differential one is not sensitive to $2\Delta\phi$, since in both of the cases $(-2,-2)$, $(-2,2)$, $(2,-2)$ and $(2,2)$ are null. However, other harmonic components with $k=2$, such as the coefficients a_2b_1 and a_2b_3, are detected. It is important to note that the functional dependency of harmonics with $k=1$ or $g=1$ can be obtained by means a linear approach but higher components require a non-linear approximation. In a previous work [32] we have linearised the systematic errors of this type of TSPSAs. Eq. (21) shows the sensitivity of the additive/differential symmetrical 3+1–symmetrical 4+1TSPSA to the presence of harmonics of first order, where only can be mathematically obtained the contribution of

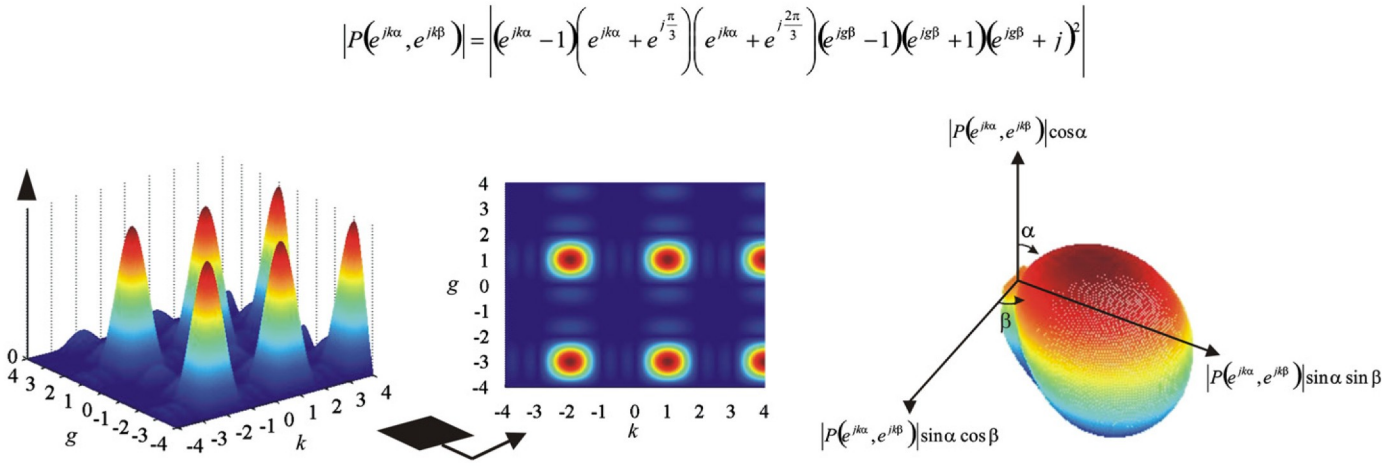

Fig. 3. Module with its plan view (left) and polar diagram (right) of the TDCP for the additive symmetrical 3+1–symmetrical 4+1 TSPSA.

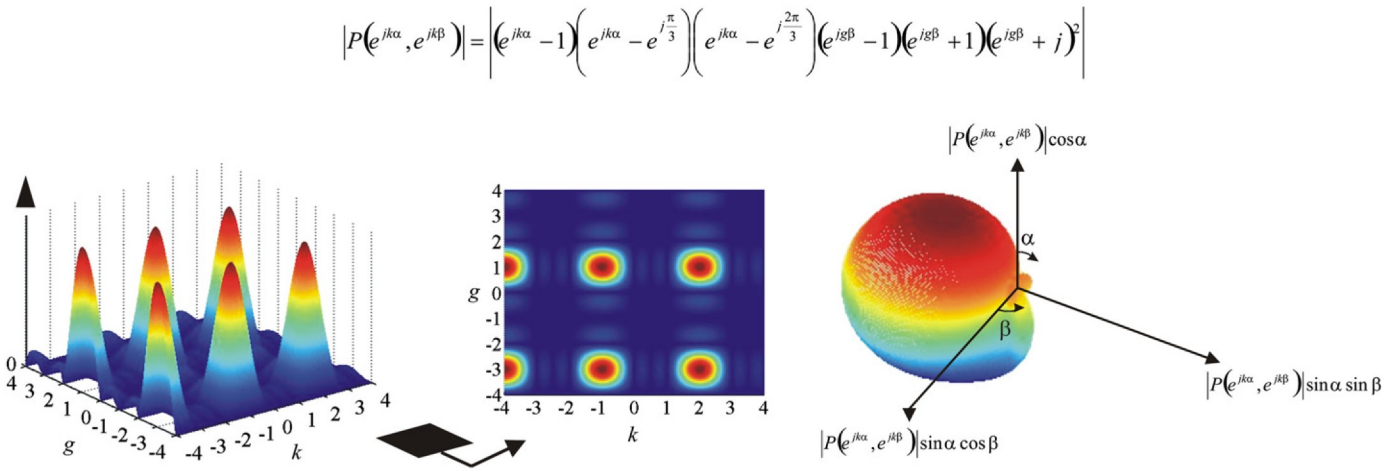

Fig. 4. Module with its plan view (left) and polar diagram (right) of the TDCP for the differential symmetrical 3+1–symmetrical 4+1 TSPSA.

the harmonics a_2b_1 and a_1b_3

$$E[(\phi+\Delta\phi)\pm\phi] = -\frac{a_2}{a_1}\sin 3\phi \mp \frac{b_3}{b_1}\sin[4(\phi+\Delta\phi)] \quad (21)$$

So, we conclude that the linear approach is good in the characterisation of PSAs in most of the cases but not enough to calculate the expression of lower order harmonics in TSPSAs. The TDCP can detect easily the presence of these harmonics. On the other hand, the symmetrical 4+1 PSA is insensitive to detuning error but as the symmetrical 3+1 PSA is not, the additive/differential symmetrical 3+1–symmetrical 4+1 TSPSA is detuning sensitive. Both PSAs should be insensitive to detuning error to transmit this capability to the TSPSA, for example if both patterns employed the symmetrical 4+1 PSA.

4. Experimental application

We employ the PSAs and TSPSAs analysed theoretically above to evaluate a wavefront distortion (WFD). It consists of a relative delay along a phase object located in the test arm of a phase-shifting interferometer. In this case the phase object is an optical window with a 12.5 mm diameter and a 5 mm thickness, being the nominal WDF of $\lambda/10$ per inch. This WFD is related with its geometry and the corresponding change in refractive index distribution along the optical path [1]. The employed optical setup (Fig. 5) is a Twyman-Green interferometer with horizontal collimation (plane *XY*) while the reference and test arms present a vertical configuration (plane *ZY*). A telescope system (formed by a microscope objective, a spatial filter and a collimating lens) produces a parallel wavefront emitted from a He–Ne laser

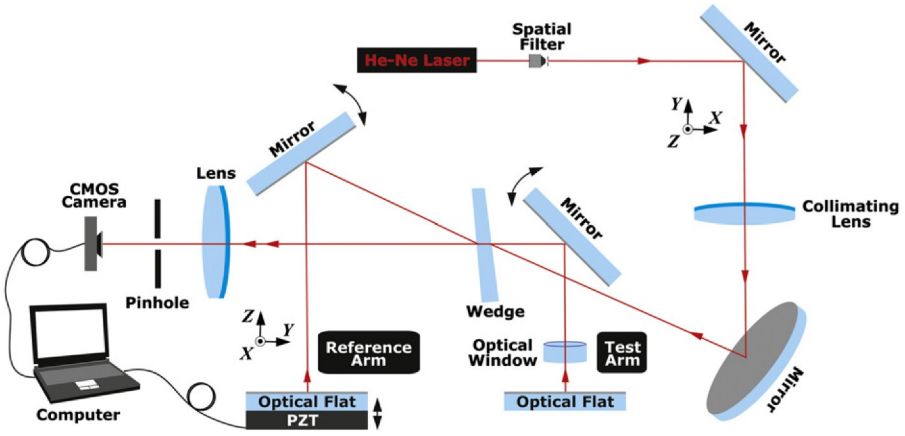

Fig. 5. A phase-shifting Mach-Zehnder interferometer for measuring the wavefront distortion of an optical window.

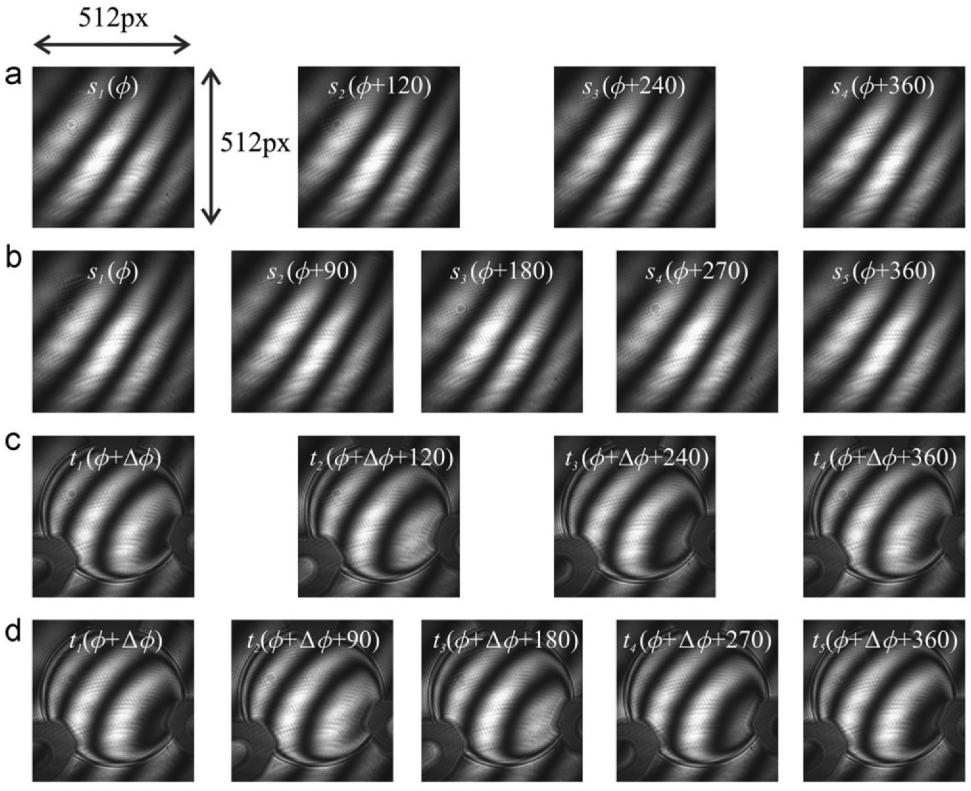

Fig. 6. (a) Original fringe patterns with a phase step of 120°, (b) original fringe patterns with a phase step of 90°, (c) modified fringe patterns with a phase step of 120° and (d) modified fringe patterns with a phase step of 90°.

(632.8 nm). A wedge divides the amplitude of the incident wavefront into parts. The transmitted part travels towards a mirror and latter to an optical surface and it is reflected back as a plane wavefront. The part of the light reflected goes to a second mirror with a piezoelectric transducer (PZT) and after reflection impinges again on the wedge. The tilts of these mirrors can be properly adjusted. The out-of plane displacement of the PZT introduces the needed additional phase terms. A CMOS camera captures two sets of phase-shifted fringe patterns without $s(\mathbf{r},\phi)$ and with $t(\mathbf{r},\phi+\Delta\phi)$ the phase object located at the test Twyman-Green arm. The phase-shifted fringe patterns when the optical window is not inside the interferometer are obtained first and then, once the optical window is located at the test Twyman-Green arm, the corresponding phase-shifted fringe patterns are obtained. In this case the interferometer aberrations affects in the same way both fringe pattern sets and therefore their influence are properly cancelled after the obtained fringe patterns with and without the optical window are combined. In order to employ the differential symmetrical 3+1–symmetrical 4+1 TSPSA (Eq. (20)) the $M=4$ original patterns were 120° phase shifted (Fig. 6a) and the $P=5$ modified patterns were 90° phase shifted (Fig. 6d). We have also acquired $M=5$ patterns 90° phase shifted (Fig. 6b) and $P=4$ patterns 120°phase shifted (Fig. 6c) to compare these results with those obtained with the differential symmetrical

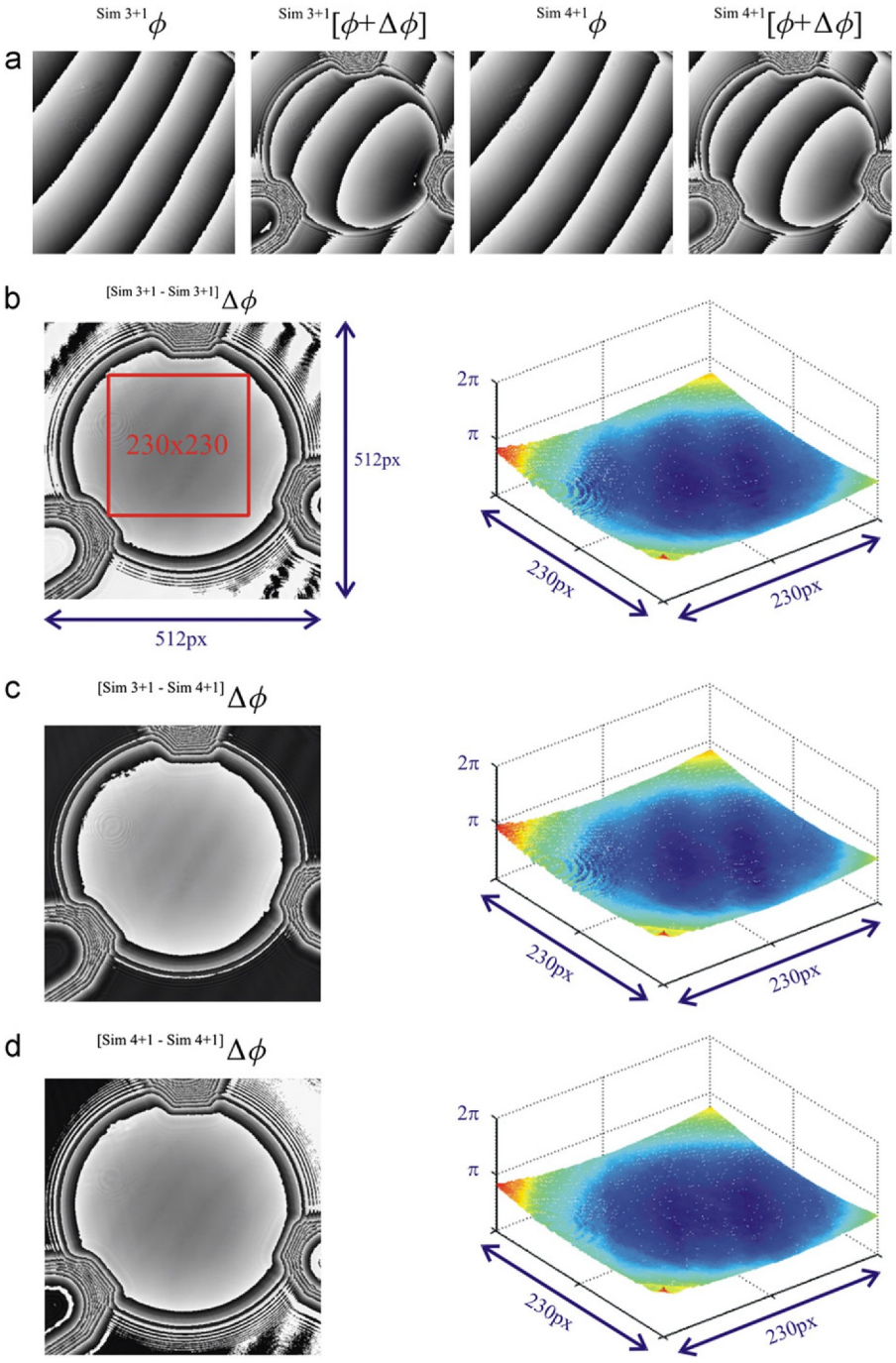

Fig. 7. (a) Phase maps obtained with symmetrical 3+1 and symmetrical 4+1 PSAs. Reconstruction of the phase difference using (b) the differential symmetrical 3+1–symmetrical 3+1 TSPSA, (c) the differential symmetrical 3+1–symmetrical 4+1 TSPSA and (d) the differential symmetrical 4+1–symmetrical 4+1 TSPSA.

3+1–symmetrical 3+1 TSPSA and the differential symmetrical 4+1–symmetrical 4+1 TSPSA, designed with Eq. (13):

$$^{\mathrm{Sim3+1-Sim3+1}}[(\phi+\Delta\phi)\pm\phi] = \arctan\frac{\sqrt{3}(s_1-s_2-s_3+s_4)(t_3-t_2)\pm\sqrt{3}(s_3-s_2)(t_1-t_2-t_3+t_4)}{\mp 3(s_3-s_2)(t_3-t_2)+(s_1-s_2-s_3+s_4)(t_1-t_2-t_3+t_4)} \quad (22a)$$

$$^{\mathrm{Sim4+1-Sim4+1}}[(\phi+\Delta\phi)\pm\phi] = \arctan\frac{2(s_1-2s_3+s_5)(t_4-t_2)\pm 2(s_4-s_2)(t_1-2t_3+t_5)}{\mp 4(s_4-s_2)(t_4-t_2)+(s_1-2s_3+s_5)(t_1-2t_3+t_5)} \quad (22b)$$

In all the cases, we have calculated directly the phase difference

$$\Delta\phi(\mathbf{r}) = \frac{4\pi}{\lambda}\omega(\mathbf{r}) \quad (23)$$

proportional to the desired WFD $\omega(\mathbf{r})$ in a configuration where the test wavefront passes the optical window twice, being λ the illumination wavelength. Fig. 7 shows the phase variation measured corresponding to the optical window. Fig. 7a shows the phase evaluation calculated with symmetrical 3+1 and symmetrical 4+1 PSAs, as the phase maps present discontinuities phase unwrapping is needed. The phase difference in Fig. 7b is calculated with differential symmetrical 3+1–symmetrical 3+1 TSPSA (Eq. (22a)), in Fig. 7c with differential symmetrical 3+1–symmetrical 4+1 TSPSA (Eq. (20)) and in Fig. 7c with differential symmetrical 4+1–symmetrical 4+1 TSPSA (Eq. (22b)). All the calculations show similar results, except for constant term from the initial phases of each pattern, with oscillating errors with less amplitude in Fig. 7d as the differential symmetrical 4+1–symmetrical 4+1 TSPSA is detuning insensitive. Also, in this case, the obtained results for the employed optical window provide a WFD in good agreement with its nominal characteristics. It is important to note that the phase difference does not exceed one complete cycle (Fig. 7b–d) and the delicate unwrapping process is not necessary.

5. Conclusions

Current metrological inspection techniques demand tools that quickly and accurately supply information about the measurement. TSPSAs provide the optical phase sum or difference in a direct calculation. The new TDCP provides an immediate qualitative characterisation of the TSPSA that inversely should allow the design of a TSPSA with the sensitivities required in each system. Direct relations between TDCP theory and Fourier description of TSPSAs are also shown in this work. By knowing the CPs of the PSAs we could construct the TDCP simply by multiplying. Moreover, the sensitivities of the PSAs that build up the TSPSA are intimately related to those of each PSA and the additive TDCP. This tool makes possible to efficiently construct new PSAs with tailored properties simply by combining PSAs with known properties. Experimental results related with wavefront distortion evaluation support the main assumptions.

Acknowledgements

The authors are grateful for funding received from Xunta de Galicia (07DPI002CT) and Ministerio de Ciencia e Innovación (DPI2008-06818-C2-01/DPI).

References

[1] Malacara D. Optical shop testing. John Wiley and Sons; 2007.
[2] Dorrío BV, Fernández JL. Phase-evaluation methods in whole-field optical measurement techniques. Meas Sci Technol 1999;10:33–5.
[3] Morgan CJ. Least-squares estimation in phase-measurement interferometry. Opt Lett 1982;7:368–70.
[4] Greivenkamp JE. Generalized data reduction for heterodyne interferometry. Opt Eng 1984;23:350–2.
[5] Freischlad K, Koliopoulos CL. Fourier description of digital phase-measuring interferometry. J Opt Soc Am 1990;A 7:542–51.
[6] Malacara D, Servín M, Malacara Z. Interferogram analysis for optical testing. Taylor&Francis Group; 2005.
[7] Servín M, Estrada JC, Quiroga JA. Spectral analysis of phase shifting algorithms. Opt Express 2009;17:16423–7.
[8] Servín M, Estrada JC, Quiroga JA. The general theory of phase shifting algorithms. Opt Express 2009;17:21867–81.
[9] Servín M, Estrada JC, Quiroga JA, Mosiño JF, Cywiak M. Noise in phase shifting interferometry. Opt Express 2009;11:8789–94.
[10] Mosiño JF, Servín M, Quiroga JA. Phasorial analysis of detuning error in temporal phase shifting algorithms. Opt Express 2009;17:5618–23.
[11] Mosiño JF, Malacara Doblado D, Malacara Hernández D. Calculus of exact detuning phase shift error in temporal phase shifting algorithms. Opt Express 2009;17:15766–71.
[12] Mosiño JF, Malacara Doblado D, Malacara-Hernández D. A method to design tunable quadrature filters in phase shifting interferometry. Opt Express 2009;17:15772–7.
[13] Surrel Y. Design of algorithms for phase measurements by the use of phase stepping. Appl Opt 1996;35:51–60.
[14] Surrel Y. Additive noise effect in digital phase detection. Appl Opt 1997;36:271–6.
[15] Surrel Y. Design of phase-detection algorithms insensitive to bias modulation. Appl Opt 1997;36:805–7.
[16] Surrel Y. Phase-shifting algorithms for nonlinear and spatially nonuniform phase shifts: comment. J Opt Soc Am 1998;A 15:1227–33.
[17] Surrel Y. Extended averaging and data windowing techniques in phase-stepping measurements: an approach using the characteristic polynomial theory. Opt Eng 1998;37:2314–9.
[18] Surrel Y. Fringe analysis. Top Appl Phys 2000;77:55–102.
[19] Kemao Q, Seah HS, Asundi AK. Algorithm for directly retrieving the phase difference: a generalization. Opt Eng 2003;42:1721–4.
[20] North-Morris M, Millerd J, Brock N, Hayes J. Phase-shifting multi-wavelength dynamic interferometer. Proc SPIE 2004;5531:64–75.
[21] North-Morris M, Millerd J, Brock N, Hayes J, Saif B. Dynamic phase-shifting electronic pattern interferometer. Proc SPIE 2005;5869:58691B.
[22] Novak M, Millerd J, Brock N, North-Morris M, Hayes J, Wyant J. Analysis of a micropolarizer array-based simultaneous phase-shifting interferometer. Appl Opt 2005;44:6861–8.
[23] Viotti MR, Dolinko AE, Galizzi GE, Kaufmann GH. A portable digital speckle pattern interferometry device to measure residual stresses using the hole drilling technique. Opt Lasers Eng 2006;44:1052–66.
[24] Kiire T, Nakadate S, Shibuya M. Simultaneous formation of four fringes by using a polarization quadrature phase-shifting interferometer with wave plates and a diffraction grating. Appl Opt 2008;47:4787–92.
[25] Bhaduri B, Kothiyal MP, Mohan NK. A comparative study of phase-shifting algorithms in digital speckle pattern interferometry. Optik 2008;119:147–52.
[26] Toto-Arellano NI, Rodriguez-Zurita G, Meneses-Fabian C, Vazquez-Castillo JF. Phase shifts in the Fourier spectra of phase gratings and phase grids: an application for oneshot phaseshifting interferometry. Opt Express 2008;16:19330–41.
[27] Cordero RR, François M, Lira I, Vial-Edwards C. Whole-field analysis of uniaxial tensile tests by Moiré interferometry. Opt Lasers Eng 2005;43:919–36.
[28] Ghiglia DC, Pritt MD. Two dimensional phase unwrapping. Wiley; 1998.
[29] Stetson KA, Brohinsky WR. Electrooptic holography and its application to hologram interferometry. Appl Opt 1985;24:3631–7.
[30] Saldner H, Molin N, Stetson K. Fourier-transform evaluation of phase data in spatially phase-biased TV holograms. Appl Opt 1996;35:332–6.
[31] Burke J, Helmers H. Complex division as a common basis for calculating phase differences in electronic speckle pattern interferometry in one step. Appl Opt 1998;37:2589–90.
[32] Miranda M, Dorrío BV. Error behaviour in differential phase-shifting algorithms. Proc SPIE 2008;7102. (71021B-1–71021B-9).
[33] Álvarez-Valado V, González-Jorge H, Dorrío BV, Miranda M, Rodríguez F, Valencia JL, Yebra FJ, Rodríguez J. Testing phase-shifting algorithms for uncertainty evaluation in interferometric gauge block calibration. Metrologia 2009;46:637–45.
[34] Miranda M, Dorrío BV. Fourier analysis of two-stage phase-shifting algorithms. J Opt Soc Am 2010;A 27:276–85.
[35] Miranda M, Álvarez-Valado V, Dorrío BV, González-Jorge H. Error propagation in differential phase evaluation. Opt Express 2010;18:3199–209.
[36] Miranda M, Dorrío BV. Monte Carlo based techniques of two-stage phase shifting algorithms. Opt Lasers Eng 2011;49:439–44.
[37] Larkin KG, Oreb BF. Design and assessment of symmetrical phase-shifting algorithms. J Opt Soc Am 1992;A 9:1740–8.

CAPÍTULO 3. ESTUDIO DE ALGORITMOS DIFERENCIALES DE DESPLAZAMIENTO DE FASE PARA MEDIDAS DE BPL

3.2. LINEAR ERROR ANALYSIS OF DIFFERENTIAL PHASE SHIFTING ALGORITHMS

RESUMEN

Un importante proceso en la metrología óptica es la determinación de la diferencia entre los elementos de prueba y de referencia. Se puede realizar el cálculo directo de la diferencia de fase óptica codificada en dos patrones de franjas utilizando algoritmos de desplazamiento de fase diferencial (DPSA). Si la diferencia de fase no alcanza un período completo, los DPSA proporcionan directamente sus valores continuos y se evitan las conocidas limitaciones de la etapa de desenrollado de fase (*unwrapping*). Este trabajo presenta un protocolo genérico de diseño de DPSAs obtenidos por un ajuste de mínimos cuadrados que combina algoritmos de desplazamiento de fase (PSAs) de una forma no lineal. También se proporcionan resultados que caracterizan cuantitativamente el efecto de las principales fuentes sistemáticas de error sobre algunos DPSA representativos. La efectividad de los DPSA analizados se contrasta con los resultados experimentales de la evaluación de la distorsión del frente de onda utilizando patrones de franjas de Mach-Zehnder con desplazamiento de fase.

PALABRAS CLAVE

Phase shifting interferometry, Differential phase shifting algorithms, Systematic errors, Least squares fitting, Mach-Zehnder.

PUBLICACIÓN ORIGINAL

M. Miranda, B.V. Dorrio, J. Blanco, J. Diz-Bugarin, "*Linear error analysis of differential phase shifting algorithms*", Optik - International Journal for Light and Electron Optics, Vol. 124, Issue 8, 2013, pp. 710-717, ISSN 0030-4026. https://doi.org/10.1016/j.ijleo.2012.02.006

Optik 124 (2013) 710–717

Contents lists available at SciVerse ScienceDirect

Optik

journal homepage: www.elsevier.de/ijleo

Linear error analysis of differential phase shifting algorithms

M. Miranda*, B.V. Dorrío, J. Blanco, J. Diz-Bugarin

Applied Physics Department, University of Vigo, Campus Universitario 36310, Vigo, Spain

ARTICLE INFO

Article history:
Received 9 September 2011
Accepted 11 January 2012

Keywords:
Phase shifting interferometry
Differential phase shifting algorithms
Systematic errors
Least squares fitting
Mach–Zehnder

ABSTRACT

An important process in optical metrology is the determination of the difference between test and reference states. Direct calculation of the optical phase difference encoded in two fringe patterns can be done by using differential phase shifting algorithms (DPSAs). If the phase difference does not reach a complete period, DPSAs provide directly its continuous values and the known limitations of the unwrapping stage are avoided. This work presents a generic design protocol of DPSAs obtained by a least squares fitting that combines phase shifting algorithms (PSAs) in a suitable non-linear way. Results are also provided that quantitatively characterize the effect on some representative DPSAs by the main systematic error sources. The goodness of the analyzed DPSAs is contrasted with the experimental results for wavefront distortion evaluation using phase-shifted Mach–Zehnder fringe patterns.

1. Introduction

The direct result provided from a large number of optical metrology techniques [1,2] are two-dimensional distributions of irradiance values $s(\mathbf{r},\phi)$ with a functional multi harmonic dependence with the optical phase $\phi(\mathbf{r})$, where $\mathbf{r}$ denotes the spatial coordinates of the image plane. The most popular decoding processes provide the optical phase $\phi(\mathbf{r})$ making use of so-called phase shifting algorithms (PSAs) [3–5]. These combine a series of M irradiance values specifically shifted relative phase increments α_m with an harmonic contribution mainly weighted by the local background $a_0(\mathbf{r})$ and the modulation amplitude of the fundamental harmonic $a_1(\mathbf{r})/a_0(\mathbf{r})$

$$s_m(\mathbf{r},\phi,\alpha_m)=\sum_{k=0}^{\infty}a_k(\mathbf{r})\cos[k(\phi(\mathbf{r})+\alpha_m)]=\sum_{k=0}^{\infty}\{E_{1k}(\mathbf{r},\phi)\cos(k\alpha_m)+E_{2k}(\mathbf{r},\phi)\sin(k\alpha_m)\} \tag{1}$$

where the i-coefficients $E_{ik}(\mathbf{r},\phi)$ are the kth harmonics in quadrature without modulating in phase of $s_m(\mathbf{r},\phi,\alpha_m)$. Usually, a perfect sinusoidal profile fringe pattern ($a_k=0$ para $k>1$) is considered. Then, the coefficients $E_{1k}(\mathbf{r},\phi)$ and $E_{2k}(\mathbf{r},\phi)$ can be obtained by a least squares fitting [6] of these irradiance values to a sinusoidal function to retrieve the optical phase as

$$\phi(\mathbf{r})=-\frac{1}{k}\arctan\frac{E_{2k}(\mathbf{r},\phi)}{E_{1k}(\mathbf{r},\phi)}=\arctan\frac{N_1\{s_m(\mathbf{r},\phi,\alpha_m)\}}{D_1\{s_m(\mathbf{r},\phi,\alpha_m)\}} \tag{2}$$

where $N_1\{s_m(\mathbf{r},\phi,\alpha_m)\}$ and $D_1\{s_m(\mathbf{r},\phi,\alpha_m)\}$ are the numerator and denominator of the employed PSA. They are usually linear combinations of the irradiance values $s_m(\mathbf{r},\phi,\alpha_m)$ and if equally spaced relative phase increments are taken in a single signal period $\alpha_m=2\pi(m-1)/M=(m-1)\alpha$ [7] Eq. (2) can be written as

$$^{M,\alpha}\phi(\mathbf{r})=-\frac{\sum_{m=1}^{M}s_m(\mathbf{r},\phi,\alpha_m)\sin\alpha_m}{\sum_{m=1}^{M}s_m(\mathbf{r},\phi,\alpha_m)\cos\alpha_m} \tag{3}$$

It is very common that a posterior phase unwrapping process was needed to obtain a continuous phase map but as it is known this delicate stage shows troubles when the fringe patterns show noise, have low modulation, show abrupt phase changes or a low sampling density [8].

In many current situations – strain and displacement analysis by electronic speckle pattern interferometry, digital holography, moiré interferometry, wave front distortion measurements, wave front error estimation, multiple wavelength interferometry calibration

* Corresponding author. Tel.: +34 986813490.
E-mail addresses: marta_miranda@uvigo.es (M. Miranda), bvazquez@uvigo.es (B.V. Dorrío), jblanco@uvigo.es (J. Blanco), jbugarin@uvigo.es (J. Diz-Bugarin).

0030-4026/$ – see front matter © 2012 Elsevier GmbH. All rights reserved.
doi:10.1016/j.ijleo.2012.02.006

procedures or residual error analyses [9–22] – the measuring magnitude is related to the optical phase difference $\Delta\phi(\mathbf{r})$ coded in two fringe patterns: the original one $s(\mathbf{r},\phi)$ and another modified one $t(\mathbf{r},\phi+\Delta\phi)$ with P irradiance values in the form

$$t_p(\mathbf{r},\phi+\Delta\phi,\beta_p)=\sum_{g=0}^{\infty}b_g(\mathbf{r})\ \cos[g(\phi(\mathbf{r})+\Delta\phi(\mathbf{r})+\beta_p)] \tag{4}$$

with harmonic amplitudes b_g and additional phase shift β_p equally spaced in a whole period. The phase $\phi(\mathbf{r})+\Delta\phi(\mathbf{r})$ of this pattern can be recovered in the same way as the original one (Eq. (2)) but combining the modified irradiance values

$$^{P,\beta}[\phi(\mathbf{r})+\Delta\phi(\mathbf{r})]=\arctan\frac{N_2\{t_p(\mathbf{r},\phi+\Delta\phi,\beta_p)\}}{D_2\{t_p(\mathbf{r},\phi+\Delta\phi,\beta_p)\}}=-\frac{\sum_{p=1}^{P}t_p(\mathbf{r},\phi+\Delta\phi,\beta_p)\ \sin\beta_p}{\sum_{p=1}^{P}t_p(\mathbf{r},\phi+\Delta\phi,\beta_p)\ \cos\beta_p} \tag{5}$$

where $N_2\{t_p(\mathbf{r},\phi+\Delta\phi,\beta_p)\}$ and $D_2\{t_p(\mathbf{r},\phi+\Delta\phi,\beta_p)\}$ define the particular PSA of the modified pattern. Thus, the phase difference $\Delta\phi(\mathbf{r})$ can be determined by using both PSAs, Eqs. (2) and (5), with a duplication of the evaluation and unwrapping processes and a subtraction of the results obtained. However, differential phase shifting algorithms (DPSAs) can provide $\Delta\phi(\mathbf{r})$ directly in a unique evaluation process. The unwrapping stage cannot be necessary if the obtained phase difference does not reach a complete period. We find several DPSAs in the literature, hardly without studying, that do not follow a systematic design method [9–11] and we therefore call specific DPSAs (SDPSAs). In this work the concept of differential phase evaluation is reviewed and a least-square design protocol, that offers a creation strategy of generic DPSAs (GDPSAs), is presented. Unfortunately, all DPSAs are susceptible to systematic errors, such as phase-miscalibration or the presence of higher harmonics in the fringe profile. The paper presents a quantitative analysis of the sensitivity of different DPSAs that can easily be extrapolated to any other DPSA. This study is checked by means of an evaluation with phase-shifted Mach–Zehnder fringe patterns.

2. Least-square estimation in differential phase evaluation

A least squares fitting, similar to that used in the design of PSAs [6], can be applied for the P phase shifted irradiance values of the modified pattern. So, Eq. (4) can be rewritten as

$$t_p(\mathbf{r},\phi+\Delta\phi,\beta_p)=b_0(\mathbf{r})+\sum_{g=1}^{\infty}[F_{1g}(\mathbf{r},\phi,\Delta\phi)\cos(g\beta_p)+F_{2g}(\mathbf{r},\phi,\Delta\phi)\ \cos(g\beta_p)+F_{3g}(\mathbf{r},\phi,\Delta\phi)\ \sin(g\beta_p)+F_{4g}(\mathbf{r},\phi,\Delta\phi)\ \sin(g\beta_p)] \tag{6}$$

where the j-coefficients $F_{jg}(\mathbf{r},\phi,\Delta\phi)$ are the gth harmonics in quadrature without modulating in phase of $t_p(\mathbf{r},\phi+\Delta\phi,\beta_p)$ that provide the optical phase difference $\Delta\phi(\mathbf{r})$, and also the individual phases $\phi(\mathbf{r})$ and $\phi(\mathbf{r})+\Delta\phi(\mathbf{r})$, once isolated in the form:

$$\phi(\mathbf{r})=-\frac{1}{g}\arctan\frac{F_{3g}(\mathbf{r},\phi,\Delta\phi)}{F_{1g}(\mathbf{r},\phi,\Delta\phi)} \tag{7a}$$

$$\Delta\phi(\mathbf{r})=\frac{1}{g}\arctan\frac{F_{2g}(\mathbf{r},\phi,\Delta\phi)}{F_{3g}(\mathbf{r},\phi,\Delta\phi)} \tag{7b}$$

$$\phi(\mathbf{r})+\Delta\phi(\mathbf{r})=-\frac{1}{g}\arctan\frac{F_{3g}(\mathbf{r},\phi,\Delta\phi)+F_{4g}(\mathbf{r},\phi,\Delta\phi)}{F_{1g}(\mathbf{r},\phi,\Delta\phi)+F_{2g}(\mathbf{r},\phi,\Delta\phi)} \tag{7c}$$

Considering $P\geq 4$ measurements, the best fit to a sinusoidal function will give the $F_{jg}(\mathbf{r},\phi,\Delta\phi)$ coefficients that minimize the variance σ^2:

$$\sigma^2=\frac{1}{P}\sum_{p=1}^{P}[b_0(\mathbf{r})+F_{1g}(\mathbf{r},\phi,\Delta\phi)\cos(g\beta_p)+F_{2g}(\mathbf{r},\phi,\Delta\phi)\ \cos(g\beta_p)+F_{3g}(\mathbf{r},\phi,\Delta\phi)\ \sin(g\beta_p)$$
$$+F_{4g}(\mathbf{r},\phi,\Delta\phi)\ \sin(g\beta_p)-t_p(\mathbf{r},\phi+\Delta\phi,\beta_p)]^2 \tag{8}$$

The obtainable equations system can be rewritten in matrix form as

$$\begin{pmatrix} P & \sum_{p=1}^{P}\sum_{g=1}^{\infty}\cos g\beta_p & \sum_{p=1}^{P}\sum_{g=1}^{\infty}\sin g\beta_p \\ \sum_{p=1}^{P}\sum_{g=1}^{\infty}\cos g\beta_p & \sum_{p=1}^{P}\sum_{g=1}^{\infty}\cos^2 g\beta_p & \sum_{p=1}^{P}\sum_{g=1}^{\infty}\sin g\beta_p\cos g\beta_p \\ \sum_{p=1}^{P}\sum_{g=1}^{\infty}\sin g\beta_p & \sum_{p=1}^{P}\sum_{g=1}^{\infty}\sin g\beta_p\cos g\beta_p & \sum_{p=1}^{P}\sum_{g=1}^{\infty}\sin^2 g\beta_p \end{pmatrix} \begin{pmatrix} b_0(\mathbf{r}) \\ \sum_{g=1}^{\infty}[F_{1g}(\mathbf{r},\phi,\Delta\phi)+F_{2g}(\mathbf{r},\phi,\Delta\phi)] \\ \sum_{g=1}^{\infty}[F_{3g}(\mathbf{r},\phi,\Delta\phi)+F_{4g}(\mathbf{r},\phi,\Delta\phi)] \end{pmatrix}$$

$$= \begin{pmatrix} \sum_{p=1}^{P} t_p(\mathbf{r},\phi+\Delta\phi,\beta_p) \\ \sum_{p=1}^{P}\sum_{g=1}^{\infty} t_p(\mathbf{r},\phi+\Delta\phi,\beta_p)\ \cos g\beta_p \\ \sum_{p=1}^{P}\sum_{g=1}^{\infty} t_p(\mathbf{r},\phi+\Delta\phi,\beta_p)\ \sin g\beta_p \end{pmatrix} \tag{9}$$

and be considerably simplified if equally spaced relative phase increments are taken in a single signal period $\beta_p = 2\pi(p\text{-}1)/P = (p\text{-}1)\beta$

$$\begin{pmatrix} P & 0 & 0 \\ 0 & \frac{P}{2} & 0 \\ 0 & 0 & \frac{P}{2} \end{pmatrix} \begin{pmatrix} b_0(\mathbf{r}) \\ \sum_{g=1}^{\infty}[F_{1g}(\mathbf{r},\phi,\Delta\phi)+F_{2g}(\mathbf{r},\phi,\Delta\phi)] \\ \sum_{g=1}^{\infty}\left[F_{3g}(\mathbf{r},\phi,\Delta\phi)+F_{4g}(\mathbf{r},\phi,\Delta\phi)\right] \end{pmatrix} = \begin{pmatrix} \sum_{p=1}^{P} t_p(\mathbf{r},\phi+\Delta\phi,\beta_p) \\ \sum_{p=1}^{P}\sum_{g=1}^{\infty} t_p(\mathbf{r},\phi+\Delta\phi,\beta_p)\ \cos g\beta_p \\ \sum_{p=1}^{P}\sum_{g=1}^{\infty} t_p(\mathbf{r},\phi+\Delta\phi,\beta_p)\ \sin g\beta_p \end{pmatrix} \tag{10}$$

and thus relate the $F_{jg}(\mathbf{r},\phi,\Delta\phi)$ coefficients in the way given in Eq. (7b) to recover, for example, $\Delta\phi(\mathbf{r})$:

$$\tan\Delta\phi(\mathbf{r}) = \frac{\frac{\sum_{g=1}^{\infty}[F_{1g}(\mathbf{r},\phi,\Delta\phi)+F_{2g}(\mathbf{r},\phi,\Delta\phi)]}{\sum_{g=1}^{\infty}[F_{3g}(\mathbf{r},\phi,\Delta\phi)+F_{4g}(\mathbf{r},\phi,\Delta\phi)]} - \frac{\sum_{g=1}^{\infty}F_{1g}(\mathbf{r},\phi,\Delta\phi)}{\sum_{g=1}^{\infty}F_{3g}(\mathbf{r},\phi,\Delta\phi)}}{1+\frac{\sum_{g=1}^{\infty}[F_{1g}(\mathbf{r},\phi,\Delta\phi)+F_{2g}(\mathbf{r},\phi,\Delta\phi)]}{\sum_{g=1}^{\infty}[F_{3g}(\mathbf{r},\phi,\Delta\phi)+F_{4g}(\mathbf{r},\phi,\Delta\phi)]}\frac{\sum_{g=1}^{\infty}F_{1g}(\mathbf{r},\phi,\Delta\phi)}{\sum_{g=1}^{\infty}F_{3g}(\mathbf{r},\phi,\Delta\phi)}} = \frac{-\frac{\sum_{p=1}^{P} t_p\ \cos\beta_p}{\sum_{p=1}^{P} t_p\sin\beta_p} + \frac{\sum_{m=1}^{M} s_m\cos\alpha_m}{\sum_{m=1}^{M} s_m\sin\alpha_m}}{1+\frac{\sum_{p=1}^{P} t_p\cos\beta_p}{\sum_{p=1}^{P} t_p\sin\beta_p}\frac{\sum_{m=1}^{M} s_m\cos\alpha_m}{\sum_{m=1}^{M} s_m\sin\alpha_m}} \tag{11}$$

Finally, it is obtained an equation that can be expressed according to a non linear combination of the irradiance values for its PSA precursors, in agreement with Eqs. (3), (5), (7a)–(7c):

$${}^{M+P,\alpha,\beta}\Delta\phi(\mathbf{r}) = \arctan\frac{D_1\{s_m(\mathbf{r},\phi,\alpha_m)\}N_2\{t_p(\mathbf{r},\phi+\Delta\phi,\beta_p)\} - N_1\{s_m(\mathbf{r},\phi,\alpha_m)\}D_2\{t_p(\mathbf{r},\phi+\Delta\phi,\beta_p)\}}{N_1\{s_m(\mathbf{r},\phi,\alpha_m)\}N_2\{t_p(\mathbf{r},\phi+\Delta\phi,\beta_p)\} + D_1\{s_m(\mathbf{r},\phi,\alpha_m)\}D_2\{t_p(\mathbf{r},\phi+\Delta\phi,\beta_p)\}} \tag{12}$$

Note that these GDPSAs do not necessarily have to combine their original $s_m(\mathbf{r},\phi,\alpha_m)$ and modified $t_p(\mathbf{r},\phi+\Delta\phi,\beta_p)$ patterns with the same precursor PSA. Of course, Eq. (12) can also be obtained by proper combinations of trigonometric formulae [23–25] but in this way no information about the transfer of sensitivity from precursors PSA is obtained.

3. Linear approximation for systematic errors in differential evaluation

In previous works [26–29], we have shown qualitatively the good behavior of some DPSAs by means of the Monte Carlo method or a Fourier analysis. In this case, we undertake an in-depth study of the main causes of systematic errors by analyzing the sensitivity of some selected DPSAs to errors in phase modulation and the presence of undesired harmonics in the pattern profiles. Knowing the specific features of each error with regard its amplitude and specific functional dependence makes it possible to choose a DPSA according to the error that can be predicted in the system and to draw up strategies for error compensation or even cancellation. A strategy based on error linearization is followed backed by a computer simulation of the process to get a quantitative result that is easy to compare among distinct DPSAs.

In what follows, by way of example, we employ the Stetson SDPSA [9]:

$${}^{4+4,\pi/2,\pi/2}\Delta\phi = \arctan\frac{(s_1-s_3-t_2+t_4)^2+(s_2-s_4+t_1-t_3)^2-(s_1-s_3+t_2-t_4)^2-(s_2-s_4-t_1+t_3)^2}{(s_1-s_3+t_1-t_3)^2+(s_2-s_4+t_2-t_4)^2-(s_1-s_3-t_1+t_3)^2-(s_2-s_4-t_2+t_4)^2} \tag{13}$$

and, on the other hand, the Creath [4] (14a) and Schwider–Hariharan [30,31] (14b) GDPSAs, which use the same PSA in the original and modified patterns:

$$^{3+3,\pi/2,\pi/2}\Delta\phi = \arctan\frac{(s_1 - s_2)(t_3 - t_2) - (s_3 - s_2)(t_1 - t_2)}{(s_3 - s_2)(t_3 - t_2) + (s_1 - s_2)(t_1 - t_2)} \tag{14a}$$

$$^{5+5,\pi/2,\pi/2}\Delta\phi = \arctan\frac{(2s_3 - s_1 - s_5)(2t_2 - 2t_4) - (2s_2 - 2s_4)(2t_3 - t_1 - t_5)}{(2s_3 - s_1 - s_5)(2t_3 - t_1 - t_5) + (2s_2 - 2s_4)(2t_2 - 2t_4)} \tag{14b}$$

3.1. Error effect in the additional phase

The main systematic error source that affects the optical phase difference $\Delta\phi(\mathbf{r})$ decoding process is possibly the discrepancy in the nominal value of the relative phase increments (α_m,β_p) of the original $s_m(\mathbf{r},\phi,\alpha_m)$ and modified $t_p(\mathbf{r},\phi+\Delta\phi,\beta_p)$ patterns. Thus, the generic expression for the calibration error in linear approximation [3] for a DPSA of M shifts in the original pattern and P shifts in the modified one is

$$E\Delta\phi(\mathbf{r}) = \sum_{m=1}^{M}\left(\frac{\partial\Delta\phi}{\partial s_m}\right)\left(\frac{\partial s_m}{\partial\alpha_m}\right)E\alpha_m + \sum_{p=1}^{P}\left(\frac{\partial\Delta\phi}{\partial t_p}\right)\left(\frac{\partial t_p}{\partial\beta_p}\right)E\beta_p \tag{15}$$

quantifying $(E\alpha_m,E\beta_p)$ the magnitude of the error between the phase shifts affected by the error and the ideal ones

$$E\alpha_m = \sum_{q=1}^{\infty}\varepsilon_q\frac{\alpha_m^q}{q\pi^{q-1}} \tag{16a}$$

$$E\beta_p = \sum_{r=1}^{\infty}\chi_r\frac{\beta_p^r}{r\pi^{r-1}} \tag{16b}$$

with (ε_q,χ_r) being the qth and rth error coefficients in each pattern.

Eqs. (17a)–(17c) show the results of this lineal approximation for the Stetson SDPSA (17a) and the Creath (17b) and Schwider–Hariharan (17c) GDPSAs to first ($q=1$ and $r=1$) and second order ($q=2$ and $r=2$) calibration error where we assume the DC term and the visibility of both patterns unitary constants ($a_0=b_0=1$ and $a_1/a_0=b_1/b_0=1$):

$$E\Delta\phi = \frac{\pi\varepsilon_1}{2}\sin\Delta\phi\sin(2\phi+\Delta\phi) + \frac{\pi\varepsilon_2}{8}\sin\Delta\phi\sin(2\phi+\Delta\phi) \tag{17a}$$

$$E\Delta\phi = -\frac{\pi\varepsilon_1}{2}\sin\Delta\phi\sin(2\phi+\Delta\phi) + \frac{\pi\varepsilon_2}{32}\sin\Delta\phi[-13\sin(2\phi+\Delta\phi) + 4\cos(2\phi+\Delta\phi)] \tag{17b}$$

$$E\Delta\phi = \frac{\pi\varepsilon_2}{8}\sin\Delta\phi\sin(2\phi+\Delta\phi) \tag{17c}$$

Fig. 1 shows the Eqs. (17a)–(17c) considering a first order and second order error of 10% positive in the phase shifts (α_m,β_p). A periodical nature is observed in the error $E\Delta\phi(\mathbf{r})$, in accord with the Fourier representation of these GDPSAs [26,29] and the shift property of the arctan function used to calculate $\Delta\phi(\mathbf{r})$ [27], with a sinusoidal dependence in multiples of the phases $\phi(\mathbf{r})$ and $\phi(\mathbf{r})+\Delta\phi(\mathbf{r})$.

The use of compensated PSAs – as is the case of the well-known Schwider–Hariharan PSA – leads equally to detuning error (first order error in the phase shift) compensated GDPSAs and show good second order behavior (Eq. (17c)).

3.2. Effect of the presence of harmonics in the pattern profile

If multi frequential patterns ($k>1$ (Eq. (1)) and $g>1$ (Eq. (4))) are assumed, an error $E\Delta\phi(\mathbf{r})$ is produced in the recovered phase whose expression in linear approximation [3] for a DPSA is

$$E\Delta\phi(\mathbf{r}) = \sum_{m=1}^{M}\left(\frac{\partial\Delta\phi}{\partial s_m}\right)Es_m + \sum_{p=1}^{P}\left(\frac{\partial\Delta\phi}{\partial t_p}\right)Et_p \tag{18}$$

where the deviation from the average is in the form:

$$Es_m(\mathbf{r},\phi) = \sum_{k=2}^{\infty}a_k(\mathbf{r})\cos[k(\phi(\mathbf{r})+\alpha_m)] \tag{19a}$$

$$Et_p(\mathbf{r},\phi+\Delta\phi) = \sum_{g=2}^{\infty}b_g(\mathbf{r})\cos[g(\phi(\mathbf{r})+\Delta\phi(\mathbf{r})+\beta_p)] \tag{19b}$$

Eqs. (20a)–(20c) show the sensitivity of the analyzed DPSAs to the presence of second ($k=2$ and $g=2$) and third order ($k=3$ and $g=3$) harmonics in the signal profile being (20a) the error of Stetson SDPSA and (20b) and (20c) the error of Creath and Schwider–Hariharan GDPSAs respectively. Again, a periodical nature is observed in the error $E\Delta\phi(\mathbf{r})$ with a sinusoidal dependence in multiples of the phases of both patterns (Fig. 2):

$$E\Delta\phi = \frac{a_3}{2a_1}\sin4\phi - \frac{b_3}{2b_1}\sin[4(\phi+\Delta\phi)] \tag{20a}$$

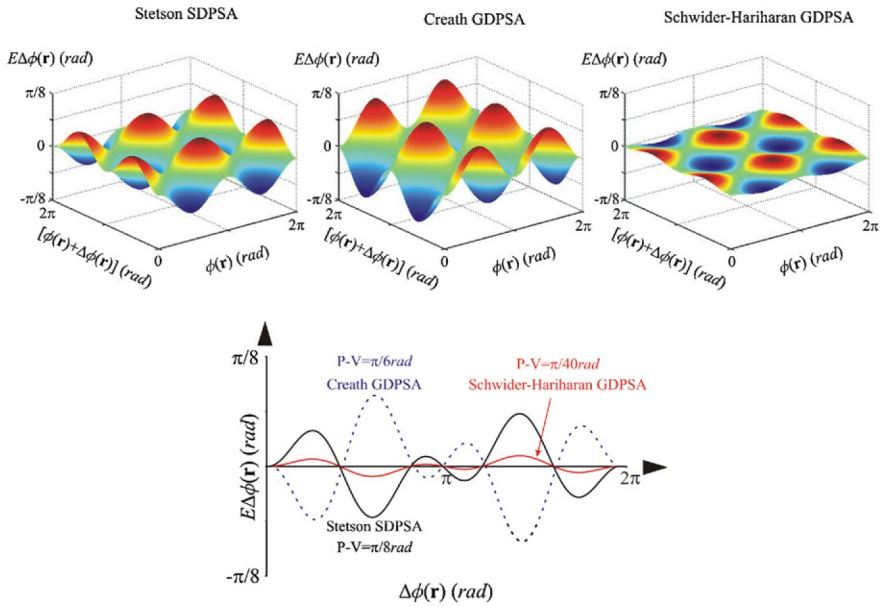

Fig. 1. Analytical simulation of phase error $E\Delta\phi(\mathbf{r})$ for 10% error in the first ($\varepsilon_1 = 0.1$, $\chi_1 = 0.1$) and second ($\varepsilon_2 = 0.1$, $\chi_2 = 0.1$) order phase shift for the analyzed DPSAs. Up depending on the phases of both of the patterns $\phi(\mathbf{r})$ and $\phi(\mathbf{r}) + \Delta\phi(\mathbf{r})$ and down a profile depending on the phase difference $\Delta\phi(\mathbf{r})$.

$$E\Delta\phi = -\left[\frac{\sqrt{2}a_2}{a_1}\sin 2\phi(\sin\phi - \cos\phi) + \frac{a_3}{a_1}\sin 4\phi\right] + \left\{\frac{\sqrt{2}b_2}{b_1}\sin[2(\phi+\Delta\phi)][\sin(\phi+\Delta\phi) - \cos(\phi+\Delta\phi)] + \frac{b_3}{b_1}\sin[4(\phi+\Delta\phi)]\right\} \tag{20b}$$

$$E\Delta\phi = \frac{a_3}{2a_1}\sin 4\phi - \frac{b_3}{2b_1}\sin[4(\phi+\Delta\phi)] \tag{20c}$$

We have obtained in the Section 3.1 that the Schwider–Hariharan GDPSA is insensitive to small detuning error and now Eq. (20c) shows that the second harmonic is no detected, nor in the Stetson SDPSA. As expected Schwider–Hariharan GDPSA provide a good compromise between computational complexity and susceptibility to errors. In general, it can be observed that GDPSAs transfer the compensatory capabilities from precursor PSAs in such a way that the error associated to the GDPSAs coincides with the difference of the errors linked to

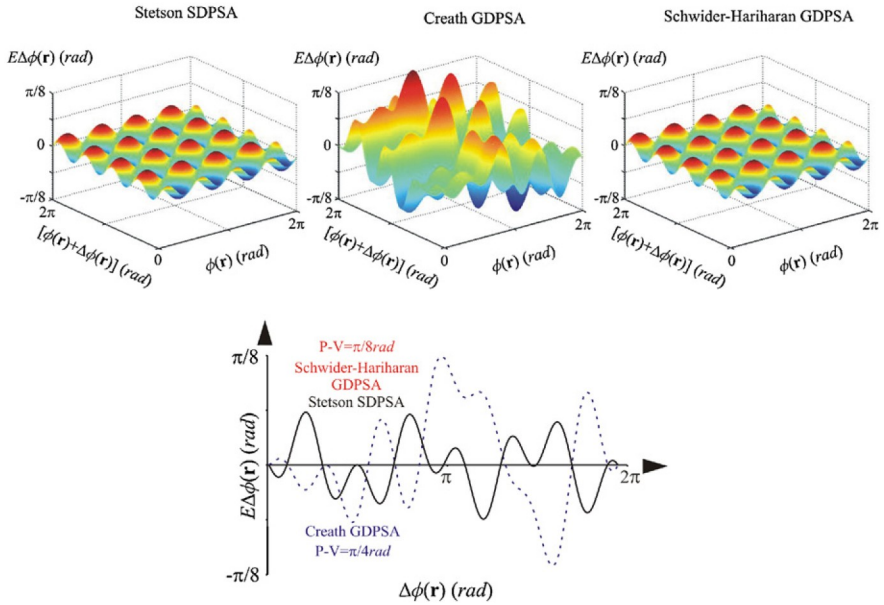

Fig. 2. Analytical simulation of the phase error $E\Delta\phi(\mathbf{r})$ due to the presence of second ($a_2 = b_2 = 0.1$) and third ($a_3 = b_3 = 0.1$) order harmonics for the analyzed DPSAs. Up depending on the phases of both of the patterns $\phi(\mathbf{r})$ and $\phi(\mathbf{r}) + \Delta\phi(\mathbf{r})$ and down a profile depending on the phase difference $\Delta\phi(\mathbf{r})$.

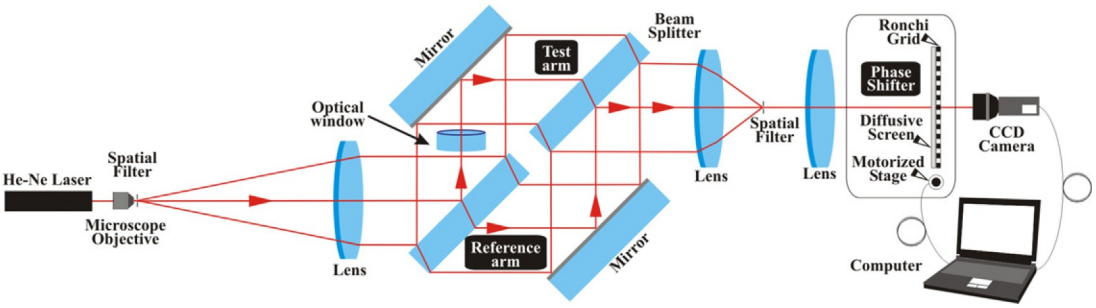

Fig. 3. Experimental setup.

each of its precursor PSAs. So it is possible to design a well-compensated GDPSA making use of known sensibilities of the precursor PSAs, such as Schwider–Hariharan GDPSA.

4. Experimental procedure

The DPSAs analyzed theoretically above have been used in evaluating the optical quality of a transparent optical window (Fig. 3). The usual interferometric procedure [32,33] is based on the calculation of the wavefront distortion (WFD) when a light beam crosses it. In our case the proper information is coded in a set of phase-shifted Mach–Zehnder fringe patterns. The main characteristics of the employed experimental moiré multiplicative phase-modulation have been previously reported [34–36]. This mechanical phase modulation requires the utilization of a high-frequency linear spatial carrier into the Mach–Zehnder interferogram. The decodification is carried out by the direct superimposition of this phase-modulated carrier on a Ronchi grid (with a similar period to the linear carrier) placed outside the Mach–Zehnder interferometer. On the grid plane, the product of the phase-modulated Mach–Zehnder carrier irradiance and the grid transmission function is obtained. With the aim of keeping this multiplicative moiré irradiance distribution a diffusive screen is located just before the grid. Among the various terms in the multiplicative moiré pattern, the term of highest period (the moiré image) is considered to be the term of interest and it is isolated from the rest by low-pass filtering. The phase of this fringe pattern with a sinusoidal profile is the difference between the Mach–Zehnder phase and the grid phase and, therefore, the moiré image phase contains an additional phase term proportional to the in-plane translation of the grating. Finally, phase modulation is produced through an in-plane displacement of a motorized stage controlled by computer.

In this way, a set of moiré images with different values of the additional phase term are obtained (Fig. 4). The WFD of an optical window fabricated with a 10 mm diameter, a 6 mm thickness and a nominal WFD of the order of $\lambda/10$ per 25 mm is calculated by proper combination in a DPSA of two sets of these phase-shifted fringe patterns with and without the refractive object located at the test Mach–Zehnder interferometer. The phase-shifted fringe patterns $s_m(\mathbf{r},\phi,\alpha_m)$ when the optical window is not inside the interferometer are obtained first and then, once the optical window is located at the Mach–Zehnder arm, the corresponding phase-shifted fringe patterns ${}^1t_p(\mathbf{r},\phi+\Delta\phi,\beta_p)$ are obtained.

These phase-shifted fringe patterns are combined (Fig. 5) according to Eqs. (13), (14a) and (14b) to obtain directly the phase difference

$$\Delta\phi(\mathbf{r}) = \frac{2\pi}{\lambda}\omega(\mathbf{r}) \tag{21}$$

proportional to the desired WFD $\omega(\mathbf{r})$, being λ the illumination wavelength. The phase-difference calculation can also be employed to evaluate the variability of the obtained measurements if fringe patterns with similar information ${}^2t_p(\mathbf{r},\phi',\beta_p)$ are employed. In this situation if the phase variation to be measured does not exceed one complete cycle the delicate unwrapping process is not necessary (Fig. 6). Then,

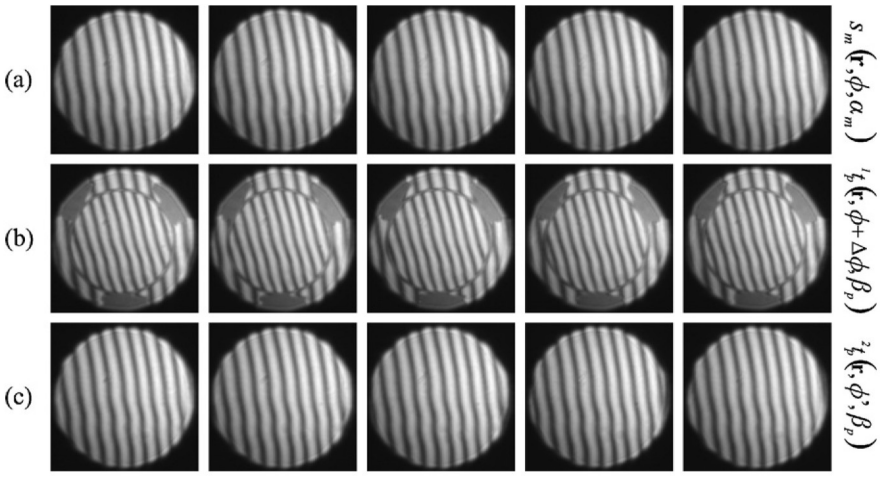

Fig. 4. Fringe patterns for WFD evaluation in a phase-shifting Mach–Zehnder interferometer (a) interferometer without the test object $s_m(\mathbf{r},\phi,\alpha_m)$; (b) test object located in the measurement area ${}^1t_p(\mathbf{r},\phi+\Delta\phi,\beta_p)$; (c) test object removed from the measurement area ${}^2t_p(\mathbf{r},\phi',\beta_p)$.

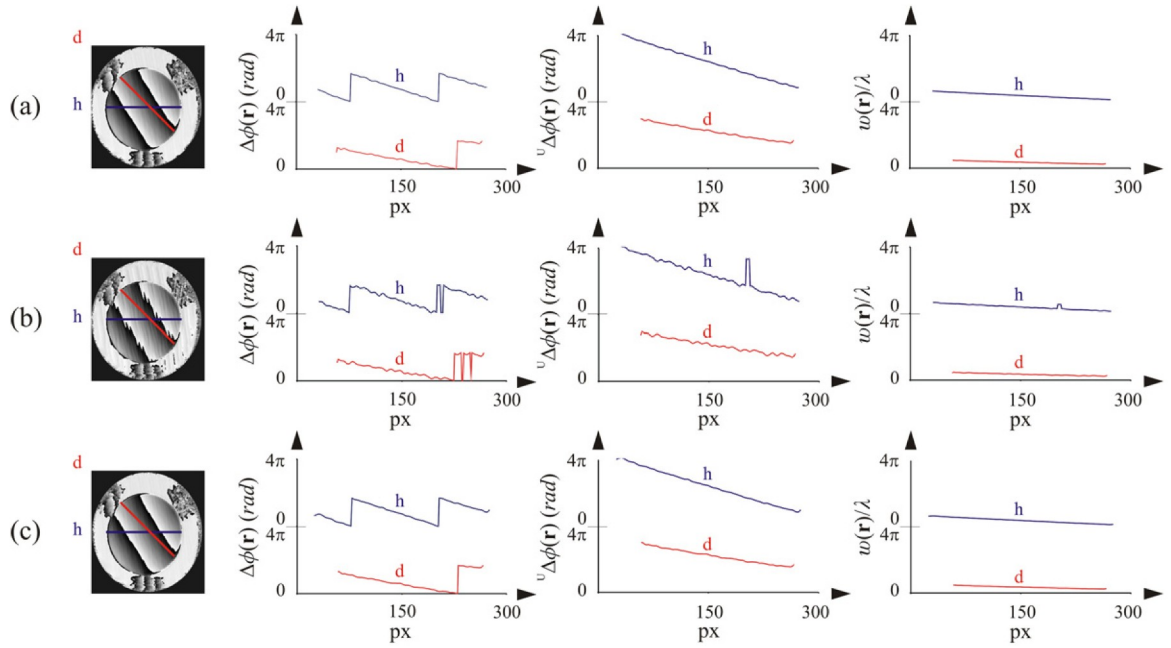

Fig. 5. Phase difference $\Delta\phi(\mathbf{r})$ related with the WFD of the transparent object and its profile for the analyzed DPSAs (a) Stetson SDPSA, (b) Creath GDPSA and (c) Schwider–Hariharan GDPSA. Fringe patterns shown in Fig. 4a $s_m(\mathbf{r},\phi,\alpha_m)$ and Fig. 4b ${}^1t_p(\mathbf{r},\phi+\Delta\phi,\beta_p)$ are employed.

the results obtained through these interferograms show a poor margin of repetibility, possibly due to environmental pertubations during measuring process.

In most of the phase difference maps calculated, without additional pre- or post-processing protocols, it can clearly be seen that there are oscillating errors like the ones shown in Figs. 1 and 2 as well as sudden phase jumps linked to variations in the DC term and in the irradiance modulation amplitude. The Creath GDPSA, even when only three irradiance values are employed, obtains profiles comparable to those of the Schwider–Hariharan GDPSAs but this shows a great compromise as it is insensitive to detuning with second order compensatory capabilities and it is also insensitive to the second harmonic.

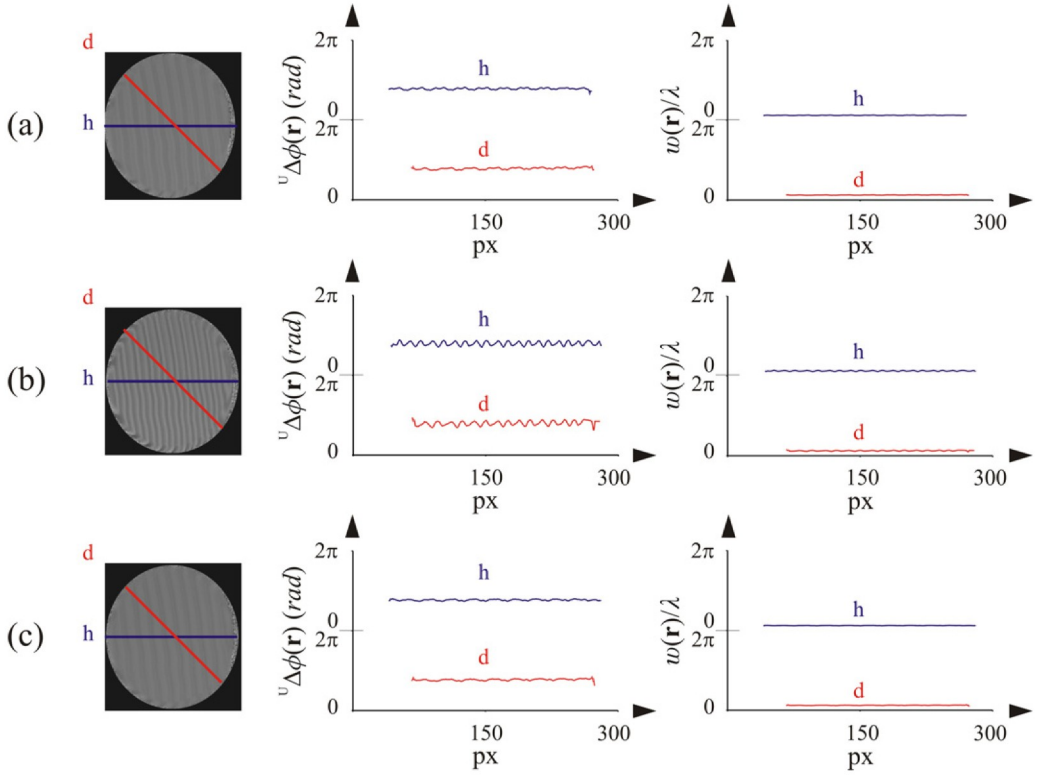

Fig. 6. Phase difference, $\phi(\mathbf{r})-\phi'(\mathbf{r})$, related with variability of the measurements and their profiles for the analyzed DPSAs (a) Stetson SDPSA, (b) Creath GDPSA and (c) Schwider–Hariharan GDPSA. Fringe patterns shown in Fig. 4a $s_m(\mathbf{r},\phi,\alpha_m)$ and Fig. 4c ${}^2t_p(\mathbf{r},\phi',\beta_p)$ are employed.

5. Conclusions

The need to design new DPSAs that are optimized against the usual error sources stems from the great advantages that these algorithms offer when directly calculating phase difference, even making the delicate unwrapping process unnecessary if the phase variation to be measured does not exceed one complete cycle, as opposed to the use of PSAs that otherwise duplicate the evaluation process and later phase unwrapping is needed. In this work, GDPSAs are deduced in a novel way from the modified pattern by means of a least squares fitting similar to that used in the design of PSAs. The obtained GDPSA provide the least-square determination of the differential phase distribution when the phase shifts of the sinusoidal phase-stepped fringe patterns are accurately known, but the phase shifts are hard to know exactly and higher order harmonics are usually present and therefore a decrease in the measurement accuracy is achieved.

In this work the strategy used for error analysis is based on a linear approximation in phase difference $\Delta\phi(\mathbf{r})$ error that provides analytical expressions for the error that can be used in a later process of error reduction.

The analyses undertaken show that GDPSAs show interesting compensatory capabilities inherited from their precursors. Furthermore, as the same PSA has been used in the original and the modified pattern, it has become clear that the error of the GDPSAs is propagated in a way that coincides with the difference of the errors linked to each of its PSA precursors. For the two error types analyzed a periodical nature is observed in the error with a sinusoidal dependence in multiples of the phases of both patterns. Since the error effect on the phases is systematic, its effect on the phase differences is small, the phase difference uncertainties provided by the DPSAs reduce as the number of phase-shifted fringe patterns increase.

The experimental results obtained with Mach–Zehnder fringe patterns corroborate the properties of the analyzed DPSAs and indicate virtues and sensitivities against non-linearities and variations in local average irradiance or visibility that must be taken into account.

Acknowledgments

The authors gratefully acknowledge the support from the Xunta de Galicia (Project 07DPI002CT) and the Ministerio de Educación y Ciencia (Project DPI2008-06818-C2-01/DPI).

References

[1] B.V. Dorrío, J.L. Fernández, Phase-evaluation methods in whole-field optical measurement techniques, Meas. Sci. Technol. 10 (1999) 33–35.
[2] D. Malacara, M. Servín, Z. Malacara, Interferogram Analysis for Optical Testing, Taylor & Francis Group, 2005.
[3] J.V. Wingerden, H.J. Frankena, C. Smorenburg, Linear approximation for measurement errors in phase shifting interferometry, Appl. Opt. 30 (1991) 2718–2729.
[4] K. Creath, Error sources in phase measuring interferometry, Proc. SPIE 1720 (1992) 428–435.
[5] C. Joenathan, Phase measuring interferometry: new methods and error analysis, Appl. Opt. 33 (1994) 4147–4155.
[6] J.E. Greivenkamp, Generalized data reduction for heterodyne interferometry, Opt. Eng. 23 (1984) 350–352.
[7] C.J. Morgan, Least-squares estimation in phase-measurement interferometry, Opt. Lett. 7 (1982) 368–370.
[8] D.C. Ghiglia, M.D. Pritt, Two Dimensional Phase Unwrapping, Wiley, 1998.
[9] K.A. Stetson, Theory and applications of electronic holography, in: Proc. SEM Conference on Hologram Interferometry and Speckle Metrology, 1990, pp. 294–300.
[10] M. Owner-Petersen, Digital speckle pattern shearing interferometry: limitations and prospects, Appl. Opt. 30 (1991) 2730–2738.
[11] C.S. Vikram, W.K. Whiterow, J.D. Trolinger, Algorithm for phase-difference measurement in phase-shifting interferometry, Appl. Opt. 32 (1993) 6250–6252.
[12] Q. Kemao, H.S. Seah, A.K. Asundi, Algorithm for directly retrieving the phase difference: a generalization, Opt. Eng. 42 (2003) 1721–1724.
[13] M. North-Morris, J. Millerd, N. Brock, J. Hayes, Phase-shifting multi-wavelength dynamic interferometer, Proc. SPIE 5531 (2004) 64–75.
[14] M. Novak, J. Millerd, N. Brock, M. North-Morris, J. Hayes, J. Wyant, Analysis of a micropolarizer array-based simultaneous phase-shifting interferometer, Appl. Opt. 44 (2005) 6861–6868.
[15] R.R. Cordero, M. François, I. Lira, C. Vial-Edwards, Whole-field analysis of uniaxial tensile tests by Moiré interferometry, Opt. Lasers Eng. 43 (2005) 919–936.
[16] M. North-Morris, J. Millerd, N. Brock, J. Hayes, B. Saif, Dynamic phase-shifting electronic pattern interferometer, Proc. SPIE 5869 (2005) 58691B.
[17] M.R. Viotti, A.E. Dolinko, G.E. Galizzi, G.H. Kaufmann, A portable digital speckle pattern interferometry device to measure residual stresses using the hole drilling technique, Opt. Lasers Eng. 44 (2006) 1052–1066.
[18] T. Kiire, S. Nakadate, M. Shibuya, Simultaneous formation of four fringes by using a polarization quadrature phase-shifting interferometer with wave plates and a diffraction grating, Appl. Opt. 47 (2008) 4787–4792.
[19] B. Bhaduri, M.P. Kothiyal, N.K. Mohan, A comparative study of phase-shifting algorithms in digital speckle pattern interferometry, Optik 119 (2008) 147–152.
[20] N.I. Toto-Arellano, G. Rodriguez-Zurita, C. Meneses-Fabian, J.F. Vazquez-Castillo, Phase shifts in the Fourier spectra of phase gratings and phase grids: an application for oneshot phase-shifting interferometry, Opt. Express 16 (2008) 19330–19341.
[21] U. Paul Kumar, B. Bhaduri, M.P. Kothiyal, N. Krishna Mohan, Two-wavelength micro-interferometry for 3-D surface profiling, Opt. Lasers Eng. 47 (2009) 223–229.
[22] J. Vargas, N. Uribe-Patarroyo, J.A. Quiroga, A. Álvarez-Herrero, T. Belenguer, Optical inspection of liquid crystal variable retarder inhomogeneities, Appl. Opt. 49 (2010) 568–574.
[23] K.A. Stetson, W.R. Brohinsky, Electrooptic holography and its application to hologram interferometry, Appl. Opt. 24 (1985) 3631–3637.
[24] H. Saldner, N. Molin, K. Stetson, Fourier-transform evaluation of phase data in spatially phase-biased TV holograms, Appl. Opt. 35 (1996) 332–336.
[25] J. Burke, H. Helmers, Complex division as a common basis for calculating phase differences in electronic speckle pattern interferometry in one step, Appl. Opt. 37 (1998) 2589–2590.
[26] M. Miranda, B.V. Dorrío, Fourier analysis of two-stage phase-shifting algorithms, J. Opt. Soc. Am. A 27 (2010) 276–285.
[27] M. Miranda, V. Álvarez-Valado, B.V. Dorrío, H. González-Jorge, Error propagation in differential phase evaluation, Opt. Express 18 (2010) 3199–3209.
[28] M. Miranda, B.V. Dorrío, Monte Carlo based techniques of two-stage phase shifting algorithms, Opt. Lasers Eng. 49 (2011) 439–444.
[29] M. Miranda, B.V. Dorrío, J. Blanco, J. Diz-Bugarín, F. Ribas, Characteristic polynomial theory of two-stage phase shifting algorithms, Opt. Lasers Eng. 50 (2012) 522–528.
[30] J. Schwider, R. Burow, K.E. Elssner, J. Grzanna, R. Spolaczyk, K. Merkel, Digital wave-front measuring interferometry: some systematic error sources, Appl. Opt. 22 (1983) 3421–3432.
[31] P. Hariharan, B.F. Oreb, T. Eiju, Digital phase-shifting interferometry: a simple error-compensating phase calculation algorithm, Appl. Opt. 26 (1987) 2504–2506.
[32] D. Malacara, Optical Shop Testing, Wiley, New York, 1992.
[33] J.D. Briers, Optical testing: a review and tutorial for optical engineers, Opt. Lasers Eng. 32 (1999) 111–138.
[34] B.V. Dorrío, A.F. Doval, C. López, R. Soto, J. Blanco-García, J.L. Fernández, M. Pérez-Amor, Fizeau phase measuring interferometry using the moiré effect, Appl. Opt. 34 (1995) 3639–3643.
[35] B.V. Dorrío, C. López, A.F. Doval, M. Pérez-Amor, J.L. Fernández, Transparent object analysis in a Mach–Zehnder interferometer using the multiplicative analogical moiré phase-shifting method, Proc. SPIE 3744 (1999) 94–100.
[36] B.V. Dorrío, D. Cernadas, C. Trillo, A.F. Doval, C. López, M. Pérez-Amor, J.L. Fernández, A multiplicative analogical moiré phase-shifting Twyman–Green technique for Nd:YAG rod wavefront distortion measurement, Meas. Sci. Technol. 12 (2001) 103–110.

CAPÍTULO 4. DISEÑO DE UN MEDIDOR INTERFEROMÉTRICO DE LONGITUD DE ONDA CON MICROCONTROLADOR MEDIANTE EL MÉTODO VERNIER

RESUMEN

Este artículo presenta un nuevo tipo de contador electrónico de franjas para la medida de longitud de onda de un diodo láser en un interferómetro por el método Vernier. El sistema está pensado como alternativa de bajo coste a los sistemas comerciales para la calibración de Bloques Patrón. La etapa de contadores y el detector de coincidencia de fase se han hecho con un microcontrolador y circuitos lógicos CMOS de alta velocidad para alcanzar la resolución requerida. El microcontrolador se puede sincronizar con otros elementos para realizar un sistema completamente automatizado. Este diseño electrónico mejora la resolución de los contadores electrónicos utilizados en diseños previos.

PALABRAS CLAVE

Instrumentation, Microcontrollers, Photodetectors, Laser Diodes.

PUBLICACIÓN ORIGINAL

© 2022 IEEE. Reprinted, with permission, from J. Diz-Bugarín, I. Outumuro-González, J. B. Vázquez-Dorrío, J. L. Valencia-Álvarez and J. Blanco-García, "*Design of a New Microcontroller-Based Vernier Fringe Counter for Interferometric Measurement of Laser Wavelength*" in IEEE Transactions on Instrumentation and Measurement, vol. 65, no. 2, pp. 407-412, Feb. 2016, doi: 10.1109/TIM.2015.2482258.

AUTORIZACIÓN PARA PUBLICACIÓN WEB

Design of a new microcontroller-based Vernier fringe counter for interferometric measurement of laser wavelength

Javier Diz-Bugarín, Ismael Outumuro-González, J. Benito Vázquez-Dorrío,
José L. Valencia-Álvarez, Jesús Blanco-García

***Abstract*— This paper presents a new electronic Vernier fringe counter for wavelength measurement of a diode laser in a scanning interferometer. The system is intended to be a low cost alternative to commercial systems used for gauge block calibration. The counter stage and phase coincidence detector are made with a microcontroller and high speed CMOS logic to achieve the required resolution. The microcontroller also can synchronize with other elements to make a fully automated measurement system. This electronic design improves the resolution of the electronic counters in previous designs.**

***Index Terms*— Instrumentation, Microcontrollers, Photodetectors, Laser Diodes**

I. INTRODUCTION

Scanning interferometer wavemeters carry out the measurement of a laser wavelength using two laser sources, one of them is unknown and the other one is calibrated and used as reference. Its operation mode consists in measuring the changes of the fringe pattern caused by the optical path difference of the beams, which is produced by the movement of the arms of a Michelson interferometer. Both laser beams suffer the same path variation but produce a different number of interference fringes because of their different wavelengths, therefore an accurate count of the number of fringes provides the unknown wavelength according to (1), where λ_R and λ_U are the reference and unknown wavelengths, and N_R and N_U are the number of fringes of the reference and unknown lasers.

$$\lambda_U = \left(\frac{N_R}{N_U} \right) \lambda_R \quad (1)$$

This equation has been simplified taking into account that the difference of the values of the refractive index for reference and unknown wavelengths is not significant because both laser wavelengths are similar [1-6].

The outputs of the interferometer are processed through an electronic system that counts the interference fringes of both lasers. The electronic system is based on a fringe counter which is composed of photodetectors (photodiodes, phototransistors, APD), an analog processing circuit and a digital counter. To achieve sub-fringe precision several techniques can be employed, like fringe multiplication with PLL circuits [7] or Vernier coincidence detection [8].

The PLL method consists of multiplying the fringe frequency by a high factor, typically 100 or more, before applying the signal to the digital counters. This method requires a steady control of the displacement velocity of the mobile arms of the interferometer to achieve a high frequency stability.

Vernier method for fringe counting starts and stops when there is a phase coincidence between the two interference signals. With this method N_R and N_U are always integer numbers and the main source of error is produced by the resolution of the electronic circuits used to detect the coincidence.

II. EXPERIMENTAL SETUP

This paper is focused on the new electronic system of a Michelson wavemeter designed to give traceability to the wavelength of external cavity diode lasers (ECDL).

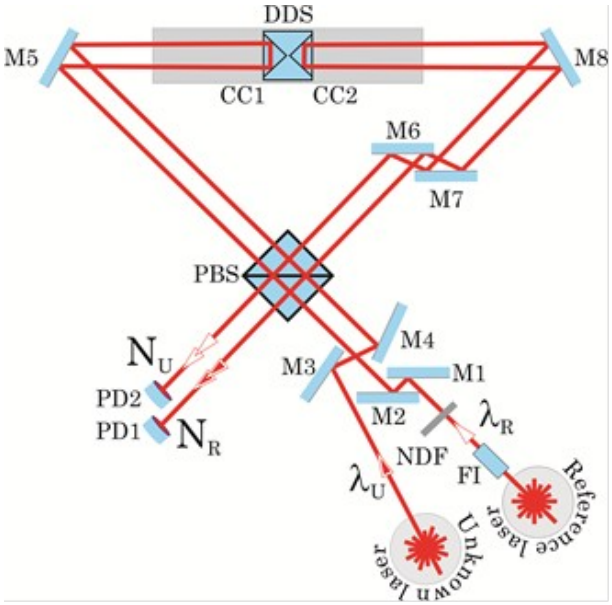

Fig. 1. Scanning Michelson interferometer setup: reference laser, unknown laser, direct drive stage (DDS), corner cubes (CC), mirrors (M), Faraday isolator (FI), photodetectors (PD), neutral density filter (NDF) and polarized beam splitter (PBS).

This system is intended to be a low cost alternative to commercial systems with better characteristics. Fig.1 shows the configuration of our experimental setup [9].

The interferometer employs a calibrated He-Ne laser as reference and an ECDL as unknown laser. The path variation is obtained by a Thorlabs DDS220/M motorized stage which moves at constant velocity. This stage has a maximum displacement of 220 mm, large enough to continuously acquire about 1,400,000 interference fringes for laser wavelengths about 633 nm in one direction travel. A Vernier coincidence detection is used to improve the accuracy of the system. Fig. 2 shows the prototype mounted in the LOMG Laboratory.

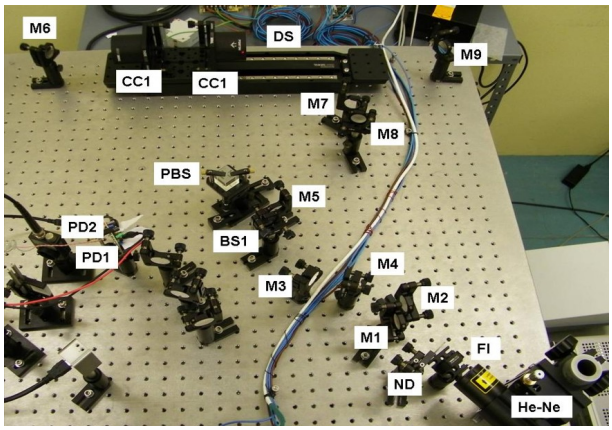

Fig. 2. Protoype mounted at LOMG (Laboratorio Oficial de Metroloxía de Galicia, Spain)

The system presented in this work improves the previous designs [10] in modularity and flexibility by means of a microcontroller board, that implements the counter stage and Vernier detector and can be easily modified to improve the characteristics of the wavemeter incorporating analog-to-digital converters to process the signal by digital algorithms. Besides it can communicate with a computer to receive control commands, send results and synchronize with the motorized stage of the interferometer.

III. System description

The electronic system is divided into four modules: analog module, digital interface with coincidence detector, microcontroller module and auxiliary generator.

A. Analog Module

The analog module consists of a transimpedance amplifier and an active filter. This is critical for the accuracy of the system because of a small signal-to-noise ratio, thus many tests were made to verify its reliability. This module fits in the interferometer, connects with the main unit and has two identical sections composed of a photodiode, a transimpedance amplifier, a voltage preamplifier with filter, a variable gain amplifier and a Schmitt-trigger comparator.

The first prototype was designed with a symmetrical power supply built with voltage regulators LM78L05 and LM79L05. Fig. 3 shows the final assembly of this prototype. The second prototype was designed with a single +5 V supply and a LDO regulator LP2950-3.3 that generates 3.3 V for the reverse polarization of the photodiodes and preamplifier reference. This configuration allows that a single supply can be used for all the analog circuits, although the power supply has separate outputs with different regulators to avoid feedback between the different amplifier stages. The digital circuits have also their own supply with a LM2576 switched regulator.

The Schmitt-trigger comparator has a hysteresis level about 200 mV, which provides noise immunity. The maximum fringe frequency has been limited to 300 kHz, which is enough for the current stage of development, although it is planned to achieve at least 2 MHz with the next prototype.

The operational amplifier TLE2074 from Texas Instruments was used in both prototypes because of its characteristics (low noise, 10 MHz bandwidth, 45 V/µs slew rate and wide supply range in symmetrical and single configuration).

Fig. 4 shows the schematic of the amplifier stages of the analog module (transimpedance and inverter amplifier).

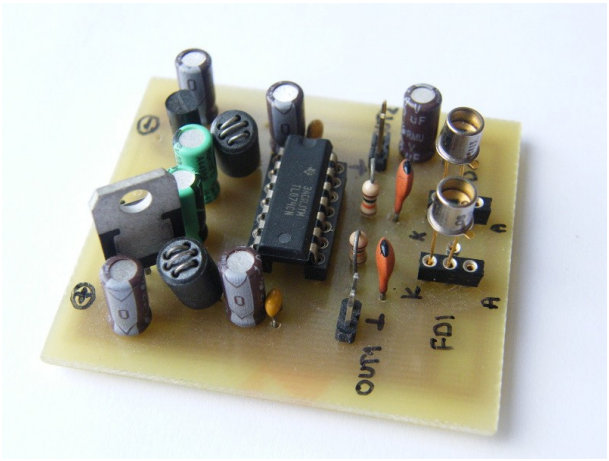

Fig. 3. Analog module pcb with amplifiers and BPX65 photodiodes.

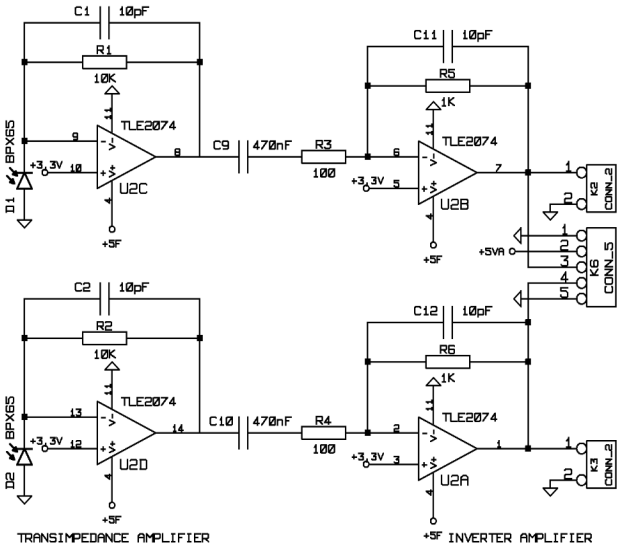

Fig. 4. Schematic of the analog board with transimpedance and preamplifier stages.

B. Coincidence Detector

The second module of the electronic system is the digital interface and coincidence detector. The digital interface module supplies the digital input to the microcontroller and it is responsible for the coincidence detection needed to start and stop the fringe measurements in the Vernier method. Previous designs of the phase coincidence [2,3] used wired logic and old hardware counters like ICL7226. Our circuit is an updated version of those designs, where the counter logic has been replaced by a microcontroller and a hardware coincidence detector has been added to generate an interrupt signal for the microcontroller counters. The coincidence detector produces short pulses in the positive edges of the input signals, using monostables built with a 74HC04 inverter and a RC network. These pulses are combined in a high speed 74HC00 logic gate, which activates a RS flip-flop when both signals are in phase.

The output of this circuit triggers an external interrupt of the microcontroller that starts and stops its counters. The flip-flop is resetted by the microcontroller in order to detect the following coincidences. There is also a led indicator and a manual reset pushbutton to test the circuit without the microcontroller. For the first prototype, the pulse duration has been specified at 100 ns without losing performance, because this pulse duration can achieve a resolution of 10^{-2} per fringe when the input frequency is less than 100 kHz. It is planned to reduce pulse duration to values as low as 10 ns to achieve a resolution of 10^{-3} per fringe.

The coincidence detector has also a digital mixer made with a nand gate and a low pass filter with a cut-off frequency of a few kHz. The difference of phase and frequency between the two input signals is the output of this circuit and it serves as an auxiliary detection signal that can be viewed with an oscilloscope. Fig. 5 shows the schematic of the coincidence detector module.

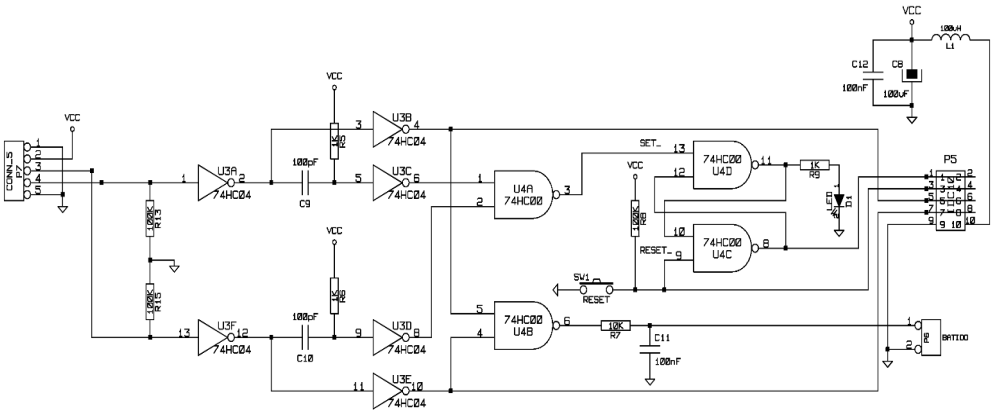

Fig. 5. Schematic of the digital coincidence detector with monostables, flip-flop and digital mixer

Some proposals for the next prototypes of the coincidence detector are the reduction of the pulse width of the monostables, the use of analog to digital converters combined with digital signal processing and a new design based in phase detectors used in PLL circuits like 74HC4046 [11].

C. Control Module

The control module has been designed with a microcontroller that carries out the user interface, fringe counter, Vernier detector and communications. The microcontrollers used belong to the family MCS-51 with In-System Programming (ISP) capabilities, such as Atmel AT89S4051 or AT89S52 [12]. These microcontrollers have high speed 16 bits integrated counters and were extended to 32 bits by software using hardware interrupts, thus the resolution is only limited by acquisition time. The module has a USB connection for ISP, remote control and data transfer to an external computer. There is also an interface board with 2x16 monochrome LCD display and a small keyboard with 4 pushbuttons. Fig. 6 shows the microcontroller board and Fig. 7 the LCD interface board.

The first prototype was made with a 20 pin AT89S4051 microcontroller. This circuit could not manage the communications whereas counting was in progress, for that reason in the second prototype it was changed by AT89S52. This circuit has one more timer and more digital inputs and outputs that can be used for new functions. In addition, the peripheral frequency of the microcontroller limits the input frequency to a maximum of 500 kHz for a 12 MHz quartz crystal. For new designs, the use of single cycle core microcontrollers is planned to allow input frequencies of at least 2 MHz.

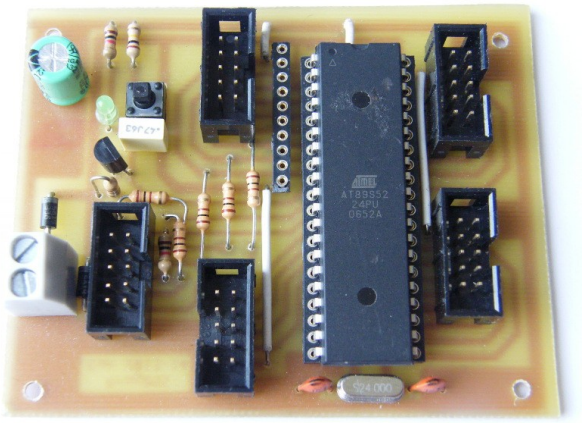

Fig. 6. Control module with AT89S52 microcontroller.

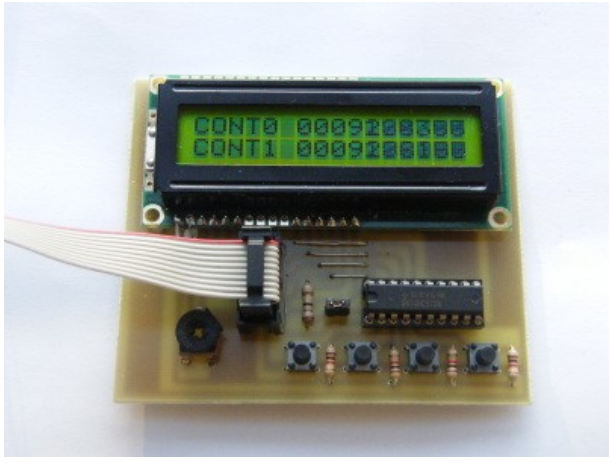

Fig. 7. LCD and keyboard module

The control module menu has three measurement modes, that can be selected by keyboard or remote control. Each mode has assigned a specific mode key and a remote command code. The input configuration of the microcontroller ports allows direct connection of multiple elements to the same pin, so the keyboard and different sensors can be connected in parallel. Another option is an external command sent by USB. This possibility should be carefully used to avoid concurrent commands from multiple sources. When the specific key is pressed or the remote code is received the control module changes to the selected mode and waits for an external order to start or stop measurement. The following paragraphs describe in detail the operation of each mode:

1) Manual counting

In this mode the beginning and end of fringe counting is controlled by the keyboard or an external trigger signal (like a photocoupler or hall effect sensor).

2) Coincidence counting

This mode operates like the manual counting, but in this case the fringe counting is triggered by the coincidence detector. The output of the coincidence detector is connected directly to an external interrupt input of the microcontroller to minimize the delay between the coincidence detection and the beginning or end of counting.

3) Frequency counting

This mode shows the fringe frequency of each input. This information can be useful for signal adjustment and velocity checking of the interferometer. The frequency mode does not use the coincidence detector and its resolution is lower than counting modes.

The microcontroller module allows remote control by an USB external connection. This option opens the possibility of integration with other elements like a motorized stage or position sensors to implement a fully automated measurement system. Furthermore, a large set of measurements can be easily acquired and stored in a computer for statistical analysis.

The USB connection module is based in a FT232R integrated circuit from FTDI. This circuit performs a complete conversion between USB interface and RS232 signals. It allows full-duplex transmissions with a baud rate of 3Mbit/s. This circuit connects directly to RXD and TXD pins of 8051 microcontrollers with TTL logic levels.

The control unit uses the same USB interface both for communications and ISP programming of the microcontroller. For that purpose some of the handshake lines of the FT232R circuit (DTR, RTS, DSR and RI) emulate a SPI serial port that connects to MOSI (P1.5), MISO (P1.6), SCK (P1.7) and RST lines of the microcontroller. This configuration simplifies the design of the control unit and allows a rapid development of the wavemeter prototype.

D. Auxiliary Generator

The auxiliary generator module provides an electronic and optical test signal to check the performance of the digital modules before integrating into the interferometer system in order to verify the accuracy and reliability of the fringe counters. This module has two quartz crystal oscillators with a variable reactance that can be adjusted to slightly change the frequency and a binary counter-divider to select the output range. Each oscillator can be adjusted independently. The module has two outputs, a digital output for direct connection to the microcontroller module to test the digital counters and programs and an optical output with visible led diodes that can be used to test the photodiodes and analog amplifiers. Fig. 8 shows the schematic of the auxiliary generator module.

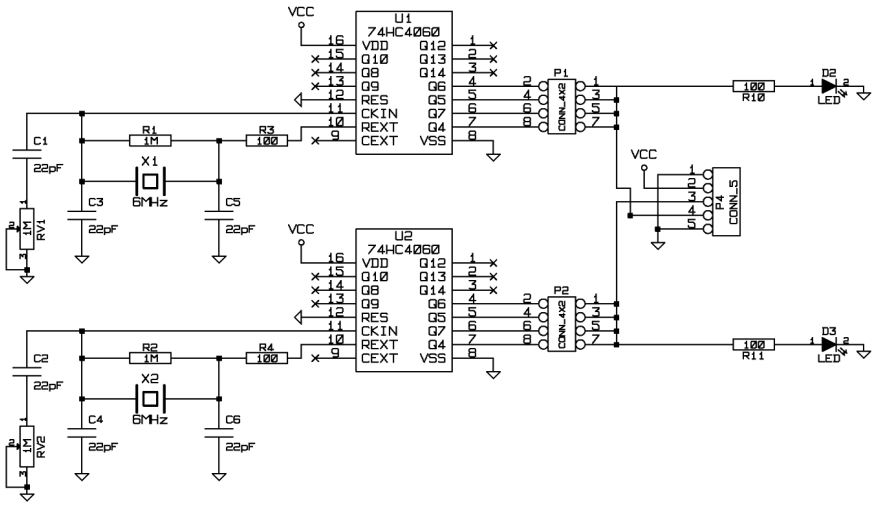

Fig. 8. Schematic of the auxiliary generator.-

IV. Electronic system accuracy and tests

The electronic counter has been designed to display 10 digit values in the LCD module in order to minimize the last digit error truncation. If the maximum value is reached the resolution could be as low as 0.0001 ppm. As the values come from the 32 bit software counters that can reach a maximum value of 4,294,967,296 the real counter resolution is 0.00023 ppm. This resolution is a few orders of magnitude better than the required value for the wavemeter, but if needed the counter size could be increased by reprogrammation of the microcontroller. This design upgrades the resolution of the electronic counters in previous designs that had only eight digits or less [2,8].

If the wavemeter counts separately the number of fringes of each laser source a large number of fringes should be acquired to compensate the error due to the truncation of the fractional part of fringes at start and stop of counting. To achieve a resolution of 0.01 ppm, a number of 10^8 fringes should be acquired.

With the current configuration of the interferometer and a laser wavelength of 633 nm, a distance of 158 mm should provide only 1,000,000 fringes. Moreover, the Thorlabs DDS220/M used in this wavemeter has a maximum displacement of 220 mm. Fig 9. represents the N_R, N_U pairs for a large set of measurements showing its linearity.

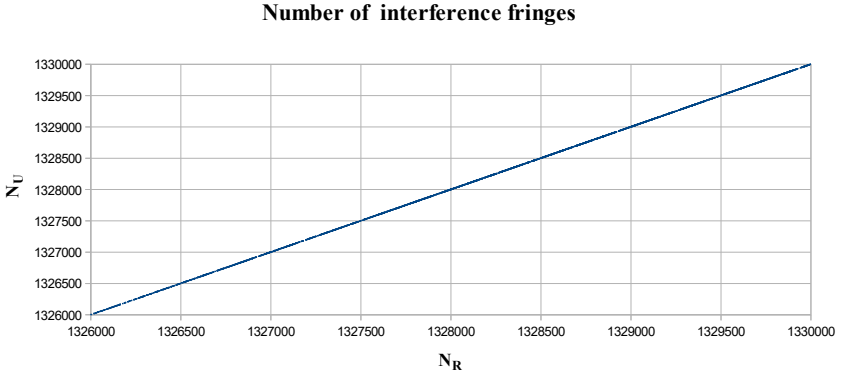

Fig. 9. Linearity of N_R, N_U for a large set of measurements

The use of Vernier method reduces the number of fringes required to achieve the same resolution. With this method the number of fringes in each channel is always an integer value, eliminating most of the error. The main source of error in this case is due to the time resolution of the electronic circuit, and is also related to the fringe frequency. In our prototype, the time resolution of the electronic coincidence detector is 100 ns.

If fringe frequency is lower than 100 kHz the interval between fringes is higher than 10 μs and the resolution is better than 0.01 fringes. If the total number of fringes is more than 1,000,000 a total resolution of 0.01 ppm can be achieved. The main problem in this case is the large acquisition time required (10 s or more). In the next prototype it is planned to use new circuits based in high speed logic that reduce the time resolution to less than 10 ns, allowing acquisition times lower than 1 s.

In order to check the performance of the electronic circuits we have made several tests with the auxiliary generator (that can provide both electronic and optical signals with led diodes) and the final tests with the interferometer and reference laser. The auxiliary generator was adjusted to a frequency of 375 kHz.

To check the analog amplifiers and comparators firstly we have applied an electronic square wave from the auxiliary generator to the counter inputs, and then the same frequency was optically coupled from the led diodes to the photodiodes and analog amplifiers. The results showed that there was no difference between the two signals and the measurement was the same in both cases.

The second test consisted of applying the same optical signal to both counters and verifying that the displayed values were also the same. The measurement time was large enough to achieve a high value in the counters (more than 100,000,000).

To verify the coincidence detector we have adjusted the second oscillator of the auxiliary generator to a slightly different value, with a difference less than 1 Hz in order to appreciate the coincidence points with an oscilloscope. The measurements in this case showed pairs N_R, N_U with different values but with a constant relationship between them (depending on the acquisition time allowed).

The results of these tests demonstrated that the electronic modules work properly with stable digital signals as input.

V. Interferometer Measurements

After integration with the interferometer we made two types of measurements: with only the reference laser and with the reference and unknown lasers. For the first measurement the reference laser was split in two beams and applied as reference and unknown lasers, giving the same number of fringes in both channels of the counter. For the second measurement, several different tests were performed in order to evaluate the uncertainty of the system [13-16].

The first test was carried out using an unknown laser (HP 5519A) and a reference laser (REO Model 32734, standardized by the CEM-Madrid-Spain with a Calibration Code CEM 131641001). In this case, the wavelength measurement was 632.99141 nm with an uncertainty of 0.00016 nm (0.26 ppm), which agrees with the values of 632.9913867 nm and 0.000013 nm obtained by the Metrology Laboratory of the ETSII at the Technical University of Madrid (UPM) for the HP 5519A calibration (Code ENAC 003/LC037).

A second test of the system uncertainty utilized the ECDL as unknown laser and REO Model 32734 as reference laser. These results of wavelength and uncertainty were 632.9922 nm and 0.0013 nm (2.0 ppm), respectively. Fig. 10 shows the wavelength values taken every 13 seconds during a period of 26 hours.

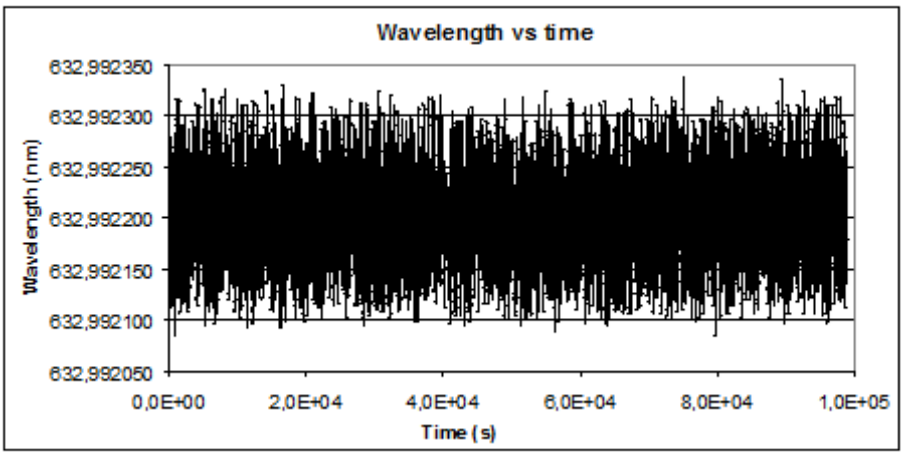

Fig. 10. Fluctuation of the ECDL wavelength in 26 hours.

VI. Conclusions

In conclusion, the results obtained with this new electronic design are good and open the possibility of employing the ECDL for gauge block calibration, but some improvements would be needed in the electronics for this specific application like better resolution in the coincidence detector, more amplification in the analog stages and higher speed in the counters. As this work is focused on the development of the electronic system of the wavemeter the measurement results should be considered as the first tests and not the final results of the complete system. The reference laser used for these tests is not good enough for gauge block calibration and should be replaced by a best one in the final stage of the development. The developed electronic design improves the resolution of the electronic counters in previous designs and allows the synchronization with other elements to make a fully automated measurement system.

Acknowledgment

The authors would like to thank Xunta de Galicia for funding the 15AELE02 Vocational Training Innovation Project.

References

[1] J.-P. Monchalin, M. J. Kelly, J. E. Thomas, N. A. Kurnit, A. Szöke, F. Zernike, P. H. Lee, and A. Javan, "Accurate laser wavelength measurement with a precision two-beam scanning Michelson interferometer", Appl. Opt., vol. 20, no. 5, pp. 736-757, Mar 1981.

[2] P. J. Fox, R. E. Scholten, M. R. Walkiewicz and R. E. Drullinger, "A reliable, compact, and low-cost Michelson wavemeter for laser wavelength measurement", Am. J. Phys., vol. 67, no. 7, pp. 624-630 Jul. 1999.

[3] J. Ishikawa, N. Ito, and K. Tanaka, "Accurate wavelength meter for cw lasers", Appl. Opt., vol. 25, no. 5, pp. 639-643, Mar 1986.

[4] A. Banerjee, U. D. Rapol, A. Wasan, and V. Natarajan, "High-accuracy wavemeter based on a stabilized diode laser", Appl. Phys. Lett., vol 79, no. 2139, 2001.

[5] L. Yan, B. Chen, W. Yang, R. Wei, and S. Zhao, "A novel laser wavelength meter based on the measurement of synthetic wavelength", Rev. Sci. Instrum., vol. 81, no. 11, Nov. 2010.

[6] Jaffee, S. M. and Yen, W. M., "A precision drive for a Michelson wavemeter" Rev. Sci. Instrum. 64, 1459-1462 (1993).

[7] M Braun, J Maier and H Liening, "A high precision compact Michelson-Sagnac wavemeter", J. Phys. E: Sci. Instrum., vol 20 no. 1247, 1987.

[8] A. Kahane, M. S. O'Sullivan, N. M. Sanford and B. P. Stoicheff, "Vernier fringe-counting device for laser wavelength measurements", Rev. Sci. Instrum., vol. 54, no. 1138, 1983.

[9] J. Diz, I. Outumuro, B. V. Dorrío, J. Blanco, M. Miranda, and J. L. Valencia, "Design of an interferometric system for gauge block calibration," Opt. Eng., vol 52, no. 4, pp. 045601-7, Apr. 2013.

[10] M. Ugray, J. E. Atfield, T. G. McCarthy, and R. C. Shiell, "Microcontroller-based wavemeter using compression locking of an internal mirror reference laser", Rev. of Sci. Inst., vol 77, no. 113109, 2006.

[11] "74HC/HCT4046A Phase-locked-loop with VCO" [Online]. Available: http://www.nxp.com/documents/data_sheet/74HC_HCT4046A_CNV.pdf

[12] "Atmel 8051 Architecture ISP Flash Microcontrollers" [Online]. Available: http://www.atmel.com/products/microcontrollers/8051Architecture/flash_isp-in_system_programmable.aspx

[13] I. Outumuro, J. Diz, J. L. Valencia, J. Blanco, B. V. Dorrío, "Uncertainty evaluation and electronic improvements of a wavemeter to measure the wavelength of an external cavity diode laser", Jour. Phys. Conf. Ser., vol. 605, no. 012018, pp. 1-5, April 2015.

[14] H. Hussein, M.A. Sobee, and M. Amer, "Calibration of a Michelson-type laser wavemeter and evaluation of its accuracy" Opt. and Las. in Eng., vol. 48 no. 3, pp. 393-397, Mar 2010.

[15] R. Castell, W. Demtröder, A. Fischer, R. Kullmer, H. Weickenmeier, and K. Wickert, "The accuracy of laser wavelength meters" Appl. Phys. B, vol. 38 no. 1, pp. 1-10, 1985.

[16] J. Vigue, B. Girard, "A systematic error of Michelson's type lambdameters", Rev. Phys. Appl., vol. 21, no. 8, pp. 463-465, Aug 1986.

Javier Diz Bugarín was born in Vigo, Spain, in 1968. He received the M.S. degree in telecommunications engineering from the University of Vigo, Spain, in 1994 and currently is working in his Ph.D. about interferometric techniques for gauge block calibration with laser diodes.
From 1994 to 1997, he was a Fellow with the Applied Physics Department at University of Vigo. Since 1998 he has been Electronics Professor with IES Escolas Proval at Nigran, Spain. He has worked as R & D engineer in electronics. Author of publications on renewable energies, microcontrollers and science education.

Ismael Outumuro González was born in Ourense, Spain, in 1982. He graduated in 2006 in physics at University of Vigo (Spain). Soon afterwards, he joined Metrology Laboratory of Galicia (Spain), where is currently working in dimensional metrology, in particular laser interferometry and coordinate measurement machines. He is enrolled in a PhD program about laser applications in metrology.

J. Benito Vázquez Dorrío was born in Ourense, Spain, in 1967. He received his BSc. degree in Physics in 1990 from the University of Santiago de Compostela (Spain), and Ph. D. degree in Physics in 1996 from the University of Vigo (Spain). Since 1998 he has permanent research position as Assistant Professor at the University of Vigo. He has co-authored over 50 international scientific publications. His research interests include fringe analysis, interferometry and phase-evaluation methods.

José Luis Valencia Álvarez was born in Barcelona, Spain, in 1977. He is a researcher at Metrology Laboratory of Galicia (Spain). He earned his M.Sc. (2000) and PhD (2005) in physics at University of Vigo (Spain). He has worked in National Physical Laboratory (UK) as a guest researcher from 2008 to 2010 in the area of dimensional nanometrology. His current areas of interest are atomic force microscopy and laser interferometry.

Jesús Blanco García was born in Vilanova de Arousa, Spain, in 1962. He received his Ph. D. in Physics in 1992 with a thesis on holographic interferometry, from the University of Santiago de Compostela (Spain). He currently teaches Physics at the University of Vigo. His main research subjects are holographic interferometry, moiré methods, ESPI, interferometers fringe analysis and Physics education.

5. CONCLUSIONES

En esta tesis se ha abordado el estudio y la realización de elementos necesarios para la calibración de Bloques Patrón Longitudinales. La construcción de un futuro sistema completo de medida de BPL requerirá la continuación de los trabajos y la integración de otros elementos como el sistema de estabilización de diodos láser. Como elementos más destacables del trabajo realizado, se citan los siguientes:

- Se ha estudiado el diseño general del sistema de medida, tema tratado en el Capítulo 2.

- Se ha realizado la integración en un único sistema de control de todos los elementos necesarios para automatizar el sistema de medida, incluyendo el desplazamiento de fase del interferómetro de medida, la lectura del conjunto de sensores que garantizan la estabilización de los parámetros ambientales para el control del índice de refracción y el cálculo preciso de la longitud de onda y los procesos de adquisición de imágenes y aplicación de algoritmos de cálculo de fase.

- Se ha avanzado en el estudio y caracterización de diversos tipos de algoritmos de evaluación de fase y de diferencia de fase y sus posibles fuentes de error, tema tratado en el Capítulo 3.

- Se ha diseñado y montado un prototipo de medidor de longitud de onda basado en el método Vernier, tema objeto del Capítulo 4.

- Se ha propuesto una nueva técnica de medida de longitud de onda basada en el método de las marcas de tiempo y realizado la parte electrónica de un nuevo medidor capaz de implementarla.

Los resultados obtenidos han sido suficientemente relevantes para su publicación en artículos de revistas internacionales de alto impacto (Anexo II) y en diferentes congresos nacionales e internacionales, cuya relación se incluye en el Anexo I.

Como líneas futuras de trabajo se proponen la continuación de los prototipos de medida de longitud de onda utilizando la nueva técnica desarrollada y la finalización del sistema completo de medida de Bloques Patrón Longitudinales, sin perjuicio de otras posibles aplicaciones de metrología, espectroscopia con diodos láser u otras.

6. BIBLIOGRAFÍA

[1] T. Doiron, J. Beers, "The Gauge Block Handbook, monograph 180", NIST, 1995. https://www.nist.gov/system/files/documents/calibrations/mono180.pdf. Acceso: 1/10/2022.

[2] Mitutoyo, "The History of Gauge Blocks", 2013, https://www.mitutoyo.com/webfoo/wp-content/uploads/E12016-History-of-The-Gage-Block.pdf. Acceso: 1/10/2022.

[3] D.A. Swyt, "Length and dimensional measurements at NIST", Journal of Research of the National Institute of Standards and Technology, 106 (2001) 1-23.

[4] Norma UNE-EN ISO 3650:2000, https://www.en-standard.eu/une-en-iso-3650-2000-geometrical-product-specification-gps-length-standards-gauge-blocks-iso-3650-1998/. Acceso: 1/10/2022.

[5] E.G. Michaelis, "A modification of Benoît's method of exact fractions", Proc. Phys. Soc. 61 (1948) 194.

[6] M. Born and E. Wolf, Principles of Optics, Pergamon Press, New York, 286-306, 1980.

[7] J.E. Decker and J.R. Pekelsky, "Gauge block calibracion by optical interferometry at the National Research Council of Canada", Measurement Science Conference, Pasadena, California, 23-24 January 1997.

[8] A. Titov, I. Malinovsky and C.A. Massome, "Gauge block measurements with nanometre uncertainty", Metrologia, 37 (2000) 121-130.

[9] M. O'Hora, B. Bowe and V. Toal, "Phase-stepped gauge block interferometry using a frequency tunable laser diode", Applied Optics, 45 (22) (2000) 5607-5613.

[10] M. Dobosz and O. Iwasinska-Kowalska "A new method of non-contact gauge block calibration using a fringe-counting technique", Optics and Laser Technology, 42 (1) (2010) 141–148.

[11] K.P. Birch and M.J. Downs, "An updated Edlen equation for the refractive index of air", Metrologia, 30 (1993) 155-162.

[12] K.P. Birch, F. Reinboth, R.E. Ward and G. Wikening, "The effect of variations in the refractive index of industrial air upon the uncertainty of precision length measurement", Metrologia, 30 (1993), 7-14.

[13] P.E. Ciddor, "Refractive Index of air: new equations for the visible and near infrared" Applied Optics, 35 (1996) 1566-1572.

[14] B.V. Dorrío, "Revisión de los algoritmos de desplazamiento de fase en Metrología Óptica", Óptica Pura y Aplicada, 31 (1998) 3-32.

[15] B.V. Dorrío and J.L. Fernández, "Phase-evaluation methods in whole-field optical measurement techniques", Measurement Science and Techonology, 10 (1999) 33-55.

[16] V. Álvarez-Valado, H. González-Jorge H, B.V. Dorrío, M. Miranda, F. Rodríguez, J.L. Valencia, F.J. Yebra and J. Rodríguez, "Testing phase-shifting algorithms for uncertainty evaluation in interferometric gauge block calibration", Metrologia, 46 (2009) 637-645.

[17] M. Miranda and B.V. Dorrío, "Fourier analysis of two-stage phase-shifting algorithms", J. Opt. Soc. Am. A, 27 (2010) 276-285.

[18] M. Miranda, V. Álvarez-Valado, B.V. Dorrío and H. González-Jorge, "Error propagation in differential phase evaluation", Optics Express, 18 (2010) 3119-3209.

[19] M. Miranda and B.V. Dorrío, "Monte Carlo based techniques of two-stage phase shifting algorithms", Optics and Lasers in Engineering, 49 (2011) 439-444.

[20] M. Miranda, B.V. Dorrío, J. Blanco, J. Diz-Bugarín and F. Ribas, "Characteristic Polynomial Theory of Two-Stage Phase Shifting Algorithms", Optics and Lasers in Engineering, 50 (2012), 522-528.

[21] Téllez-Quiñones A., Malacara-Doblado D., García-Márquez J., "Phase-shifting algorithms for a finite number of harmonics: First-order analysis by solving linear systems", Journal of the Optical Society of America A: Optics and Image Science, and Vision, 29 (4) (2012), 431-441.

[22] Téllez-Quiñones A., Malacara-Doblado D., García-Márquez J., "Compensation of the two-stage phase-shifting algorithms in the presence of detuning and harmonics", Journal of the Optical Society of America A: Optics and Image Science, and Vision, 30 (8), (2013), 1670-1679.

[23] Ghiglia, D. C., Pritt, M. D., "Two-Dimensional Phase Unwrapping: Theory, Algorithms, and Software", (1998) Wiley.

[24] Songzhe Lian, Haiquan Yang, and Hiroyuki Kudo, "Simple phase unwrapping method with continuous convex minimization," Opt. Express 30 (2022), 33395-33411.

[25] Liping Yan, Qiuxia Wang, Liu Huang, Benyong Chen, Ye Lin, "Phase unwrapping of digital holographic microscopy using adaptive region segmentation and phase derivative calibration with respect to fringe density", Optics and Lasers in Engineering, 148 (2022), 106780.

[26] Anik Ghosh, Rishikesh Kulkarni & Rajshekhar Gannavarpu, "Phase unwrapping algorithm using breadth-first-search and multi-level segmentation of phase quality interval in digital holography", Journal of Modern Optics 69 (2022), 957-967.

[27] K.B. McAdam, A. Steibach and C. Wieman, "A narrow-band tunable laser diode system with gratting feedback, and saturated absortion spectrometer for Cs and Rb", American Journal of Physics, 60 (12) (1992), 1098-1111.

[28] C. Wieman and G. Flowers, "Inexpensive laser cooling and trapping experiment for

undergraduate laboratories", American Journal of Physics, 63(4) (1995), 317-330.

[29] L.D. Turner, K.P. Weber, C.J. Hawthorn, R.E. Scholten "Frequency noise characterisation of narrow linewidth diode lasers," Optics Communications 201(4–6) (2002), 391-397.

[30] R. W. P. Drever, J. L. Hall, F. V. Kowalski, J. Hough, G. M. Ford, A. J. Munley & H. Ward, "Laser phase and frequency stabilization using an optical resonator" Appl. Phys. B: Lasers Opt. 31(2) (1983), 97–105.

[31] Sebastian D. Saliba, Mark Junker, Lincoln D. Turner, and Robert E. Scholten, "Mode stability of external cavity diode lasers", Appl. Opt. 48 (35) (2009), 6692–6700.

[32] S.D. Saliba and R.E. Scholten, "Linewidths below 100 kHz with external cavity diode lasers", Applied Optics, 48 (2009), 6961-6966.

[33] Wavemeter Moglabs, https://www.moglabs.com/products/wavemeters-and-pds/mwm. Acceso: 1/10/2022.

[34] J. L. Hall and S. A. Lee, ''Interferometric real-time display of cw dye laser wavelength with sub-Doppler accuracy,'' Appl. Phys. Lett. 29 (1976), 367–369.

[35] F. V. Kowalski, R. T. Hawkins, and A. L. Schawlow, "Digital wavemeter for cw lasers", J. Opt. Soc. Am. 66 (1976), 965–966.

[36] P. J. Fox, R. E. Scholten, M. R. Walkiewicz and R. E. Drullinger, "A reliable, compact, and low-cost Michelson wavemeter for laser wavelength measurement", Am. J. Phys., 67 (7) (1999), 624-630.

[37] A. Kahane, M. S. O'Sullivan, N. M. Sanford, B. P. Stoicheff, Vernier fringecounting device for laser wavelength measurements, Rev. Sci. Instrum. 54 (1983), 1138.

[38] Miao Miao, Zhou Wei, and Wang Bin, Application of length vernier in phase coincidence detection and precision frequency measurement, Rev. Sci. Instrum. 83 (2012), 024706.

[39] J. Pedregosa, D Guyomarc´h, M. Vedel, C. Champenois, M. Knoop, "Computer-controlled high-precision Michelson wavemeter", Eur. Phys. J. Plus, 129 (9) (2014).

[40] J. Ishikawa, N. Ito, and K. Tanaka, "Accurate wavelength meter for cw lasers", Appl. Opt., 25 (5) (1986), 639-643.

[41] S. J. Bennet, and P. G. Gill, "A digital interferometer for wavelength measurement", Journal of Physics E: Scientific Instruments, 13 (2) (1980), 174-177.

[42] M. Ugray, J. E. Atfield, T. G. McCarthy, and R. C. Shiell, "Microcontroller-based wavemeter using compression locking of an internal mirror reference laser", Rev. of Sci. Inst., 77 (2006), 113109.

[43] M Braun, J Maier and H Liening, "A high precision compact Michelson-Sagnac wavemeter",

J. Phys. E: Sci. Instrum., vol 20 (10) (1987), 1247.

[44] J.-P. Monchalin, M. J. Kelly, J. E. Thomas, N. A. Kurnit, A. Szöke, F. Zernike, P. H. Lee, and A. Javan, “Accurate laser wavelength measurement with a precision two-beam scanning Michelson interferometer”, Appl. Opt., 20, (5) (1981), 736-757.

ANEXO I. LISTA DE PUBLICACIONES RESULTANTES DE LOS TRABAJOS DE INVESTIGACIÓN

I.1. PUBLICACIONES EN REVISTAS INTERNACIONALES

Javier Diz-Bugarin, Benito V. Dorrio, Jesus Blanco, Marta Miranda, Ismael Outumuro, Jose Luis Valencia, "Design of an interferometric system for gauge block calibration", Optical Engineering 52(4), 045601 (3 April 2013). https://doi.org/10.1117/1.OE.52.4.045601

M. Miranda, B.V. Dorrio, J. Blanco, **J. Diz-Bugarin**, "Linear error analysis of differential phase shifting algorithms", Optik - International Journal for Light and Electron Optics, Vol. 124, Issue 8, 2013, pp. 710-717, ISSN 0030-4026. https://doi.org/10.1016/j.ijleo.2012.02.006

M. Miranda, B.V. Dorrio, J. Blanco, **J. Diz-Bugarin**, F. Ribas, "Characteristic polynomial theory of two-stage phase shifting algorithms", Optics and Lasers in Engineering, Vol. 50, Issue 4, April 2012, Pages 522-528, ISSN 0143-8166. https://doi.org/10.1016/j.optlaseng.2011.09.002

J. Diz-Bugarín, I. Outumuro-González, J. B. Vázquez-Dorrío, J. L. Valencia-Álvarez, J. Blanco-García, "Design of a New Microcontroller-Based Vernier Fringe Counter for Interferometric Measurement of Laser Wavelength", IEEE Transactions on Instrumentation and Measurement, Vol. 65, No. 2, pp. 407-412, Feb. 2016. https://doi.org/10.1109/TIM.2015.2482258

I.2. CONGRESOS INTERNACIONALES

M. Miranda, B.V. Dorrío, J. Blanco, **J. Bugarín**, F. Ribas, "Two-dimensional characteristic polynomials in the direct calculation of optical phase sum and difference", 7th Ibero-American Conference on Optics and 10th Latin-American Meeting on Optics, Lasers and Applications (RIAO-OPTILAS 2010), Pontificia Universidad Católica del Perú, Lima (Perú), 20-24 September, 2010, Journal of Physics, Conference Series Vol. 274, No. 012031, pp. 1-8, Feb. 2011, http://dx.doi.org/10.1088/1742-6596/274/1/012031

M. Miranda, B.V. Dorrío, J. Blanco, **J. Bugarín**, F. Ribas, "The Monte Carlo method as a tool for statistical characterisation of differential and aditive phase shifting algorithms", 7th Ibero-American Conference on Optics and 10th Latin-American Meeting on Optics, Lasers and Applications (RIAO-OPTILAS 2010), Pontificia Universidad Católica del Perú, Lima (Perú), 20-24 September, 2010, Journal of Physics, Conference Series Volume 274, no. 012032, pp. 1-9, Feb. 2011, http://dx.doi.org/10.1088/1742-6596/274/1/012032

M. Miranda, B.V. Dorrío, J. Blanco, **J. Diz-Bugarín**, F. Ribas, "Characteristic Polynomial Theory of Two-Stage Phase Shifting Algorithms", International Conference on Optics in Precision Engineering and Nanotechnology (ICOPEN 2011), Singapur, 23-25 marzo 2011, Proc:Physics Procedia Vol 19, ISBN: 978-1-62748-731-3

B. V. Dorrío, **J. Diz-Bugarin**, J. Blanco, F. Rivas, M. Miranda, F. Yebra, M. Otero, J. L. Valencia, J. Rodriguez, "Refractometric evaluation stability in interferometric gauge block calibration", International Conference on Applications of Optics and Photonics (AOP 2011), Braga (Portugal), May

3 -7 2011, Braga, Portugal. http://www.spidof.pt/aop2011/Abstracts_AOP2011.pdf

Diz, J., García González, J. Domínguez, J. "Modular architecture with microcontroller for advanced electronic practices". X Congreso de Tecnologías Aplicadas a la Enseñanza de la Electrónica (TAEE 2012), Vigo (España), 13-15 julio 2012, http://dx.doi.org/10.1109/TAEE.2012.6235415

J. Diz-Bugarin, B.V. Dorrío, J. Blanco, F. J. Yebra, I. Outomuro, M. Otero, J. Rodríguez, M. Miranda, J. L. Valencia, "Study of the refractometric stability of an interferometer equipment for gauge block calibration", SPIE Conference: Optical Engineering and Applications, San Diego, California, 14-16 aug 2012, Proc. SPIE 8493, no. 44, pp. 8493161-8, 2012. http://dx.doi.org/10.1117/12.929266

Outumuro, I., Valencia, J.L., Diz-Bugarin, J., Blanco, J., Dorrío, B.V., "Study of the stability and uncertainty of an external cavity diode laser through a Michelson wavemeter", SPIE Optical Engineering and Applications, San Diego, California, Aug 17-21 2014. Proc. SPIE, vol 9204, art. no. 92040M, pp. 92040M1-6, 2014. http://dx.doi.org/10.1117/12.2061761

Marta Miranda, **Javier Diz-Bugarín**, Benito V. Dorrío, Jesús Blanco, "Design of new phase shifting algorithms according to interferometer sensitivities", 8th Iberoamerican Optics Meeting and 11th Latin American Meeting on Optics, Lasers and Applications (RIAO/OPTILAS), 24-26 july 2013, Porto, Portugal, Proc. SPIE Vol 8785, no. 321, pp. 87856A1-6, 2013, http://dx.doi.org/10.1117/12.2026240

I. Outumuro, J. L. Valencia, J. Diz-Bugarin, I. Estevez-Caride, J. Blanco, B.V. Dorrío, "Stabilization and calibration of an ECDL system with a Michelson interferometer", 8th Iberoamerican Optics Meeting and 11th Latin American Meeting on Optics, Lasers and Applications (RIAO/OPTILAS), 24-26 july 2013, Porto, Portugal, Proc. SPIE Vol 8785, no. 360, pp. 87855E1-6, 2013. http://dx.doi.org/10.1117/12.2026295

Outumuro, I., Valencia, J.L., Diz-Bugarin, J., Blanco, J., Dorrio, B.V., "Wavemeter uncertainty evaluation for the calibration of external cavity diode lasers", 2nd International Conference on Applications of Optics and Photonics (AOP2014), Aveiro (Portugal), May 26-30, 2014. Proc. SPIE, vol 9286, art. no. 92860R, pp. 92860R 1-6, 2014. http://dx.doi.org/10.1117/12.2060658

I. Outumuro, J.L. Valencia, **J. Diz-Bugarin**, Jesus Blanco, B.V. Dorrío, "Uncertainty evaluation and electronic improvements of a wavemeter to measure the wavelength of an external cavity diode laser", 23rd International Commission for Optics Conference (ICO23), Santiago de Compostela, 26-29 August 2014. Journal of Physics Conference Series, Vol. 605, No. 012018, pp. 1-5, April 2015, http://dx.doi.org/10.1088/1742-6596/605/1/012018

Marta Miranda, **Javier Diz-Bugarín**, Benito V. Dorrío and Jesús Blanco, "Carré PSA for interferometric calibration", 23rd International Commission for Optics Conference (ICO23), Santiago de Compostela, 26-29 August 2014. ISBN: 978-84-697-1027-2.

J. Diz-Bugarin, A. Infante-Taboada, J. Benito Vazquez-Dorrio, J. Blanco-Garcia, I. Outumuro-Gonzalez, J. L. Valencia-Alvarez, "Interferometric comparison of laser wavelengths: learning applications of an innovation project in vocational training", XII Congreso de Tecnologías, Aprendizaje y Enseñanza de la Electrónica (TAEE 2016), Sevilla, España, 22-24 Julio 2016. http://dx.doi.org/10.1109/TAEE.2016.7528242

I. Outumuro, **J. Diz-Bugarin**, J. L. Valencia, J. Blanco, B. V. Dorrío, "Wavemeter improvements for laser diode calibration", Third International Conference on Applications of Optics and Photonics (AOP 2017), Faro, Portugal, 8-12 May 2017. Proc. SPIE 0277-786X, Vol 10453, http://dx.doi.org/10.1117/12.2272010

Benito Vázquez-Dorrío, Samuel Costa, **Javier Diz-Bugarin**, Jesus Blanco-Garcia, "Absolute flatness measurement with a Twyman-Green interferometer", Third International Conference on Applications of Optics and Photonics (AOP 2017), Faro, Portugal, 8-12 May 2017.

I.3. CONGRESOS NACIONALES

J. Diz-Bugarín, B.V. Dorrío, J. Blanco, M. Miranda, F. Ribas, F. J. Yebra, M. Otero, J. Rodríguez, I. Outumuro, J. L. Valencia, "Gauge block interferometric calibration at the university of Vigo/LOMG", VIII Jornadas de Procesado de Materiales con Tecnología Láser, 16-17 noviembre de 2011. AIMEN, Porriño, España, 2011.

J. Diz-Bugarín, B.V. Dorrío, J. Blanco, M. Miranda, F. J. Yebra, M. Otero, J. Rodríguez, I. Outomuro, J. L. Valencia, "Estabilidad refractométrica y piezoeléctrica en la medida de bloques patrón longitudinales con interferometría de desplazamiento de fase", X Reunión Nacional Óptica, Zaragoza, 4-7 sep 2012, pp. 401-404. ISBN: 978-84-695-4749-6.

J. L. Valencia, I. Outumuro, J. A. Mondaray, **J. Diz-Bugarín**, J. Blanco, B. V. Dorrío, "Láser de diodo rojo estabilizado mediante una técnica de anclaje en frecuencia para Metrología Dimensional", X Reunión Nacional Óptica, Zaragoza, 4-7 sep 2012, pp. 421-424. ISBN: 978-84-695-4749-6.

I. Outumuro, J. L. Valencia, **J. Diz-Bugarín**, J. Blanco, B. V. Dorrío, "Estabilización de un diodo láser de cavidad externa para la calibración de bloques patrón", V Congreso Español de Metrología, Madrid 12-13 junio 2013.

Javier Diz, Ismael Outumuro, Benito V. Dorrío, José L. Valencia, Jesús Blanco, "Métodos electrónicos de mejora de la precisión subfranja para la medición de longitud de onda de diodos láser con interferómetro Michelson", IX Reunión Española de Optoelectrónica, Salamanca, 13-15 de Julio de 2015. Libro Actas pp. 224-229 ISBN: 978-84-606-9716-9

Javier Diz-Bugarín, Ismael Outumuro, Benito V. Dorrio, Jesús Blanco, José L. Valencia, "Deseño dun medidor electrónico de lonxitude de onda de díodos láser con interferómetro Michelson", I Workshop do Programa Interuniversitario de Doutoramento en Láser, Fotónica e Visión 2015, Santiago de Compostela (España), 25 de setembro de 2015.

Javier Diz-Bugarín, Ismael Outumuro, Benito V. Dorrio, Jesús Blanco, José L. Valencia, "Transferencia de tecnología en un proyecto de innovación: aplicaciones docentes de un medidor de longitud de onda de láser", II Workshop do Programa Interuniversitario de Doutoramento en Láser, Fotónica e Visión 2016, Santiago de Compostela (España), 7 de outubro de 2016.

ANEXO II. FACTOR DE IMPACTO Y CRITERIOS DE CALIDAD DE PUBLICACIONES

ARTÍCULO: "Design of an interferometric system for gauge block calibration"

Journal: Optical Engineering	
Título Abreviado ISO	Opt. Eng.
Editor	SPIE-SOC PHOTO-OPTICAL INSTRUMENTATION ENGINEERS
País	USA
Año	2013
ISSN	0091-3286
Código Publicación	XT001
1er Año Publicación	1956
Código Categoría	SY
Descripción Categoría	OPTICS
Cuartil	Q3
Factor impacto	0,958
Factor impacto 5 años	0,847

Total citas	Influencia Art.	Índice Inmediatez
6918	0,215	0,245
Vida Media Citas	Eigenfactor	Ranking Categoría
9,6	0,00885	55/83

ARTÍCULO: “Linear error analysis of differential phase shifting algorithms”

Journal: Optik - International Journal for Light and Electron Optics	
Título Abreviado ISO	Optik
Editor	ELSEVIER GMBH, URBAN & FISCHER VERLAG
País	Germany
Año	2013
ISSN	0030-4026
Código Publicación	ZX450
1er Año Publicación	1949
Código Categoría	SY
Descripción Categoría	OPTICS
Cuartil	Q3
Factor impacto	0,769
Factor impacto 5 años	0,730

Total citas	Influencia Art.	Índice Inmediatez
2239	0,113	0,069
Vida Media Citas	Eigenfactor	Ranking Categoría
4	0,00318	62/83

ARTÍCULO: "Characteristic polynomial theory of two-stage phase shifting algorithms"

Journal: Optics and Lasers in Engineering	
Título Abreviado ISO	Opt. Lasers Eng.
Editor	ELSEVIER SCI LTD
País	England
Año	2012
ISSN	0143-8166
Código Publicación	JM451
1er Año Publicación	1980
Código Categoría	SY
Descripción Categoría	OPTICS
Cuartil	Q2
Factor impacto	1,916
Factor impacto 5 años	1,837

Total citas	Influencia Art.	Índice Inmediatez
2773	0,5	0,386
Vida Media Citas	Eigenfactor	Ranking Categoría
4,5	0,00743	25/80

ARTÍCULO: "Design of a New Microcontroller-Based Vernier Fringe Counter for Interferometric Measurement of Laser Wavelength"

Journal: IEEE Transactions on Instrumentation and Measurement	
Título Abreviado ISO	IEEE Trans. Instrum. Meas.
Editor	IEEE-INST ELECTRICAL ELECTRONICS ENGINEERS INC
País	USA
Año	2016
ISSN	0018-9456
Código Publicación	LT560
1er Año Publicación	1952
Código Categoría	OA
Descripción Categoría	INSTRUMENTS & INSTRUMENTATION
Cuartil	Q1
Factor impacto	2,456
Factor impacto 5 años	2,426

Total citas	Influencia Art.	Índice Inmediatez
10902	0,549	0,386
Vida Media Citas	Eigenfactor	Ranking Categoría
7	0,01477	14/58

Universidade Vigo